

**Synthesis of carbon nanomaterials by
using in-liquid plasma and its application
to fuel cell**

AMANO Tomoki

2018

Nagoya University

Department of Electrical Engineering and Computer Science

Contents

Chapter 1 Introduction

1.1 Carbon nanomaterials	1
1.2 Nanographene	4
1.2.1 Characteristics.....	4
1.2.2 Synthesis methods	5
1.2.3 Synthesis of nanographene using by in-liquid plasma	6
1.3 Polymer electrolyte fuel cell (PEFC).....	9
1.3.1 Fundamentals.....	9
1.3.2 Issues of polymer electrolyte fuel cell	13
1.3.3 Background of catalysts in the polymer electrolyte fuel cell	16
1.4 Objective and composition of this thesis	18
References	21

Chapter 2 Experimental setup and evaluation methods of nanographene

2.1 Synthesis of nanographene	26
2.1.1 In-liquid plasma method	26
2.1.2 Hydrogen peroxide treatment	29
2.1.3 Platinum nanoparticle loading method	30
2.2 Plasma diagnostic technique	31
2.2.1 Optical Emission spectroscopy (OES)	31
2.3 Evaluation methods of nanographene	32
2.3.1 Raman spectroscopy	32
2.3.2 X-ray diffraction (XRD)	35
2.3.3 Scanning electron microscopy (SEM)	39
2.3.4 Transfer electron microscopy (TEM)	42
2.3.5 X-ray photoelectron spectroscopy (XPS)	46

Contents

2.3.6 Electrochemical measurement	48
References	57

Chapter 3 Synthesis of nanographene and durability as catalyst electrode for fuel cell

3.1 Introduction	59
3.2 Experimental details	61
3.3 Synthesized and Characteristics	65
3.3.1 Plasma diagnostics	65
3.3.2 Synthesis rates	70
3.3.3 Degree of perfection of six-membered ring structure	72
3.4 Crystalline structures of Pt nanoparticles supported on nanographenes	76
3.5 Durability of catalyst of the Pt nanoparticles supported nanographenes	84
3.6 Summary	90
References	92

Chapter 4 Synthesis of carbon flakes by in-liquid plasma using iron phthalocyanine added alcohols

4.1 Introduction	93
4.2 Experimental details	95
4.3 Nanographene synthesized by in-liquid plasma	97
4.3.1 Surface condition of graphene flakes	97
4.3.2 Plasma diagnostics	100
4.4 Effect of iron-phthalocyanine on flaky structure	101
4.5 Conclusion	106
References	107

Chapter 5 Structures and catalytic activity of carbon nanomaterial synthesized using iron phthalocyanine

5.1 Introduction	109
5.2 Experimental details	111
5.3 Synthesis characteristics by in-liquid plasma with FePc	113
5.4 Structural and morphologic properties	115
5.5 Catalytic activity of iron-nitrogen doped carbon nanomaterial	120
5.5.1 Composition and chemical bonding states	120
5.5.2 Catalytic activity	123
5.6 Conclusion	129
References	130

Chapter 6 Conclusions and future works

6.1 Summary of this thesis	131
6.2 Scopes for future works	134

Acknowledgements	136
List of papers	138

Chapter 1

Introduction

1.1 Carbon nanomaterials

Carbon nanomaterials have attracted particular attention in the world of nanotechnology in recent years, because of a number of researches on carbon nanomaterials. Structures of carbons are diverse caused to form various bonds such as sp , sp^2 , and sp^3 bonding, involved in carbon nanotubes and graphene sheets. These carbon nanomaterials are composed of carbon atoms, therefore weights of the nano carbon materials are lighter than the other materials of traditional metals, and so on.

Fullerene is a carbon nanomaterial having a structure of soccer balls composed of 60 carbon atoms, consisting of 60 carbon atoms involving 12 five-membered rings and 20 six-membered rings. In 1985, the fullerene was discovered by Kroto et al.[1] Before the discovery, Osawa predicted the existence of fullerene [2]. Fullerenes are known to have various applications such as lubricant .[3-7]

Carbon nanotubes are formed into a coaxial tubular shape in multiple layers, which are constituted six-membered rings of carbon, as discovered by Iijima et al. in 1991 [8]. The multilayer carbon nanotubes were discovered from the deposits of the arc electrodes in the fullerene synthesis, employing the arc discharge method. In 1993, they

also discovered the single-walled carbon nanotubes [9]. An annular number of the six-membered ring in the single-walled carbon nanotubes changes in electrical and optical properties. From the different annular structure of the single-walled carbon nanotubes, metallic and semiconducting characters appeared in electrical properties [10]. Chemical stability of the carbon nanotubes shows high resistance. The other properties are also superior 100 times high tensile strength of steel [11], 1000 times tolerance current density of copper [12], and 10 times large thermal conductivity [13]. Nowadays, carbon nanotubes are used for applications to battery, sensor, and wiring material [14-17].

Graphite consists of a stack of graphene. Graphite is known as a core of a pencil and its crystal structure is a laminate of carbon atoms forming some honeycomb lattice. Graphene honeycomb lattice forms a strong covalent sp^2 bond. By the hybridization of orbitals of the p orbit and s orbit of carbon atom, the sp^2 hybrid bonds form three angles 120° with each other in one plane. Graphene layers are stacked with a weak van der Waals binding.

The graphene layer was experimentally realized by the Geim group of Manchester University in Great Britain in 2004. A piece of Scotch tape adhered on graphite surface and the tape was peeled off. One layer of graphene could be obtained by this exfoliation method [18].

The unique physical properties of graphene have been understood theoretically. The theoretical electron mobility is expected 20 times higher than that of silicon [19-20]. It may be possible to operate at a very high speed with wiring materials. The excellent physical properties are confirmed experimentally. These excellences were also found in the other properties such as chemical physical properties, opportunity physical

Chapter 1

properties, and thermo-physical properties. It is expected to be useful for next generation device materials [21].

1.2 Nanographene

1.2.1 Characteristics

Graphene is a two-dimensional sheet constituted by a six-membered ring structure of carbon atoms. Figure 1-1 shows the classification of graphene materials by size difference [22]. Graphene has a sheet with a size of 100 nm or larger. Nanographene has sheets with a size of 100 nm or larger.

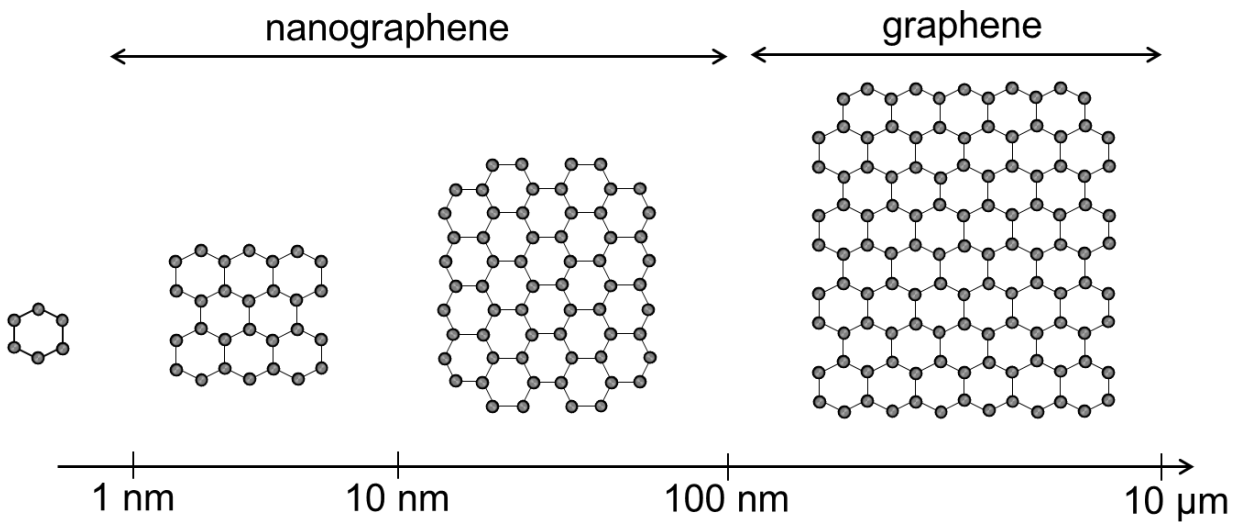


Fig. 1-1. Classification by graphene sheet size.

1.2.2 Synthesis methods

Graphene has been conventionally synthesized by a method such as an epitaxial growth method, a chemical vapor deposition (CVD) method, etc. [23]. The methods are necessary using a large-scale apparatus having a vacuum pump. These vacuum process costs and the apparatus are enormous expensive. It spends a lot of time to evacuate the process chamber and to synthesize a large quantity of graphene. Large quantities of graphene with a high quality are issued on a problem in the graphene synthesis methods.

In recent years, a method for chemically reducing graphite oxide (GO) to obtain graphene has also been established [24]. This method is possible to synthesize graphenes at a high speed and at a low cost. This method also requires without any large-sized apparatus having the vacuum pump. The synthesized graphene is a problem on the low crystallinity.

There are the other methods of preparing nanographene. A method provides graphene to cut into small pieces of large graphene sheets grown on a large substrate, using the lithography. Essentially, this method is limited to use only small production of nanographene. In addition, another method is used a source of carbon nanotube. The incision of carbon nanotubes are performed by chemical treatments. This is possible to synthesize in large quantities. There is a problem on the low crystallinity, damaged by the chemical treatments.

The organic chemistry synthesis as bottom-up method can be used to synthesize large quantities of nanographenes with the sheet-size of several nanometers. A disadvantage is a complex, multiple processes for the synthesis. The organic synthesis methods are progressing at present.

There is no best method in the synthesis process of graphene, because there is a trade-off relationship between synthesis amounts and material quality. The author has been developed a method called in-liquid plasma method, which was established for synthesizing cheap and high quality graphenes.

1.2.3 Background of in-liquid plasma

In-liquid plasma is a method in which bubbles are formed in a solution by using microwaves or high-frequency powers. Plasma is generated in the solution to come into contact with the liquid. This submerged plasma is advantageous that there is a difference of more than three orders of magnitude between the liquid and the gas, whereas individual and liquid have a difference of about one order of magnitude compared to individual and liquid densities. In other words, the density of the liquid is far higher than that of the gas, and the density of reactive active species generated by the plasma is very high.

According to film formation technology using in-liquid plasma, it has been reported that the amorphous carbon film (DLC) can be deposited at a speed of about 9000 times faster than vapor deposition method of conventional vapor [25]. Moreover, the in-liquid plasma has been used for synthesis of metal nanoparticles, plasma scalpel in medical field and the like in recent years [26-29]. New applications are opened in fields such as bioprocess, inactivation of algae, and material process.

Since the periphery of the plasma is covered with a liquid having a large heat capacity, a cooling effect is suitable for a film formation process of a substrate material susceptible to heat can be performed. In view of the advantages of in-liquid plasma as

described above, the synthesis of carbon nanomaterials has attracted much attention.

This in-liquid plasma method is operated in a normal temperature and pressure process, no equipment for vacuum and cooling is required. Thus, apparatus can be fabricated by the small size and low cost.

1.2.4 Nanographene synthesis in the in-liquid plasma

An alternative synthesis method has been reported by Hagino *et al* [30]. Nanographene synthesis became possible at a higher rate than the conventional gas phase process, compared to the reduction process of graphite oxide. This is characteristic and also high crystallization of nanographene speed realized in a liquid phase process. This method yielded high-crystallinity nanographene with a G-band peak FWHM of less than 30 cm^{-1} and a high synthesis rate of up to 0.61 mg/min .

In the in-liquid plasma method, two electrodes are positioned such that they sandwich the boundary between the gas and the liquid. That is, one electrode is placed in the liquid alcohol, while the other is placed in the Ar ambient. Situated between these two basic phases, the third, the additional phase at the gas-liquid boundary, which is in the form of a layer, is expected to induce a rich reaction field. For convenience, here the author refers to it as an in-liquid plasma, which is generated away the gas phase, the gas-liquid boundary layer phase, and the liquid phase. The in-liquid plasma can potentially provide the rich chemistry: Relatively high-energy electrons generate atomic species such as hydrogen, oxygen, and carbon in the gas phase, and a rich variety of radicals of the precursors derived from alcohols is generated in the liquid plasma. Furthermore, reactions occur between the atomic species and precursors, yielding

products in non-equilibrium states. Such a rich reaction field causes mutual reactions at the boundary layer between the gas and liquid phases.

This time, the plasma used by the author is of the type in which one electrode is in the gas phase and the other is in the liquid phase. The other liquid plasma is the one which causes the discharge in the liquid. Our plasma can utilize three reaction fields of gas phase, gas-liquid interface and liquid phase.

In actual syntheses, the synthesis rates strongly depended on the type of alcohol. The synthesis rate obtained using 1-butanol was roughly three times higher than that obtained using ethanol. A synthesis mechanism has been proposed based on analyses of residual liquids using the gas chromatography. Figure 1-2 shows the synthesis model from the GC-MS analysis.

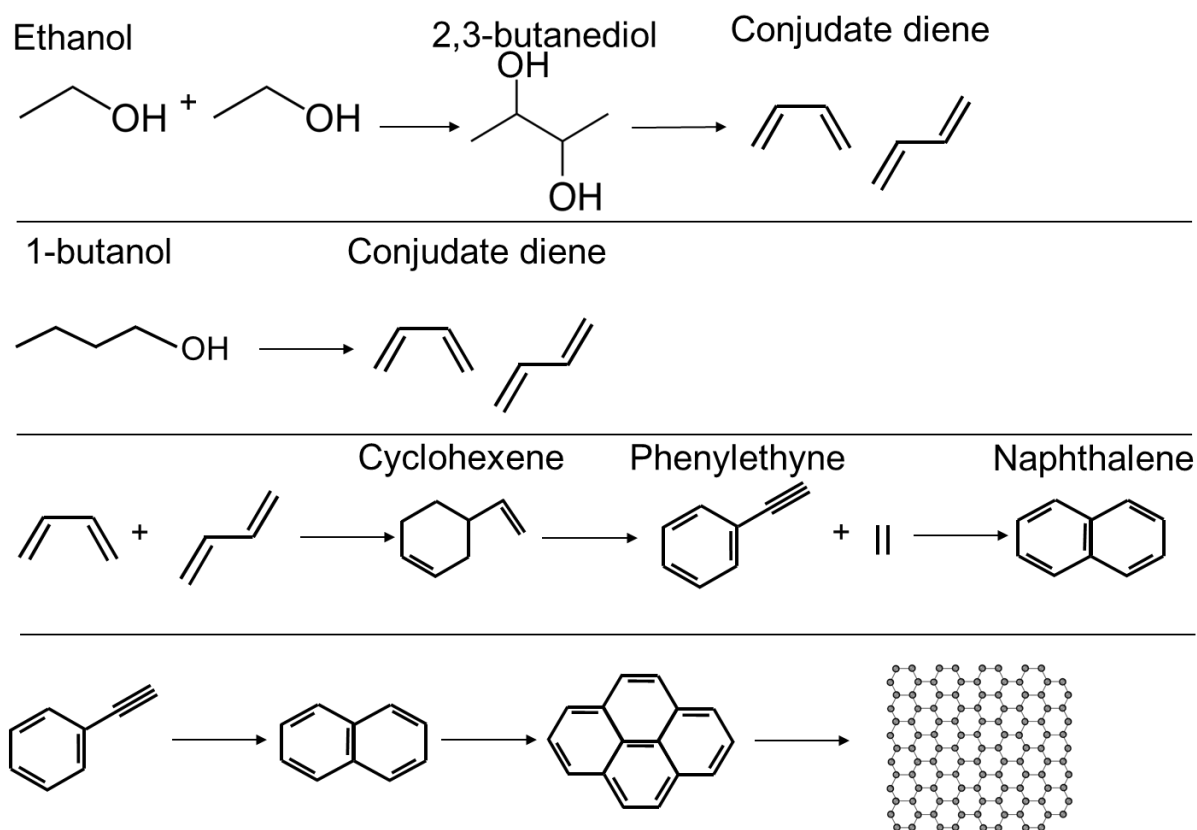


Fig. 1-2 Synthetic model from GC-MS analysis.

1.3 Polymer electrolyte fuel cell (PEFC)

1.3.1 Fundamentals

Global warming is issued on the carbon dioxide emissions in recent years. Among carbon dioxide emitted in Japan in recent years, the amount of carbon dioxide discharged from the transport sector of automobiles, ships, etc. accounts for about 20%. Especially automobiles are one of the major causes of environmental pollution [31].

It is necessary to decentralize the energy from the exhaustion of fossil fuels. Fuel cells, solar batteries, wind power generations, etc., have attracted attentions of the green energy in practical use. The fuel cells have been proposed for the application as a small and stable power supply. Since the fuel cell generates the electricity using hydrogen, it hardly emits the harmful gas. These green energy applications are proposed to be greatly solved by suppression of the global warming and the air pollution.

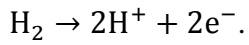
The operating temperature of the fuel cell depends on the temperature at which ions can move through the electrolyte. Therefore, an appropriate fuel and catalyst are selected by the electrolyte. First, polymer electrolyte fuel cells are suitable for environments where the operating temperature is low and start-up and shutdown are frequently performed [32]. Second, phosphoric acid fuel cell has almost the same structure as the solid polymer fuel cell, but because the phosphoric acid is used for the electrolyte membrane, the operating temperature is as high as 200°C [33]. Also, since the temperature is high, the effect of poisoning by carbon monoxide contained in the fuel is small. Third, the molten carbonate fuel cell has a high operating temperature of about 650°C, but has the merit of not using a noble metal as a catalyst [34]. Fourth, the solid oxide fuel cell has the highest fuel efficiency among fuel cells. The solid oxide

fuel cells have been started recently to use in domestic industry and consumer areas [35].

Especially among fuel cells, the polymer electrolyte fuel cell has an advantage that the operating temperature is as low as 80 to 100 °C, as compared with other fuel cells. Output density per unit volume is high, since the electrode is coated with a solution of the polymer membrane to form a catalyst, owing to increase the reaction area of the electrodes. Characteristics of low operating temperature and high power density of polymer electrolyte fuel cells enable to fuel cells such as home power generation, transport machinery and mobile equipment. Since the electrolyte is solid, vibration resistant and easy mass-production are also expected. In a view of economic costs, the low operating temperature is advantageous. The other types of fuel cells are necessary to use special materials [36-38]. Thus, in recent years, hydrogen as a substitute for gasoline is proposed to realize fuel cell vehicles using solid polymer type fuel cells by automobile manufacturers.

The basic principle of a polymer electrolyte fuel cell is an electrochemical device that supplies a fuel and an oxidizer from the outside and causes ion reactions to take out a direct current. In most cases, the reactions that generate electrical currents are oxidation reaction of H₂. The fuel of natural gas (methane) or methanol supplies from outside of cells instead of hydrogen gas. In that case, a device (reformer) for obtaining hydrogen from the fuel is needed, but this is a system suitable for stationary type from the viewpoint of running cost. For a vehicle-mounted type, the installation of a hydrogen fuel station is a problem. Whereas, the cell contains a reactive substance (closed system), the fuel cell supplies a reactant from the outside and discharges a purified substance (usually H₂O), so it is a flow system or an open system. The basic configuration is as shown in Figure 1-3. In the type, the reaction of hydrogen and

oxygen (air) is practically equated, at the anode



When the oxidation reaction occurs, electrons flow to the outside circuits. H^+ as a charge carrier diffuses through the polymer membrane as ion conductor. At the cathode, H^+ recombines with electrons and oxygen. The reaction is given by

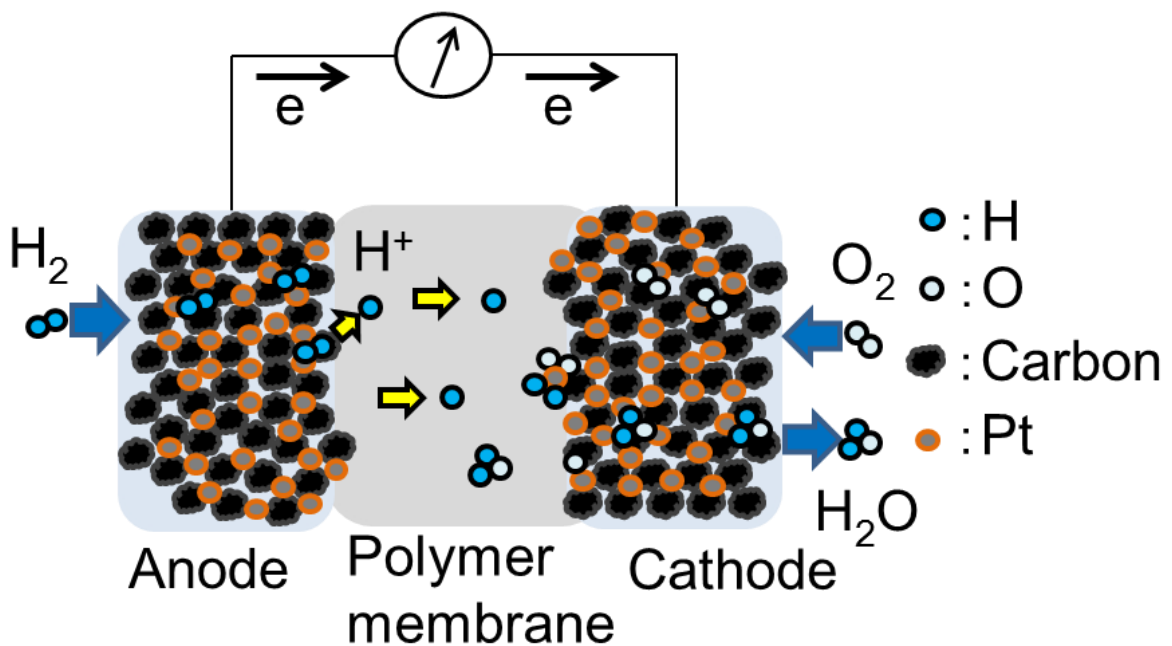
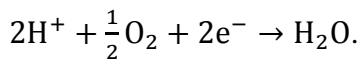


Fig. 1-3 Schematic diagram of polymer electrolyte fuel cell catalyst layer.

Catalysts decorated on the electrodes are composed of a support material and a catalytic metal. Currently, platinum is generally used as a catalyst, and carbon black is used as a support material. Instead of the carbon black, attempts have been made to use carbon nanotubes and carbon nanohorns from the size of its surface area in recent years [39-40]. Since the chemical reaction of oxygen and hydrogen is carried out in the electrode catalyst layer, the surface areas per unit are an important factor determining

the power generation efficiency. Therefore, it needs to increase the surface area of the carbon nanomaterial as the electrode carrier. The effective surface area of the platinum as the catalyst is very important for the practical application of the fuel cell.

A catalyst is capable of proceeding chemical reactions at low temperature. In a view of thermodynamics, lowering the activation energy accelerates selectively the specific reactions. Generally, the amount and quality of the catalyst do not change at all before and after the reaction. The catalysts are not included in the chemical equation. A catalyst compounds are added in the reaction system with a relatively small amount.

Since PEFC uses a solid polymer electrolyte membrane, it can be operated at low temperature (80-100 ° C), and it is expected to be put into practical use as a car power source, home cogeneration (combined heat and power), and portable power source. Lower temperature causes higher catalytic activation voltage (polarization) of the electrode and the lower voltage efficiency. Therefore, the high active noble metal is used for the catalyst. Platinum is the most suitable to corrosion resistance, to process ability, and the environmental impact.

1.3.2 Issues of polymer electrolyte fuel cell

Durability

Degradation of the catalyst layer is a serious problem as a problem of solid polymer fuel cells. Carbon black which can be mass synthesized at a low cost is used [41]. The corrosion occurs due to the low chemical stability and crystallinity. When the fuel cell starts and stops, applied high potential to the cathode deteriorates the catalysts [42]. Figure 1-4 shows a schematic diagram of platinum-supporting carbon before and after the cycle test. The catalyst particles supported the carbon black easily corroded and agglomerated during the cycle test [43-45]. In order to suppress this aggregation, carbon nanomaterials are expected to use as catalyst-supports for fuel cells because of high stability and high crystallinity.

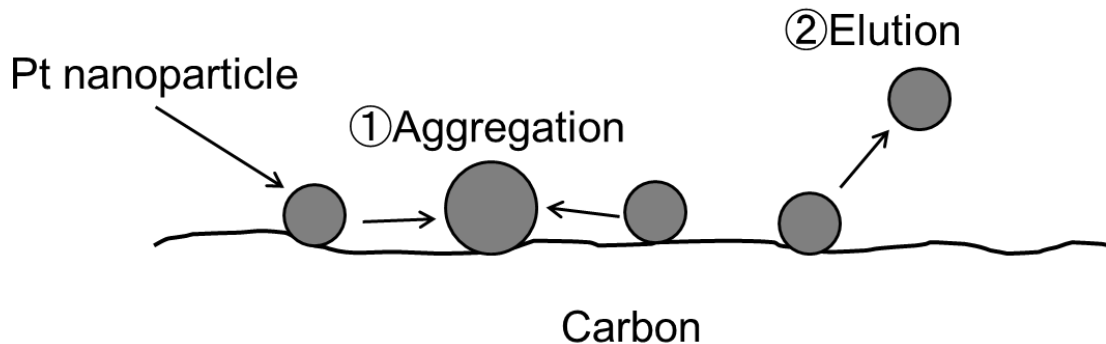


Fig. 1-4 Flow of catalyst layer deterioration.

Catalyst metal

One of the most important tasks is issued on the reduction of the economic cost of platinum. Since the platinum is very expensive, efficient uses of platinum are necessary. If catalyst performance improved, it would be reduce amounts of uses of Pt. To atomize platinum at nanoscale will solve this problem. Thus, a use of fine particles of platinum is possible to reduce an amount of total use of platinum, while an effective platinum surface area is kept to a constant. Nano-sized particles would achieve the high surface area (specific surface area) per unit weight and the high contact area. Fine particles of platinum improve the electrochemical characteristics, leading to reduce the catalyst costs.

The metal fine particle synthesis is in general known to be difficult due to the high surface energy of particles. In practical uses in the fuel cell, the platinum catalyst is supported on the carbon nanomaterial at nanoscale. The surface area of the carbon nanomaterial used is also required to increase. Figure 1-5 shows the relationship between platinum fine particles and the theoretical specific surface area. This figure of merits is calculated by the specific surface area of platinum fine particles, given by $M = (n4\pi \cdot r^3 / 3)\rho$, where n particles of radius r, the total surface area, and the density ρ . The density is constant. Larger particle radius r, leads to larger the specific surface area. The specific surface area increases as the nanosize of platinum fine particles progresses, the catalytic activity becomes the highest at 2-4 nm, and decreases at 1 nm or less [46]. When the particle size becomes less than several nanometers, the surface energy increased extremely. It should be considered that the fine particle easily agglomerates and grows large particles.

To solve the problem, the surface energy of metal particles should be reduced. Carbon nanomaterials promote the stabilization of the fine particles by exchanging electrons through the contact surface between the fine particles. The catalysts should be fine platinum particles at nanoscale with high surface area of the carbon nanomaterial and low electrical conductance, capable of supporting fine particles. Studies on the "catalytic platinum atomization" and "electronic carrier having a large specific surface area and good supporting performance of particles" have been actively conducted.

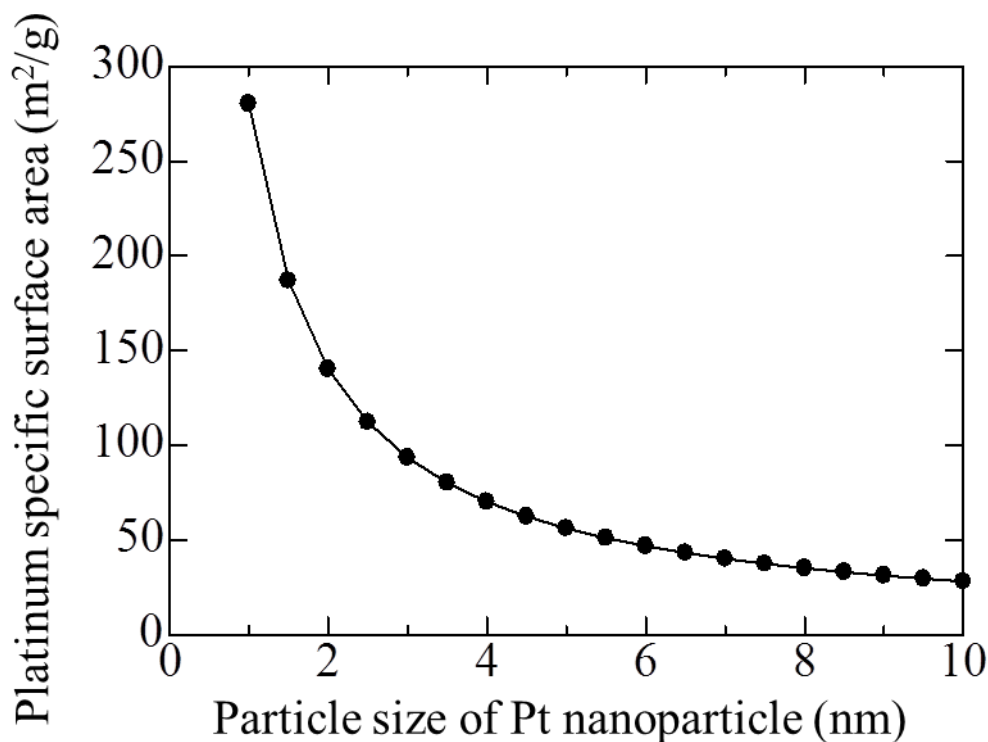


Fig. 1-5 Relation between platinum fine particles and theoretical specific surface area.

1.3.3 Previous researches on catalysts in the polymer electrolyte fuel cell

In the catalyst electrode of the fuel cell, the carbon black is used as a catalyst carrier. Since the carbon black has a low chemical stability, it is known that carbon black is deteriorated by a high electric potential applied at the on / off time of the fuel cell. As a method for improving this durability, it is necessary to improve the graphitization of carbon. It becomes thermally and electrochemically stable by the graphitization. In addition, the oxidative corrosion is preferentially promoted from the carbon defect site. In order to increase the degree of graphitization, it is achieved by heating the carbon material to a high temperature (1600 °C or higher), and the obtained carbon material has a high degree of graphitization [47]. As a result, the resistance against corrosion of carbon becomes high, and a material with fewer defects is obtained. Defects on the surface of the carbon material work as sites of the catalytic metal.

Carbon nanomaterials have been studied as a material which is changed to conventional carbon black [48-51]. For example, it is the carbon nanotube, the carbon nanofiber or the graphene. It is reported that the catalytic reaction is enhanced by using these. The durability is improved as compared with the carbon black. However, carbon nanotubes cause the irreversible aggregation by van der Waals forces. Moreover, it has a problem of high cost for synthesis. Graphene has been synthesized by various synthetic methods and there is a possibility of mass synthesis. The theoretical specific surface area is twice as large as that of carbon nanotubes. Therefore, it is expected that platinum fine particles are supported at a high density.

The research on non-platinum catalysts is under way to solve this problem [52-55].

In order to reduce the amount of Pt used, studies have been made to prepare alloy catalysts with the shape of nanoparticles and transition metals. Catalysts using inexpensive noble metals other than Pt have also been studied. Carbon containing N atom in the catalyst which does not use precious metal is being investigated. In the description of nitrogen-doped carbon supported metal ions metal oxides or transition metal chalcogenides are considered a potential alternative to conventional Pt-based cathode catalysts. These materials still have inadequate catalytic activity compared to Pt, but are potentially superior to Pt in terms of stability. Furthermore, research results have been obtained that show catalytic activity also in nitrogen doped carbon.

Transition metals have been mainly studied so far. Among them, metal oxides were also investigated to increase the durability of the catalyst. It was also found that catalytic activity was exhibited from a nitrogen-containing carbon material. In recent years, catalysts containing transition metals in addition to nitrogen and carbon materials have been mainly studied. It has a metal-nitrogen-carbon structure as its structure. As a preparation method, there has been widely used mainly adding nitrogen-containing metal complex to a carbon material. To this end, in 1964, the oxygen reduction properties of the transition-metal phthalocyanine were first reported [56]. Later, the use of transition-metal phthalocyanine like iron and cobalt phthalocyanine as catalysts was also proposed [57-60]. Nonetheless, iron phthalocyanine has not exceeded the catalytic activity of Pt catalysts in the case of oxygen reduction reactions owing to its poor electron conductivity [61]. In particular, the iron phthalocyanine is likely to degrade in acidic solutions that are used in fuel cells [62]. To address these problems, the use of carbon nanomaterials with the metal phthalocyanines is suggested [63-64].

1.4 Objectives and composition of this thesis

The synthesis method using in-liquid plasmas is more advantageous than the conventional carbon nanomaterial synthesis method. Therefore, it is absolutely necessary to study the application destination of the synthesized nanographene, and it is necessary to clarify the synthesis process and characterization.

Nanographene synthesized by in-liquid plasmas can be synthesized at high a speed and has a high crystallinity. If the nanographene can be applied to the fuel cell, it can be considered that the lifetime of the fuel cell can be increased. It is also thought that by using the nanographene it is possible to realize a platinum alternative catalyst.

The structures and properties of carbon nanomaterials are described in Section 1.1. Then, graphene consisting of two-dimension sheets have characteristic structural features and exhibit unique electronic properties. In Section 1.2, the definition of nanographene and conventional graphene synthesis method and problems are summarized. The author emphasizes the superiority of nanographene synthesis using submerged plasma. Section 1.3 described the current status and issues of fuel cells. The author describes the superiority of polymer electrolyte fuel cells and their problems. In Section 1.4, as a problem of the fuel cell, there are things such as deterioration of the catalyst carrier and exploration of the platinum substitution catalyst, but the preceding research which has been carried out.

In Chapter 2, the in-liquid plasma device for synthesizing nanographene was described. The amorphous carbon removal treatment of the synthesized graphene and the platinum supporting process are shown. Various evaluation methods of the nanographene are also described.

In Chapter 3, a nanographene synthesized in in-liquid plasmas has the highly durable catalyst-support-property in applications of polymer electrolyte fuel-cells (PEFC). The in-liquid plasma was generated using copper or graphite electrodes positioned outside and within ethanol, 1-propanol, or 1-butanol. The higher the electron density derived from the spectrum of H_{β} , the higher the synthesis amount. There was a trade-off relationship between the synthesis rate and the crystallinity of nanographenes depending on kinds of alcohols employed as a liquid. The nanographene synthesized using the ethanol was hardly degraded in a high-potential cycle test of the half-cell, e.g., only loss of 10% in effective surface area of Pt even after 10,000 cycles. The better catalyst-support property in the PEFC was obtained by the nanographene with the narrower width of the G-band peak in the Raman spectra, owing to the perfect formation of six-membered ring carbons, rather than that with wider domain sizes of the crystallites.

In Chapter 4, giant graphene-flakes with a size of micrometer scale were grown in the liquid phase of submerged plasmas of iron-phthalocyanine (FePc)-added ethanol. The atmospheric pressure plasmas were generated in the Ar gas phase and in the liquid phase comprising of bubbles and liquid-solution. The mixture of FePC in ethanol was essential for the formation of giant graphene-flakes of aggregates of nanographenes, confirming by D, G and 2D bands in the Raman spectra.

In Chapter 5, the iron phthalocyanine mixed nanographenes were synthesized by the in-liquid plasma using the ethanol, the 1-propanol and the 1-butanol. Then, their catalytic activity was evaluated. As a result, the high catalytic activity was obtained in iron phthalocyanine mixed nanographene synthesized with an ethanol. It was found that the amount of nitrogen contained in alcohol species was different. The author discussed

Chapter 1

the relationship between the results and catalytic activity.

Finally, the results and discussion in the present study are summarized, and the future scopes are described in Chapter 6.

Reference

- [1] H. W. Kroto, J. R. Heath, S. C. O'brien, R. F. Curl, and R. E. Smally, *Nature* **318** (1985) 163.
- [2] E. Ozawa, *Kagaku* **25** (1970) 854.
- [3] M. Maggini and G. Scorrano, *J. Am Chem. Soc.* **115** (1993) 9798.
- [4] C. Thilgen and F. Diederich, *Chem. Rev.* **106** (2006) 5049.
- [5] A. Cravino and N. S. Sariciftci, *J. Mater. Chem.* **12** (2002) 1931.
- [6] R. Bakry, R. M. Vallant, M. Najam-ul-Haq, M. Rainer, Z. Szabo, C. W Huck, G. K. Bonn, *Int J Nanomedicine.* **2** (2007) 639.
- [7] S. S. Babu, H. Mohwald and T. Nakanishi, *Chem. Soc. Rev.*, 2010, **39**, 4021
- [8] S. Iijima, *Nature* **354** (1991) 56.
- [9] S. Iijima and T. Ichihashi, *Nature* **363** (1993) 603.
- [10] J. Kong, N.R. Franklin, C. Zhou, M.G. Chapline, S. Peng, K. Cho, and H. Dai, *Science* **287** (2000) 622.
- [11] S. Belluci, *Physical Status Solidi C*, **2** (2005) 34.
- [12] H.G. Chae, S. Kumar, *Journal of Applied Polymer Science*, **100** (2006) 791.
- [13] M. Meo, M. Rossi, *Composites Science and Technology* **66** (2006) 1597.
- [14] A. Bianco, K. Kostarelos and M. Prato, *Current Opinion in Chemical Biology* **9** (2005) 674.
- [15] G. G. Wildgoose, C. E. Banks, and R.G. Compton, *Small.* **2** (2006) 182.
- [16] J. M. Schnorr and T. M. Swager, *Chem. Mater.* **23** (2011) 646.
- [17] M. F. L. D. Volder, S. H. Tawfick, R.H. Baughman, and A. J. Hart, *Science.* **339** (2013) 535.
- [18] K. S. Novoselov, A. K. Geim, S. V. Morozov, D. Jiang, Y. Zhang, S. V. Dubonos, I.

- V. Grigorieva, and A. A. Firsov: *Science* **306** (2004) 666.
- [19] K. S. Novoselov, A. K. Geim, S. V. Morozov, D. Jiang, M. I. Katsnelson, I. V. Grigorieva, S. V. Dubonos, and A. A. Firsov, *Nature* **438** (2005) 197.
- [20] Y. Zhang, Y. W. Tan, H. L. Stormer, and P. Kim, *Nature* **438** (2005) 201.
- [21] Y. Zhu, S. Murali, W. Cai, X. Li, J. W. Suk, J. R. Potts, and R. S. Ruoff, *Adv Mater.* **22** (2010) 5226.
- [22] L. Chen, Y. Hernandez, X. Feng, and K. Mullen, *Angew. Chem. Int. Ed.* **51** (2012) 7640.
- [23] A. Reina, X. Jia, J. Ho, D. Nezich, H. Son, V. Bulovic, M. S. Dresselhaus, and J. Kong, *Nano Lett.* **9** (2009) 30.
- [24] W. S. Hummers Jr, and R. E. Offeman, *J. Am. Chem. Soc.* **80** (1958) 1339.
- [25] S. Nomura, and H. Toyota, *Appl. Phys. Lett.* **83** (2003) 22.
- [26] Y. Li, Q. Chen, K. Xu, T. Kaneko, R. Hatakeyama, *Chemical Engineering Journal* **215** (2013) 45.
- [27] T. Shirafuji, Y. Noguchi, T. Yamamoto, J. Hieda, N. Saito, O. Takai, A. Tsuchimoto, K. Nojima, and Y. Okabe, *Jpn. J. Appl. Phys.* **52** (2013) 125101.
- [28] C. Richmonds and R. M. Sankarana, *Appl. Phys. Lett.* **93** (2008) 131501.
- [29] B. J. Lee, and G. H. Jeong, *Current Applied Physics.* **15** (2015) 1506.
- [30] T. Hagino, H. Kondo, K. Ishikawa, H. Kano, M. Sekine, and M. Hori, *Appl. Phys. Express* **5** (2012) 035101.
- [31] M. Z. Jacobson, W. G. Colella, and D. M. Golden, *Science* **308** (2005) 1901.
- [32] T. E. Springer, T. A. Zawodzinski and S. Gottesfeld, *J. Electrochem. Soc.* **138** (1991) 2334.
- [33] L. Qingfeng, H.A. Hjuler, and N.J. Bjerrum, *Journal of Applied Electrochemistry.*

31 (2001) 773.

[34]B. C. H. Steele and A. Heinzl, *Materials for Sustainable Energy*. (2010) 224.

[35]R. M. Ormerod, *Chem. Soc. Rev.* **32** (2003) 17.

[36]B. C. H. Steele, and A. Heinzl, *Nature* **414** (2001) 345.

[37]S. D. Knights, K. M. Colbow, J. St-Pierre, and D. P. Wilkinson, *J. Power Sources* **127** (2004) 127.

[38]V. Mehta, and J. S. Cooper, *J. Power Sources* **114** (2003) 32.

[39]T. Matsumoto, T. Komatsu, K. Arai, T. Yamazaki, M. Kijima, H. Shimizu, Y. Takasawa, and J. Nakamura, *Chem. Commun.* **7** (2004) 840.

[40]T. Yoshitake, Y. Shimakawa, S. Kuroshima, H. Kimura, T. Ichihashi, Y. Kubo, D. Kasuya, K. Takahashi, F. Kokai, M. Yudasaka, and S. Iijima, *Physica B*, **323** (2002) 124.

[41]S. Litster, and G. McLean, *J. Power Sources* **130** (2004) 61.

[42]M. Hara, M. Lee, C. H. Liu, B. H. Chen, Y. Yamashita, M. Uchida, H. Uchida, and M. Watanabe, *Electrochim. Acta* **70** (2012) 171.

[43]D. A. Stevens, M. T. Hicks, G. M. Haugen, and J. R. Dahn, *J. Electrochem. Soc.* **152** (2005) 2309

[44]F. A. de Bruijn, V. A. T. Dam, and G. J. M. Janssen, *Fuel Cells* **8** (2008) 3

[45]A. Taniguchi, T. Akita, K. Yasuda, and Y. Miyazaki, *J. Power Sources* **130** (2004) 42.

[46]S. Bhaviripudi, X. Jia, M. S. Dresselhaus, and J.Kong, *Nano Lett.* **10** (2010) 4128.

[47]M. Hara, M. Lee, C. H. Liu, B. H. Chen, Y. Yamashita, M. Uchida, H. Uchida, and M. Watanabe, *Electrochim. Acta* **70** (2012) 171.

[48]X. Wang, W. Li, Z. Chen, M. Waje, and Y. Yan, *J. Power Sources* **158** (2006) 154.

- [49] S. K. Natarajan, and J. Hamelin, *J. Electrochem. Soc.* **156** (2009) B210.
- [50] A. Kongkanand, S. Kuwabata, G. Girishkumar, and P. Kamat, *Langmuir* **22** (2006) 2393.
- [51] Y. Shao, S. Zhang, C. Wang, Z. Nie, J. Liu, Y. Wang, and Y. Lin, *J. Power Sources* **195** (2010) 4600.
- [52] F. Jaouen, E. Proietti, M. Lefèvre, R. Chenitz, J. P. Dodelet, G. Wu, H. T. Chung, C. M. Johnston, and P. Zelenay. *Energy Environ. Sci* **4** (2011)114.
- [53] R. Bashyam, and P. Zelenay. *Nature* **443** (2006) 63.
- [54] M. Lefèvre, E. Proietti, F. Jaouen, and J.P. Dodelet. *Science* **324** (2009)71.
- [55] Z. Chen, D. Higgins, A. Yu, L. Zhang, and J. Zhang. *Energy Environ. Sci* **4** (2011) 3167.
- [56] R. Jasinski. *Nature* **4925** (1964)1212.
- [57] C. W. B. Bezerra, L. Zhang, K. Lee, H. Liu, A. L. B. Marques, E. P. Marques, H. Wang, J. Zhang. *Electrochimica Acta* **53** (2008) 4937.
- [58] R. Chen, H. Li, D. Chu, and G. Wang. *J. Phys. Chem. C* **113** (2009) 20689.
- [59] A. Morozan, S. Campidelli, A. Filoramo, B. Jusselme, S. Palacin. *Carbon* **49** (2011) 4839.
- [60] C. Zhang, R. Hao, H. Yin, F. Liu, and Y. Hou. *Nanoscale* **4** (2012)7326.
- [61] G. Dong, M. Huang, and L. Guan. *Phys. Chem. Chem. Phys* **14**(2012)2557.
- [62] R. Othman, A.L. Dicks, and Z. Zhu. *Int. J. Hydrogen Energy* **37** (2012) 357.
- [63] S. Pylypenko, S. Mukherjee, T. S. Olson, P. Atanassov. *Electrochimica Acta* **53** (2008) 7875.
- [64] H. Niwa, M. Saito, M. Kobayashi, Y. Harada, M. Oshima, S. Moriya, K. Matsubayashi, Y. Nabaie, S. Kuroki, T. Ikeda, K. Terakura, J. Ozaki, and S. Miyata.

Journal of Power Sources **223** (2013) 30.

Chapter 2

Experimental setup and evaluation methods of nanographene

2.1 Synthesis of nanographene

2.1.1 In-liquid plasma method

The liquid plasma used in this laboratory adopts the micro hollow cathode method [1-3]. The upper electrode is an electrode using a micro hollow cathode, and the tip of the upper electrode is cylindrical. By applying a voltage to the electrode, electrons are emitted from the inside of the electrode and accelerated to the inside of the opposing electrode. Electrons arriving at the opposite side are repelled by the electric field in the opposite direction, and electron acceleration occurs in the opposite direction. By repeating the repulsion of electrons inside such an electrode, electrons are repeatedly collided with neutral particles and the discharge is maintained. Due to the discharge of this micro hollow cathode type, the current density in the discharge becomes higher than the ordinary discharge, and the discharge sustaining current becomes low. In this study, a non-equilibrium atmospheric plasma having a high electron density or more is generated in the micro hollow region at the tip of the upper electrode.

The experimental setup and the experimental procedure are shown. Figure 2-1 is a

schematic diagram of the in-liquid plasma device. Ar gas with a flow rate of 6 slm was introduced and filled the gas region at the upper half of the reactor. The pressure was maintained at atmospheric pressure. These electrodes were positioned so as to sandwich the gas-liquid boundary. One electrode, the upper one, was placed in the gas phase. The other, lower electrode was immersed in the liquid phase. More specifically, the tip of the upper electrode was placed 1 mm above the liquid level. The 100-mm-long wire that was used as the lower electrode was immersed 9 mm below the liquid level in the alcohol. As shown in Figure 2-2, 9 kV was applied to the upper electrode and the lower electrode facing each other via the liquid level of various alcohols with a 60 Hz AC power source to generate the in-liquid plasma. There are various metal materials for electrode materials, but copper having a report that nanographene having high crystallinity is synthesized [4]. The upper gas phase electrode has a micro hollow cathode structure, and the generated non equilibrium atmospheric pressure plasma reaches the lower liquid phase electrode. It is considered that the alcohol is decomposed using this liquid phase as a reaction field, and nanographenes are formed.

After the syntheses, the suction filtration with a filter (Millipore JAWP04700) collected solid materials as the synthesized compounds. The weights of the products were measured by an electronic balance.

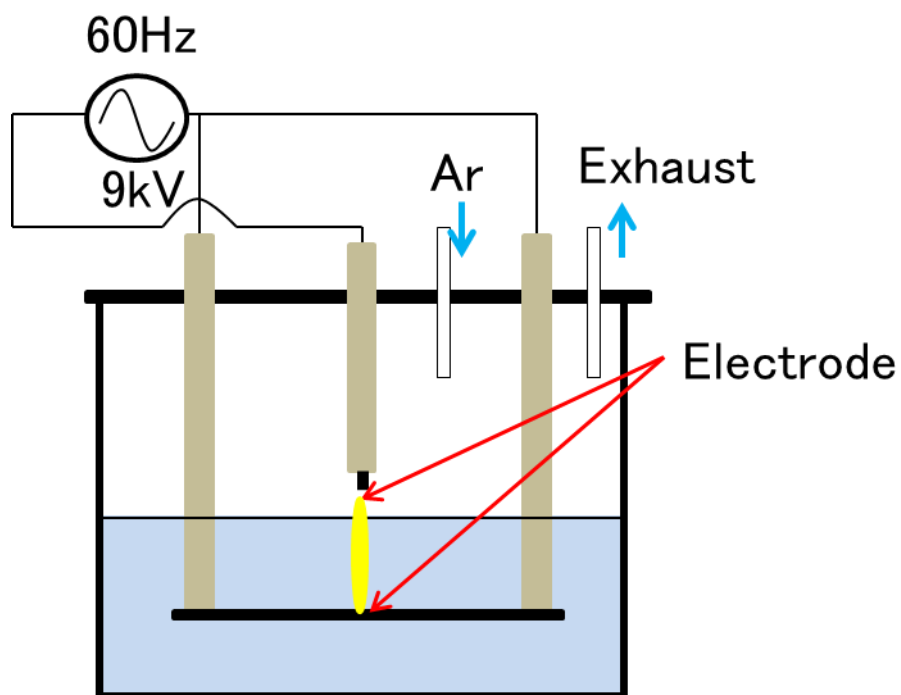


Fig. 2-1 In-liquid plasma device.

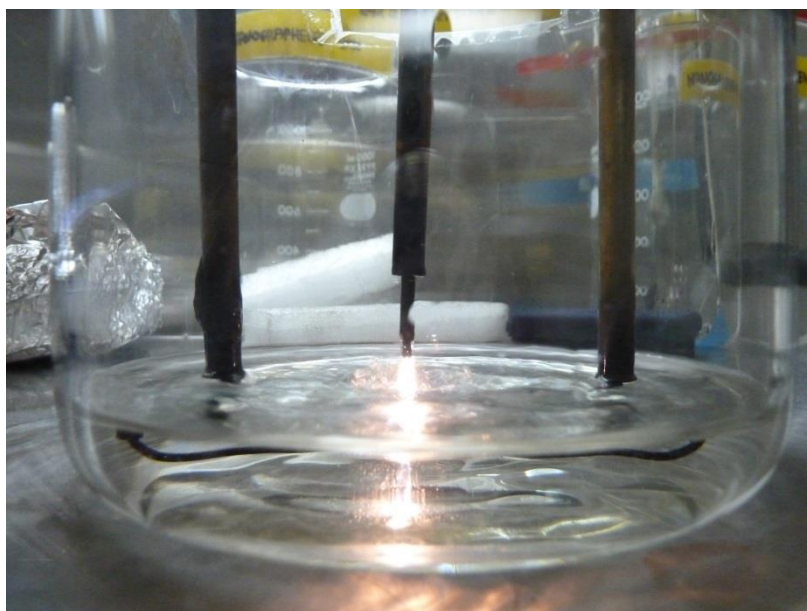


Fig. 2-2 State of plasma discharge in the liquid.

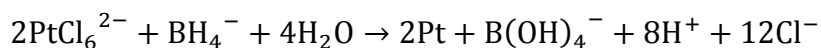
2.1.2 Hydrogen peroxide treatment

As a surface treatment after the production of carbon nanomaterials, the hydrogen peroxide water treatment for carbon nanotubes is well known [5]. It has been reported that catalytic metals and amorphous carbon components attached to the surface of carbon nanotubes before the treatment are removed by the hydrogen peroxide treatment and carbon nanotubes [6]. The bundles are separated by dispersion of each single nanotube [6]. The catalytic metals and amorphous carbon components have been removed by the oxidation reaction with hydrogen peroxide. The same treatment can be carried out with an aqueous acid solution or the like having a higher oxidizing power than the hydrogen peroxide solution, but in these cases, not only the catalytic metal and the amorphous carbon component but also the carbon nanotube itself can be damaged. Therefore, the selective removal of catalytic metals and amorphous carbon components can be realized by using the hydrogen peroxide having the weak oxidizing power in comparison.

In analogy for the effectiveness in the carbon nanotube treatments, the author have tried to remove the amorphous carbon components by the hydrogen peroxide water treatment of the nanographene material synthesized by using the in-liquid plasma. The collected material was a composite of amorphous carbon and nanographenes. The amorphous component was removed by immersing the filtrates in hydrogen peroxide (30% H_2O_2) at a temperature of 120°C for 120 min [3]. After this H_2O_2 treatment, the compounds were collected again by suction filtration. The Raman spectra before and after the H_2O_2 treatments were essentially observed with similar D and G bands, regardless of the amorphous carbons that were removed.

2.1.3 Platinum nanoparticle supporting method

The liquid phase reduction method was used supporting on the nanographenes. A hexachloroplatinic acid was used as a precursor for precipitating platinum nanoparticles. An example of the chemical reaction formula in the reduction reaction is shown below.



The platinum nanoparticles are grown by reducing the precursor with the reducing agent [7].

Supporting nanoparticles on a carbon material, the carrier is dispersed in a solution and then administered in the order of precursor after reducing agent. When this order is reversed, it is reduced at the moment when the precursor of platinum is charged, and platinum of black fine powder called platinum black appears, and it agglomerates without being supported.

From this, the liquid phase reduction method is well known as it can produce catalyst particles easily.

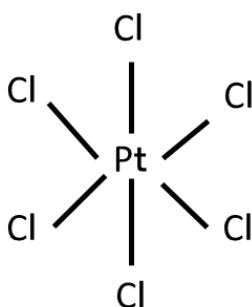


Fig. 2-3 Chloroplatinic acid.

2.2 Plasma diagnostic technique

2.2.1 Optical Emission spectroscopy (OES)

Generally, plasma is optically observed by light emission from excited species in plasma. Emission spectroscopic measurement is simple. It is widely used for measurement in process plasma. In the plasma, particles such as charged and neutral particles, electrons and ions, existing in the plasma collide with each other. Electrons collide with the particles such as atoms, molecules, and radicals. The particles at the electronic excited level emit light of a specific frequency by transitions to the lower level.

Energies are conserved before and after collisions. The kinetic energy of colliding particles stored and this collision is called as elastic collision. In the collisions, the kinetic energy is not preserved and this collision is called as inelastic collisions. The change in the kinetic energy before and after the inelastic collision is transferred into the internal energy of the collided particle. By inelastic collisions, excited, dissociated, or ionized particles are generated. The transitions to the lower level permit under the optical transition rule, equal to the energy difference between the upper level and the lower level. It emits photons with energy [8-11].

2.3 Evaluation methods of nanographene

2.3.1 Raman spectroscopy

Raman spectroscopy is a non-destructive and noncontact measurement with regard to any sample. The sample burning may occur if the strength of the laser is too strong. Previously it was an analysis that it was difficult to measure and it took a long time, but in recent years the performance of the equipment has improved, and structural analysis can be easily done in a short time, so it is actively used in industrial materials.

The measurement depth of the Raman spectrum is dominated by the absorption by the sample of the laser light and the Raman scattering light used as the light source. Since the absorption of carbon material in the visible light region is extremely large except for diamond, the measurement depth is as shallow as several tens of nm, and Raman spectroscopy is practically a surface analysis method. Therefore, it is necessary to pay attention to contamination of the sample surface and handling of the sample. Particularly since the Raman spectrum is extremely sensitive to structural disturbances, it is extremely difficult to grind and the structure may be changed only by pushing the sample or rubbing it.

In nanocarbons, various carbons such as graphite and carbon black from sp^2 type carbon such as coal and pitch, sp^3 type carbon such as diamond and diamond like carbon film, graphite intercalation compound, fullerene, carbon nanotube, carbon having sp^2 bonds. Since the Raman spectrum sensitively reflects the structure of the carbon material, X-ray diffraction, transmission electron microscopy, etc. together with the Raman spectra become a powerful evaluation method of the carbon material.

When the graphite structure is disturbed, Raman bands are observed at 1340 and

1620 cm^{-1} in addition to the Raman band of 1580 cm^{-1} and 2700 cm^{-1} , and the disorder of the structure becomes large, and as compared with the Raman band of 1580 cm^{-1} in these bands It is well known that the relative strength increases and it becomes a broad band shape as a whole. The bands of 1340 and 1620 cm^{-1} are attributable to the disorder of the structure, and the bands of D band (1340 cm^{-1}) and D 'band (1620 cm^{-1}) and D band (1620 cm^{-1}) are used for G band (1580 cm^{-1}) inherent to graphite [12-13]. Thus, the Raman spectrum of graphite is extremely sensitive to structural defects unlike other compounds in other compounds, and is useful as a method for evaluating carbon materials.

In addition, it has been reported that the nanographene domain size can be obtained from the peaks of the G band and the D band in the present nanographene. This is a study of a sample in which graphene is made nano-sized by using Raman spectroscopy and transmission electron microscopy to investigate the correlation due to the difference in domain size. As a result, the following formula was derived [14].

$$L_a(\text{nm}) = (2.4 \times 10^{-10})\lambda_1^4 \left(\frac{I_D}{I_G}\right)^{-1}$$

The Raman spectrum in carbon is shown in Figure 2-4. In addition, nanographene is susceptible to spectral effects due to shape due to edge surface. Specifically, on the edge surface, the relative intensity of the band of 1340 and 1620 cm^{-1} with respect to 1580 and 2700 cm^{-1} . As the Raman bands intensity increases, but the full width at half maxima of the Raman band of 1580 cm^{-1} were substantially same. The size of the nanographene is small.

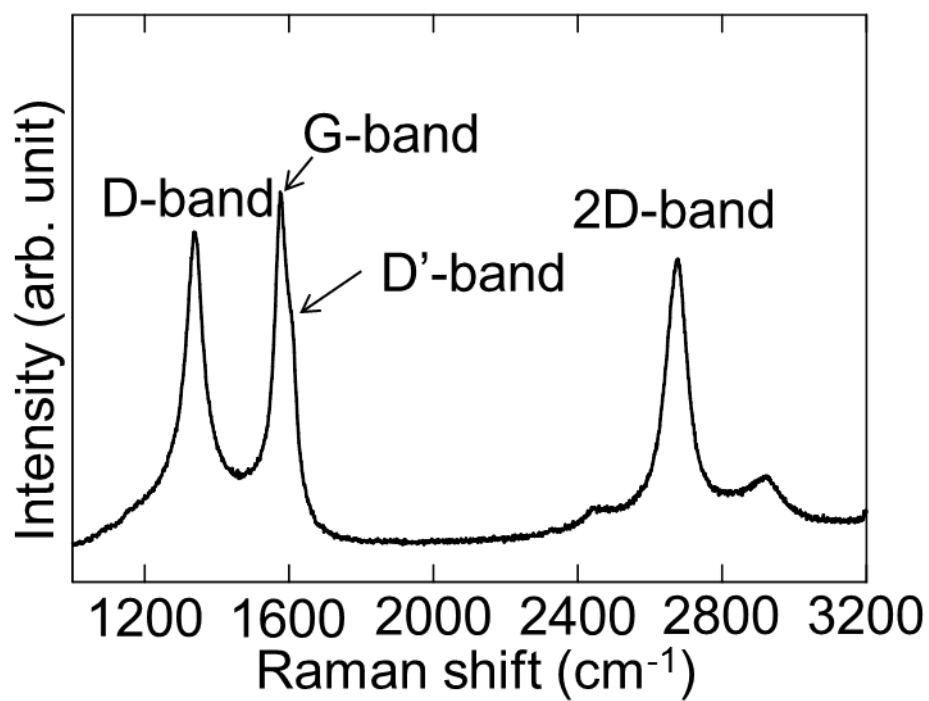


Fig. 2-4 Raman spectra of nanographenes with ethanol.

2.3.2 X-ray diffraction (XRD)

X-rays are the same electromagnetic waves as visible light, and the wavelength is approximately 0.01 to 100 Å (0.001 to 100 nm). In the X-ray generator used in ordinary powder X-ray diffractometer, X-rays are obtained by colliding electrons with the target. In this case, the obtained X-ray spectrum has two types of continuous X-rays and characteristic X-rays. In general, powder X-ray diffraction measurements are performed using characteristic X-rays. The wavelength of the characteristic X-ray is closely related to the structure of the electron orbit of the element constituting the target material, and it has a value unique to each element. Those in which atoms or atomic groups are periodically arranged and spatial lattices are formed at intervals of several Å is referred to as crystals. When X-rays having the same kind of wavelength as the intervals of atoms constituting this crystal are incident, the X-ray becomes strongly scattered in a specific direction. This phenomenon is called diffraction.

As shown in Figure 2-4, when the X-ray of a wavelength enters the atomic arrangement plane at an angle θ with respect to the atomic arrangement plane with the interplanar spacing d , if the scattering angle is equal to the incident angle. The X-ray radiation phases are uniform, and the waves interfere and strengthen each other. If the optical path difference $2 d \sin \theta$ of each scattered wave by a certain surface and the surface adjacent thereto is equal to an integral multiple of the wavelength, given by

$$2 d \sin \theta = n \lambda ,$$

where, n is a positive integer, λ is a wavelength, d is an interval between lattice planes, and θ is a viewing angle (supplementary angle of incidence angle). These scattered waves intensify each other in phase and diffraction occurs. The condition of the formula

is called the Bragg condition, and when the crystal is irradiated with X-rays, if the Bragg condition is satisfied, the X-ray diffracts in a specific direction. As can be seen from the Bragg's condition, if $\lambda \leq 2d$, no diffraction occurs.

Crystallite size measurement is also often used as an evaluation method that is often used to know characteristics of a catalyst, which is an important factor in a fuel cell. This is based on the equation that gives the relationship between the spread of the diffraction line width and the crystallite diameter by utilizing the fact that the width of the diffracted X-ray diffuses when the crystallite size in fine powder X-ray diffraction is small (usually 100 nm or less) And calculating the crystallite diameter. As shown in Figure 2-5, the crystallite size is determined by correcting the spread of the diffraction X-ray width by the optical system, so that only the crystallite diameter, or the crystallite diameter and the spread of the diffraction X-ray width due to inhomogeneous strain Calculate and calculate. Calculations up to the calculation of the crystallite diameter by performing these corrections are included as a series of procedures in a commercially available analysis program, so values can be calculated comparatively easily by using these. Next, a representative calculation method will be shown. In this method, the crystallite diameter is calculated from the spread of the width of the corrected diffracted X-ray using the following equation derived by Scherrer [15]. This equation is derived by using a Gaussian exponential function which is convenient for calculation instead of the Laue function expressing the intensity of the diffraction function and further simplifying it under certain conditions. The calculated latitude crystallite diameter has an error according to the degree of nonuniform distortion with respect to a substance having a spread of diffraction X-ray width due to nonuniform distortion. Generally, when the width of the diffracted X-ray depends only on the crystallite diameter, the

Chapter 2

crystallite diameter in both exponential directions of the diffracted X-ray is obtained by the formula.

$$D = (K \cdot \lambda) / (\beta \cdot \cos\theta)$$

D is the particle diameter, K is a constant, λ is the wavelength of the measurement X-ray, β is the half-width of the diffracted X-ray, and θ is the Bragg angle of the diffracted X-ray.

The XRD patterns were obtained with R-AXIS7 FR-E (Rigaku Corporation, Japan) instrument operating at 45 kV and 45 mA using CuK line ($k = 0.15418$ nm). The camera length is 70 mm. A mark tube with diameter 0.5 mm and inner diameter 0.01 mm was used as a sample holder.

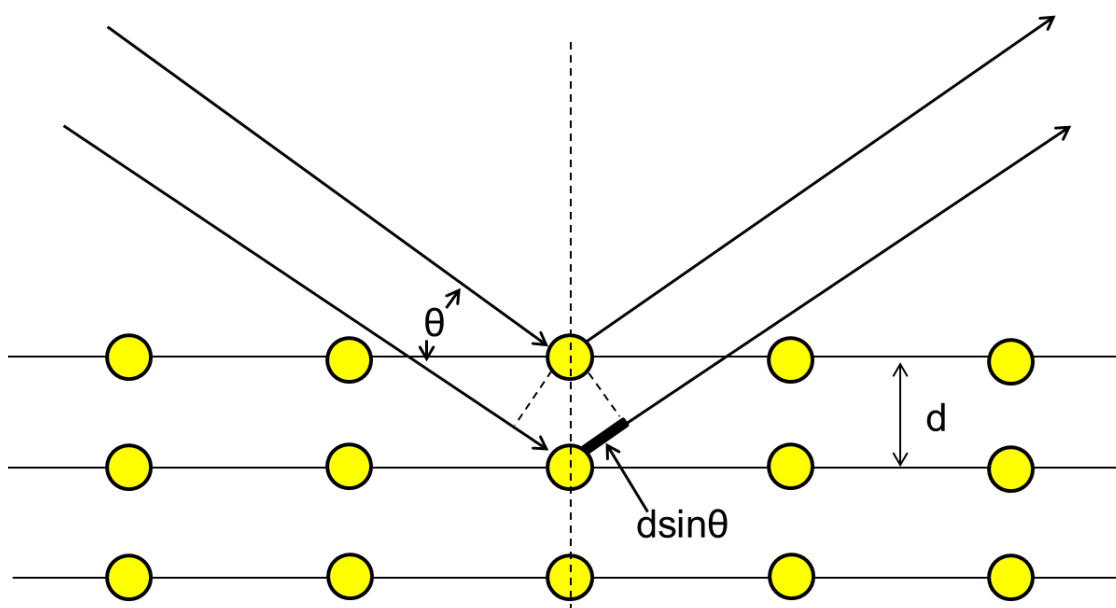


Fig. 2-4 Bragg's condition.

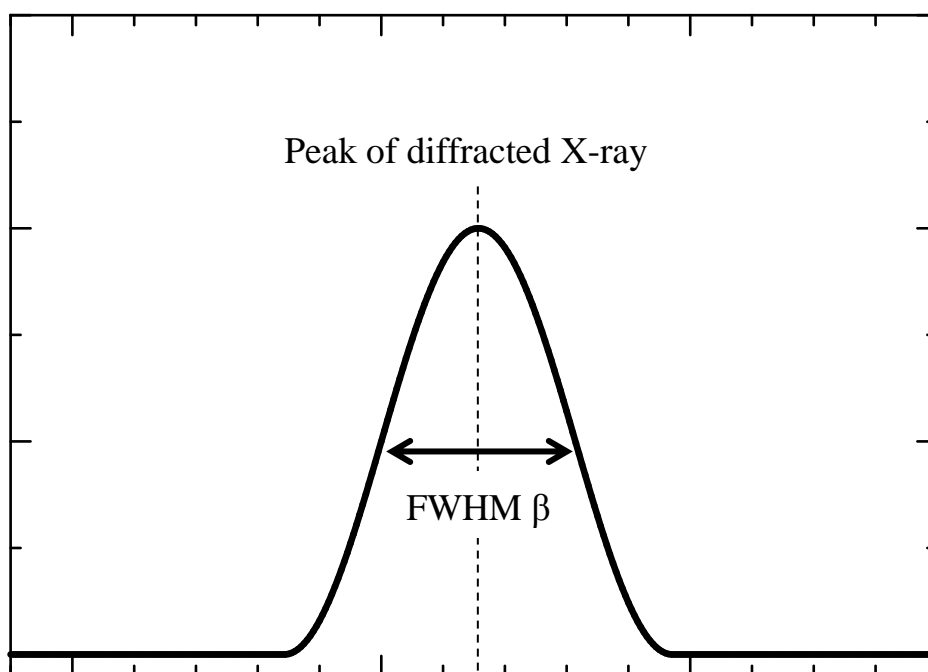


Fig. 2-5 Particle size derivation by XRD.

2.3.3 Scanning electron microscopy (SEM)

The properties of carbon nanomaterials are important not only from an academic point of view, but also from the standpoint of manufacturing and application, to observe the structure of this group of crystallites, that is, the fine structure. Observation with a scanning electron microscope (SEM) is easy to prepare a sample and can be observed from low magnification to high magnification, so that the entire sample can be uniformly observed.

When accelerated electrons are irradiated on a substance (sample), secondary electrons, reflected electrons, X-rays, cathode luminescence and the like are emitted from the surface of the sample (Figure 2-6). Electrons with energy less than 50 eV are called secondary electrons. From this, secondary electrons are generated even in deep inside the sample, but only those generated in the extremely close (~ 10 nm) of the sample surface can jump out from the surface into the vacuum. Therefore, by detecting the secondary electrons, it is possible to obtain information indicating the shape (unevenness) of the surface and the distribution of the material.

An electron beam made of an electron gun converges to a beam diameter of 10 nm or less with a focusing lens and an objective lens. Using the deflection coil, this electron beam is two-dimensionally scanned on the sample surface. Secondary electrons generated from the sample surface are converted into electric signals by a detector. This electric signal is amplified and sent to a cathode ray tube in synchronization with the electron beam of the lens barrel, and a two-dimensional scan image is obtained by the same method as that of the television.

On the other hand, the resolution of the SEM is 0.5 nm, and it is impossible to

directly observe atoms and hexagonal plane. Also, generally, for light element materials such as carbon materials, the incident beam abnormally diffuses inside the sample and the performance of the SEM can not be fully exhibited. The spatial resolution in SEM observation is generally determined by the beam diameter. However, when the observation sample is a carbon material, in most cases it can only be observed with lower resolution than the highest resolution of the device. For light element materials such as carbon materials, the incident electron beam penetrates deeper than metal. For this reason, incident electrons penetrate from the surface of the sample to the inside of the sample, and generate secondary electrons including information other than the surface of the sample and backscattered electrons. Therefore, in terms of faithfully observing the shape (unevenness) of the surface, the ratio of the signal-noise (SN) to the signal becomes large, which causes a reduction in the resolution. As the accelerating voltage of the electron beam is increased, the penetration depth and spread of incident electrons increase, so the SN ratio decreases and the resolution decreases. On the other hand, the electron beam diameter that can be narrowed decreases as the acceleration voltage increases, and the resolution improves. When the acceleration voltage is lowered, the diffusion region of the electron beam becomes small and the S / N ratio of the image improves, but the electron beam diameter that can be narrowed becomes large. For these reasons, in order to faithfully observe the surface shape (irregularities) for each sample to be observed, it is necessary to select an optimum acceleration voltage.

Figure 2-7 shows the SEM image of nanographenes. The observation condition was an acceleration voltage 10 kV, and the irradiation current was 10 μ A. Aggregates in the order of several tens of nanometers are observed. It is thought that each one of these were nanographenes.

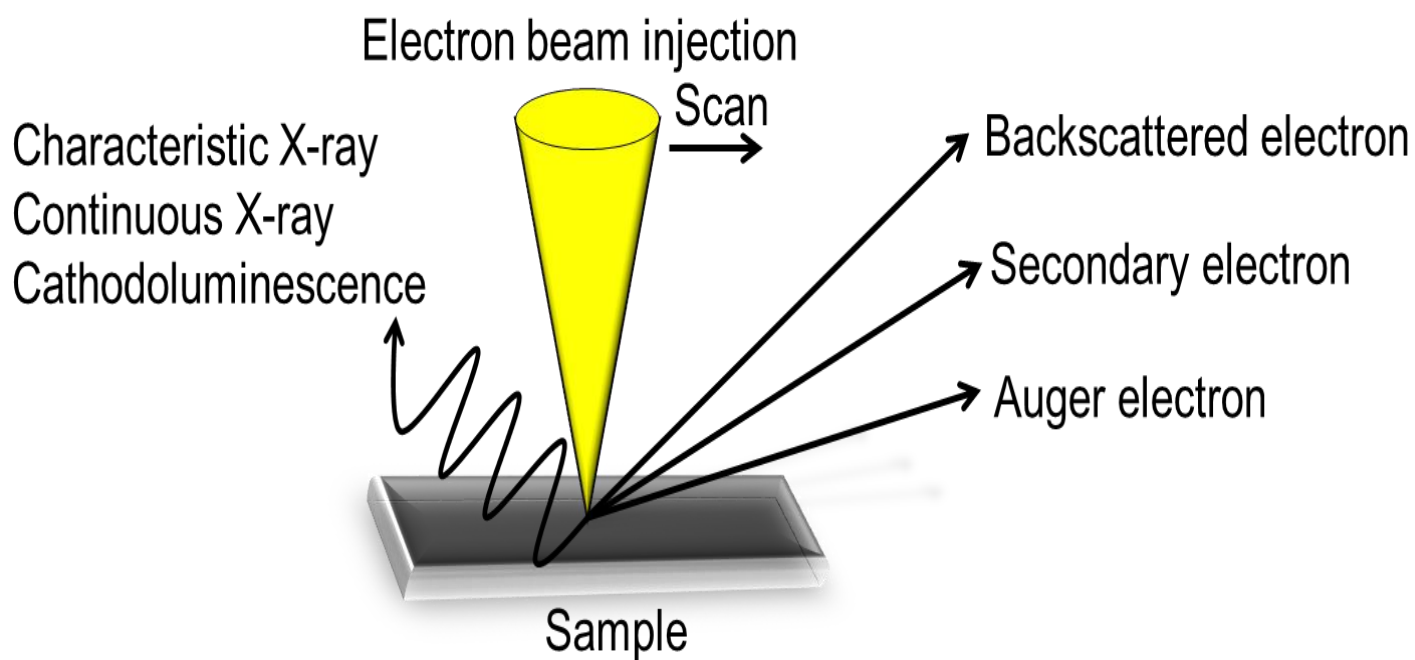


Fig. 2-6 Principle of SEM.

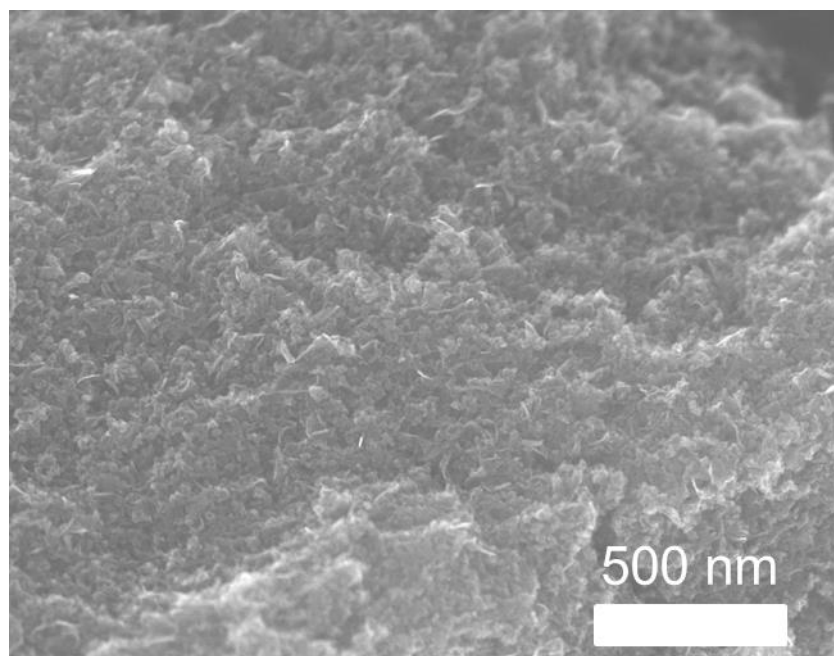


Fig. 2-7 SEM image of nanographene.

2.3.4 Transmission electron microscopy (TEM)

The observation by a transmission electron microscope (TEM), it can be grasped visually from the entire sample to such local organizations or orientation. Especially, observation with a high resolution transmission electron microscope makes it possible to observe a region of nanometer or less, which is a very effective means for structural analysis at the atomic level.

The imaging path of the TEM consists of multistage electronic lenses (Converging Lens, Objective Lens, Intermediate Lens, Projector Lens) (Figure 2-8). Increase the electron acceleration voltage of the electron gun and heat the filament to generate the electron beam. The accelerating voltage is generally from several tens of kV to several hundred kV, and some exceeding 1,000 kV. As shown by the following equation, the de Broglie wavelength λ of the electron beam becomes shorter as the acceleration voltage is higher, so that the energy of electrons is increased, the permeability to the sample is increased, and the resolution is improved.

$$\lambda \text{ (nm)} = \frac{h}{\sqrt{2meV\left(1 + \frac{eV}{2mc^2}\right)}} \approx \frac{0.03878}{\sqrt{V(1 + 9.785 \times 10^{-4}V)}} \text{ (nm)}$$

Here, h is Plank's constant, m and e are the mass and charge magnitude of the electron, V is the accelerating voltage (kV), and c is the light velocity.

The electron beam emitted from the electron gun is collected by the converging lens and irradiated on the sample as a minute parallel light flux. In order to adjust the light quantity of the electron beam, a condenser aperture is inserted between the focusing lens and the sample. The electron beam is adjusted so that the converging diaphragm is at the center of the optical path. The electron beam which passed through

the sample reaches the objective lens, enlarging in the first stage. This enlarged image is further enlarged by the intermediate lens and projector lens, and becomes the final observation image. Therefore, the objective lens is extremely important. The objective aperture is used to increase the contrast of the image by inserting it into the back focal plane of the objective lens. The restricted selected area aperture is inserted when obtaining the electron beam diffraction image of a part of the observation image.

The final image displayed on the fluorescent screen is observed with the naked eye from the glass window or the image on the compact fluorescent screen with binoculars. Or remove the fluorescent plate, and irradiate the photographic film directly with an electron beam to expose it. There is also a device which attaches a camera instead of a fluorescent board to capture an image and displays it on a monitor screen. There is also a system that can save an image captured by a CCD camera as a digital image.

Figure 2-9 shows the SEM image of nanographenes. The nanographene structures were analyzed by TEM (JEOL JEM-2010). TEM images were taken at 200 kV acceleration of electrons. Transmission electron diffraction (TED) patterns were taken at 200 kV acceleration of electrons and camera length 0.6 m.

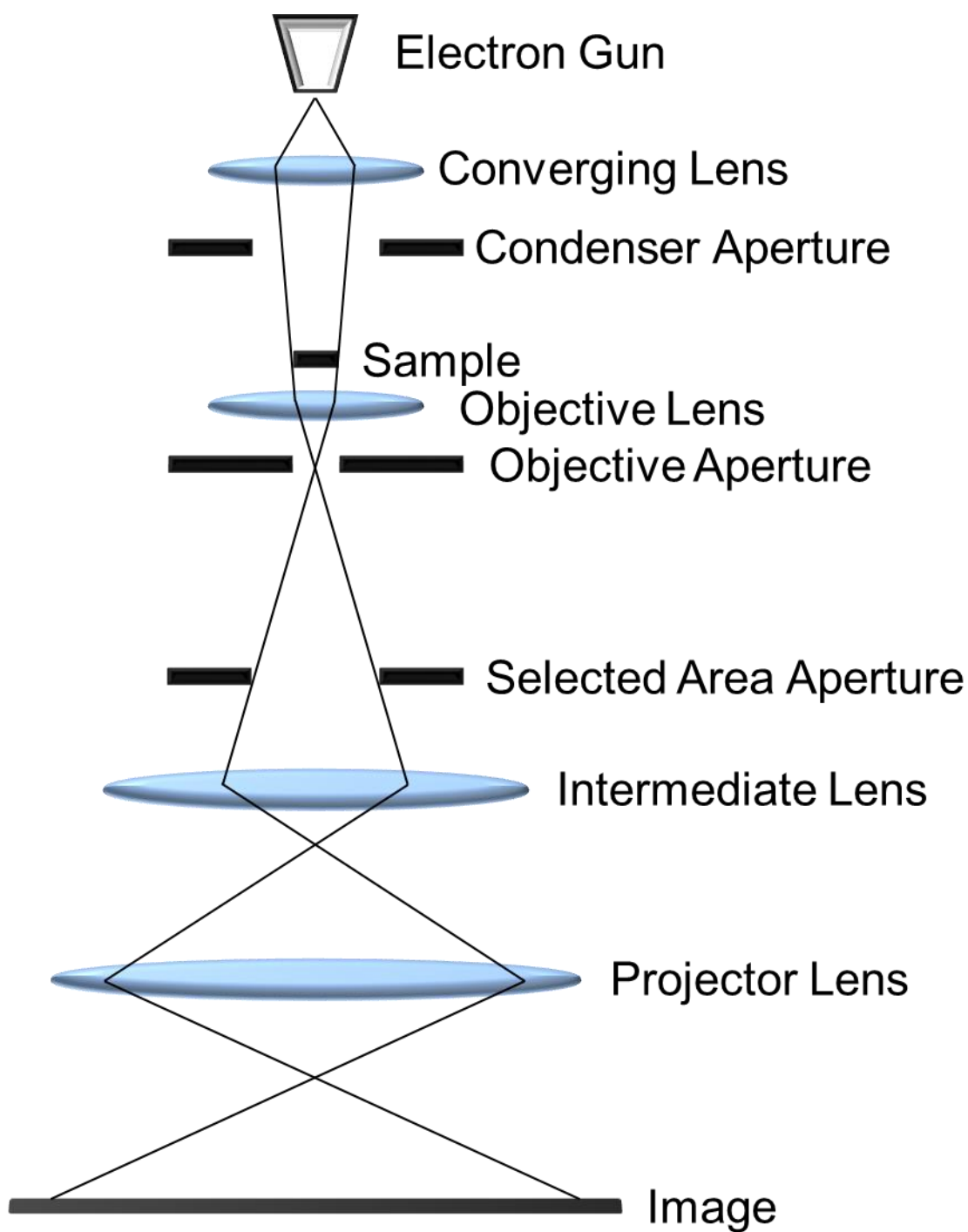


Fig. 2-8 Principle of TEM.

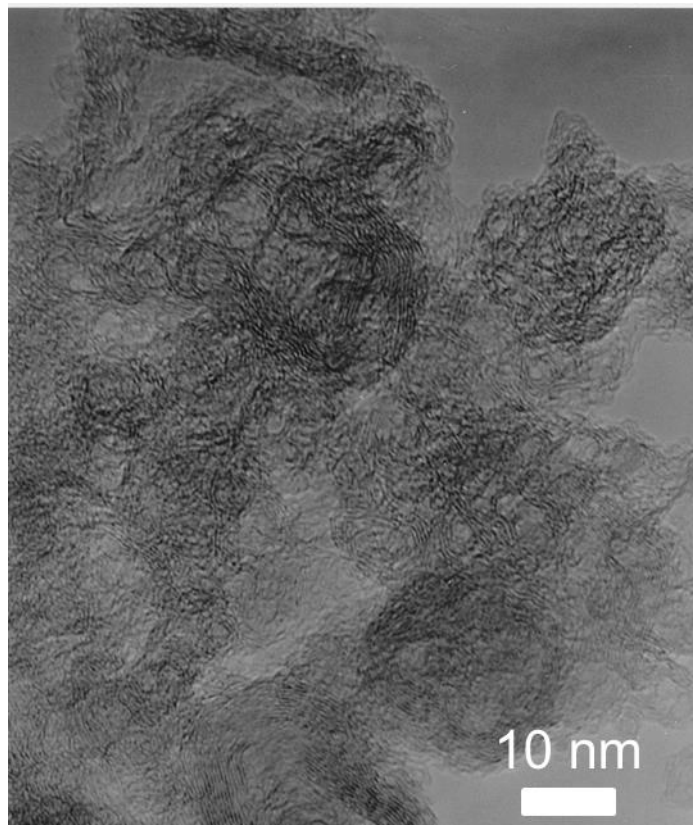


Fig. 2-9 TEM image of nanographene.

2.3.5 X-ray photoelectron spectroscopy (XPS)

X-ray photoelectron spectroscopy (XPS) is a method of measuring the spectrum of kinetic energy E_K of electrons emitted by photoionization by irradiating a substance with X-rays having a constant energy $h\nu$ in a vacuum an element constituting the surface of a substance, a chemical state of the element, and information on the existence ratio thereof.

The binding energy E_B (the Fermi level in the case of a solid) with the atomic nucleus of the element has an intrinsic value depending on the kind of the element and its orbital, but also varies depending on the chemical state (chemical shift). When a solid sample is irradiated with X-rays, electrons in orbits having an E_B smaller than $h\nu$ are emitted, and these E_{KS} are based on the energy conservation law, where ϕ is the work function of the sample. When the surface of the sample is electrically conductive and electrically coupled with the energy analyzer and becomes the ground potential, the Fermi levels of both are equal, but since the work function ϕ_s of the analyzer is not generally equal to ϕ , analysis It is the value of E_K 'that is actually measured, but ϕ_s is a constant determined by the device, so if you calibrate beforehand with a substance whose E_B is accurately known in advance E_B is obtained. Since there is a table organizing the values of E_B for each element and electron orbit, it is possible to immediately identify the element from this value. Since the line width of the X-ray directly affects the resolution of the spectrum, Al $K\alpha$ (average energy 1486.58 eV) and Mg $K\alpha$ (average energy 1253.56 eV) lines with narrow characteristic line width are used in ordinary devices. Therefore, one cannot obtain information from orbit with larger E_B than this. The mean free path (or escape depth) within the solid of released

Chapter 2

photoelectrons is determined by E_K , but since $E_K < 1486.58$ eV, the depth at which information can be obtained is inevitably limited. The inelastic mean free path λ of the electrons in the solid differs depending on the material, but it is approximately 0.4 to 3 nm in this energy range.

2.3.6 Electrochemical measurement

Electrochemical measurements are chemicals that handle the transfer of electrons between samples. Examples of electrochemical applications currently include primary batteries, secondary batteries, fuel cells, aluminum electrolysis, organic electrolysis, electrolytic refining of metals, corrosion and corrosion prevention, and the like. Among them, in fuel cells, it is used for catalytic reaction evaluation of catalytic electrodes. Figure 2-10 shows the electrochemical measurement system. In the measurement, a three electrode system using a working electrode, a reference electrode, and a counter electrode is used. In the electrochemical reaction, oxidation reaction and reduction reaction proceed simultaneously at two electrodes. Therefore, the two electrode measurement is not properly to understand electrochemical reaction at the electrode. For example, information on anode and cathode are mixed in the potential difference, and both companies can not be separated. However, if the potential of either electrode is accurately known, it is possible to estimate what kind of reaction is taking place. In order to know the potential difference of the working electrode, a potential difference with the reference electrode may be measured. However, when the reaction actually occurs at the working electrode, another reaction occurs at the counter electrode. Then the potential changes. Therefore, an auxiliary electrode is used as the third electrode. The potential of the working electrode is measured and controlled with respect to the reference electrode, but in order to maintain the accuracy of the potential, almost no current is allowed to flow through the reference electrode. However, when an oxidation reaction occurs at the working electrode, since the electrons received by the working electrode must be thrown away somewhere, a reduction reaction is caused at the counter

electrode. Such an experimental system is called a three-point electrode system.

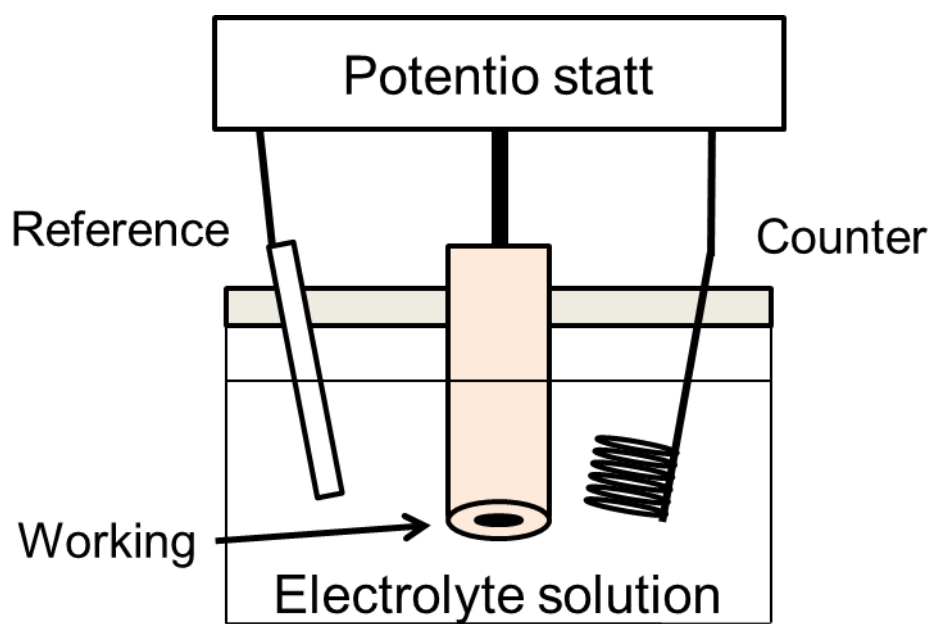


Fig. 2-10 Electrochemical measurement system.

In the case of measurement using a catalyst electrode for a fuel cell, an evaluation method called cyclic voltammetry (CV) is used. The CV method is used for initial diagnosis of the system, electrode characterization, reaction monitoring, etc. The CV method is simple and gives a lot of information, but requires careful analysis. Figure 2-11 is typically a cyclic voltammogram of a catalyst electrode for a fuel cell. A peak of hydrogen charge adsorption / desorption wave appears around 0.05 ~ 0.4 (V). This peak is a peak attributable to the magnitude of the catalytic reaction in which platinum, which is the catalyst particle, has been generated through the electrolyte solution. The peaks occurring in the vicinity of 0.8 (V) are peaks resulting from surface participation and reduction of platinum nanoparticles, respectively. The peak that we used for analysis in this measurement is a hydrogen adsorption / desorption wave occurring at 0.05 to 0.4 (V). Using the peak, the effective area (ECSA) of platinum used as a catalyst can be obtained from the following formula using the hydrogen adsorption charge amount. This is a quantification of the amount of platinum effectively used by using the magnitude of the hydrogen adsorption charge amount and the platinum content used for the measurement as a parameter.

$$\text{ECSA (m}^2\text{/g)} = \frac{\text{Electric charge amount (C)}}{2.1 \text{ (C/m}^2\text{)}} \times \frac{1}{\text{Pt content (g)}}$$

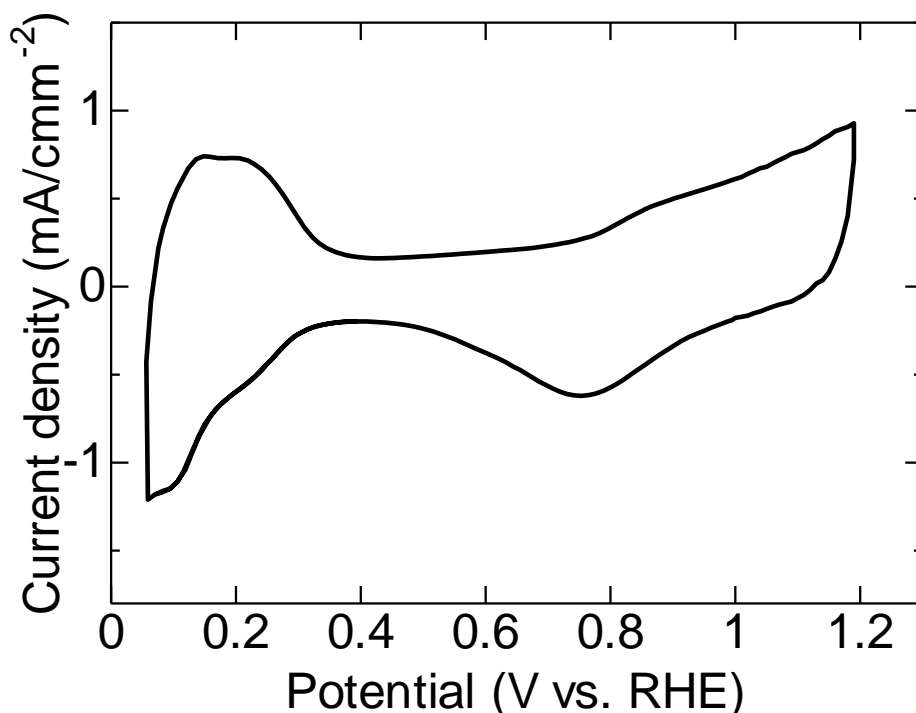


Fig. 2-11 A cyclic voltammogram of a typical fuel electrode catalyst electrode.

In the CV measurement, the reaction amount in hydrogen was measured. In fuel cells, the reaction rate of oxygen on the cathode side is about 10,000 times smaller than that of the anode, which is a problem. Therefore, the ease and the magnitude of the oxygen reduction reaction are obtained and evaluated by oxygen reduction reaction (ORR) measurement. The method quantitatively analyzes charge transfer on the electrode surface by convective voltammetry using a rotary electrode device (RDE). Figure 2-12 shows the structure of the rotating electrode and the flow of electrolyte. Embed the electrode in Teflon or glass tube on the disk and polish the electrode and the insulator to be flush with each other. Tighten the electrode and the insulator and take care not to leak the electrolyte. The author took careful wear-out the brush for reduction of any noise.

The electrode was dipped in the electrolytic solution. The solution in the vicinity of the electrode is stirred by rotation of the electrode. The movement generated vortex-like streams. The electrolytic solution was supplied the electrode surface by the vertical direction flow of electrolyte. In this way, the convection generated in the solution is faster as the number of revolutions is larger, and as a result that the influence extends to the vicinity of the electrode, the diffusion layer becomes thinner and the diffusion rate increases. As a result, the diffusion rate of reactants and products can be controlled by the rotation speed of the electrode.

In the measurement method using the stationary electrode like the CV method, the potential scanning speed is changed to analyze the diffusion and charge transfer of the substance. Also, in rotation disk electrode (RDE), it is possible to suppress the temporal change of the concentration gradient of the substance in the vicinity of the electrode and realize a constant current value regardless of the time. Voltammogram obtained by RDE is called convective voltammogram.

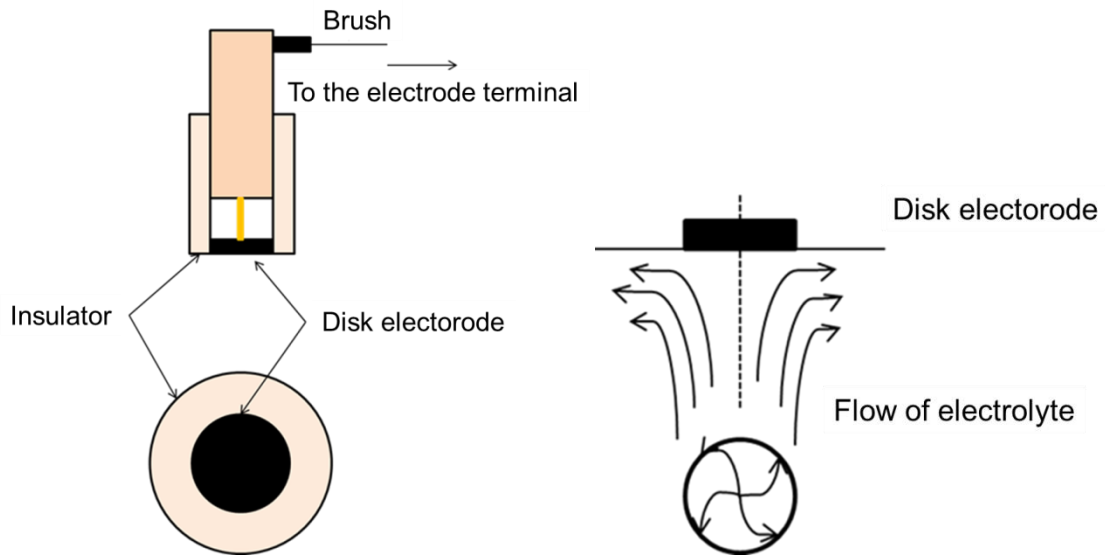
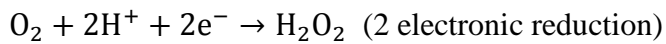


Fig. 2-12 Structure of rotating electrode and flow of electrolyte.

In the case of a catalyst electrode for a fuel cell, as described above, the electron transfer is slow. In this case, the following reaction occurs in the oxygen reduction reaction at the working electrode.



In the two-electron reduction in the fuel cell, hydrogen peroxide promotes deterioration of the catalytic electrode, so it is desirable to promote the reaction of four-electron reduction.

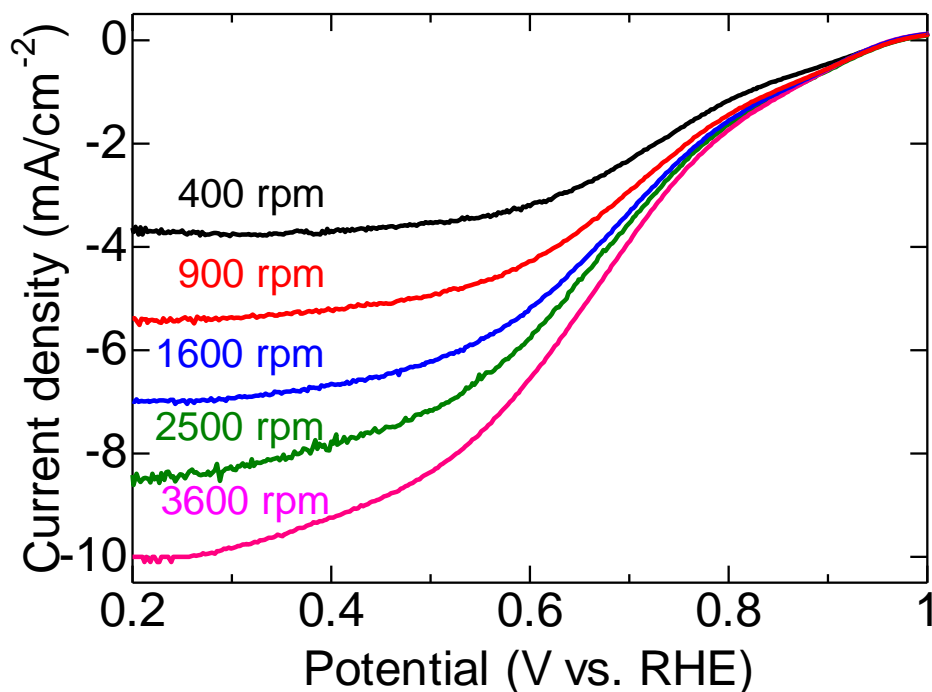


Fig. 2-13 Structure of rotating electrode and flow of electrolyte.

Lastly, the durability test assuming startup and shutdown of the fuel cell will be described [16]. This is a test assuming a high potential applied to the cathode side when the fuel cell startup is stopped. Deterioration of the catalyst carrier in the current fuel cell catalyst electrode poses a problem. In order to cycle from 1.0 to 1.5 (V) as a feature of this test, it can be evaluated separately from deterioration of platinum nanoparticles whose surface is oxidized in the vicinity of 0.8 (V). By this test, deterioration of the catalyst carrier itself is evaluated, and the effective platinum area per cycle is derived accordingly. As a flow of measurement,

- ① Wash the cell thoroughly by ultrasonic cleaning or boiling washing and pour the electrolyte adjusted to the predetermined concentration into the cell.
- ② While controlling the cell to the prescribed temperature, bubbling nitrogen into the glass cell.
- ③ CV is carried out to clean the electrode surface and measure the surface area with the electrode rotation speed set to zero.
- ④ When reproducible voltammogram is obtained, carry out the potential cycle test under the conditions as shown in Figure 2-14.
- ⑤ On the way, perform CV measurement at a frequency of 10 to 1000 cycles to obtain the electrochemical effective area (ECSA).

In case

When the potential cycle test is actually carried out, it is understood that the electric double layer in the vicinity of 0.3 to 0.6 (V) increases as the cycle number increases, and the hydrogen adsorption / desorption charge amount decreases. From this, it is considered that corrosion of carbon black is promoted in the catalyst electrode, and desorption and aggregation of platinum nanoparticles occur.

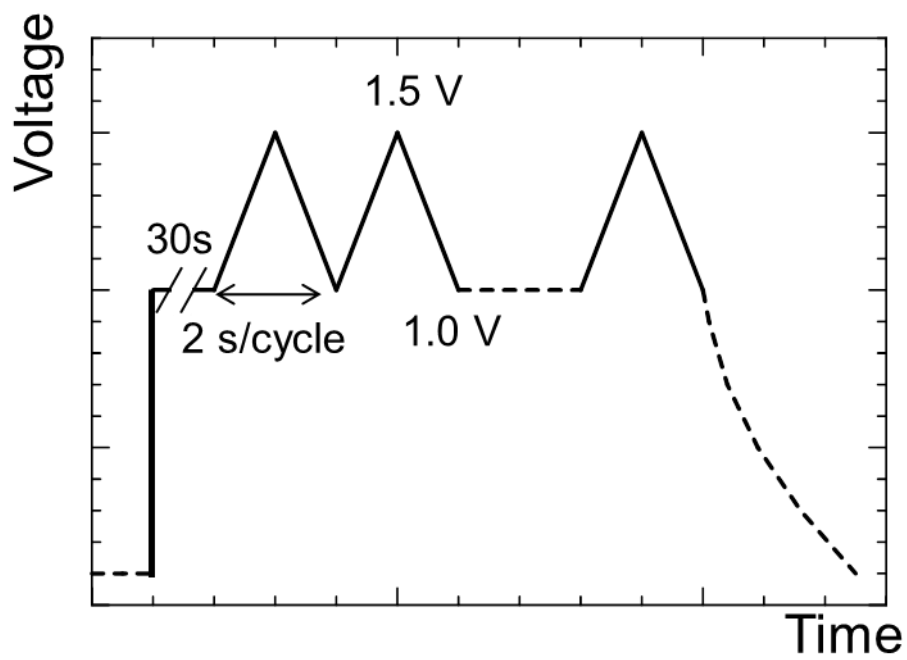


Fig. 2-14 Potential cycle test under the conditions.

Reference

- [1] M. Iwasaki, H. Inui, Y. Matsudaira, H. Kano, N. Yoshida, M. Ito, and M. Hori, *Appl. Phys. Lett.* **92**, 081503 (2008).
- [2] S. Takashima, M. Hori, T. Goto, A. Kono, M. Ito, and K. Yoneda, *Appl. Phys. Lett.* **75**, 3929 (1999).
- [3] R. H. Stark and K. H. Schoenbach, *J. Appl. Phys.* **85**, 2075 (1999).
- [4] T. Hagino, H. Kondo, K. Ishikawa, H. Kano, M. Sekine, and M. Hori, *Applied Physics Express*, **5** (2012) 035101.
- [5] Y. Feng, G. Zhou, G. Wang, M. Qu, Z. Yu, *Chemical Physics Letters* **375** (2003) 645.
- [6] Y. Peng and H. Liu, *Ind. Eng. Chem. Res.* **45** (2006) 6483.
- [7] T.C. Deivaraja, Jim Yang Leea, *Journal of Power Sources* **142** (2005) 43.
- [8] J. R. Roth, *Industrial Plasma Engineering Principles* (Institute of Physics, Berkshire, 1995).
- [9] M.A. Lieberman and A. J. Lichtenberg, *Principles of Plasma Discharges and Materials Processing* (Wiley, New York, 1994).
- [10] P. Fauchais and A. Vardelle, *IEEE Trans. Plasma Sci.*, **25**, 1258 (1997).
- [11] R. W. Smith, D. Wei and D. Apelian, *Plasma Chem. Plasma Process*, **9**, 135S
- [12] F. Tuinstra, and J. L. Koenig, *J. Phys. Chem.* **53** (1970) 1126.
- [13] R. P. Vidano, D. B. Fishbach, L. J. Willis, and T. M. Loehr, *Solid State Commun.* **39** (1981) 341.
- [14] M. A. Pimenta, G. Dresselhaus, M. S. Dresselhaus, L. G. Cancado, A. Jorio, and R. Saito, *Phys. Chem. Chem. Phys.* **9** (2007) 1276.
- [15] V. Radmilovic, H. A. Gasteiger, and P. N. Ross, *J. Catal.* **154** (1995) 98.

- [16] A. Ohma, K. Shinohara, A. Iiyama, T. Yoshida, and A. Daimaru, *ECS Trans.* 41 (2011) 775.

Chapter 3

Synthesis of nanographene and durability as catalyst electrode for fuel cell

3.1 Introduction

The author notes that the in-liquid plasma can potentially provide the rich chemistry: Relatively high-energy electrons generate atomic species such as hydrogen, oxygen, and carbon in the gas phase, and a rich variety of radicals of the precursors derived from alcohols is generated in the liquid plasma. Furthermore, reactions occur between the atomic species and precursors, yielding products in non-equilibrium states. Such a rich reaction field causes mutual reactions at the boundary layer between the gas and liquid phases. In actual syntheses, the synthesis rates strongly depended on the type of alcohol. The synthesis rate obtained using 1-butanol was roughly three times higher than that obtained using ethanol [1]. A synthesis mechanism has been proposed by the first step of ethanol to conjugated diene formation and the second step of the Diels-Alder reactions aromatic ring syntheses based on analyses of residual liquids using gas chromatography. Since the synthesized nanographene had high crystallinity in

ethanol but not butanol, this study investigates that it is potentially useful as a support material in PEFCs. Therefore, in the present study, the nanographenes synthesized by this method were assessed for use as catalyst support material with a focus on durability. The in-liquid plasma and the physicochemical structure of the nanographenes were also characterized under varying conditions, i.e. for different types of alcohol and electrode materials.

In the present study, the author investigated the relationship between the synthesis rate and the crystallinity of nanographene synthesized with the in-liquid plasma by using two types of electrodes and three types of alcohol. In the use of metallic electrodes, any electrochemical catalytic effect of incorporated metallic elements was eliminated from a comparison with all carbon conditions of the use of graphite electrodes. The durability of Pt nanoparticle supports made of nanographene was characterized by two electrochemical measurements. Cyclic voltammetry was used to measure electrochemical reactivity. High potential cycle testing, which simulates the start-and-stop operations in a fuel cell, was used to assess the stability of catalytic performance of the nanographene electrode [2]. Based on these results, the author discusses the effects of nanographene crystallinity on the durability of nanographene durability during electrochemical reactions.

3.2 Experimental details

Figure 3-1 shows a schematic of the synthesis reactor for nanographene [1]. The glass reactor, with an inner diameter of 108 mm, was filled with the 300 ml of pure alcohol. Three types of pure alcohols, *viz.*, ethanol (C_2H_5OH), 1-propanol (C_3H_7OH), and 1-butanol (C_4H_9OH), were used to synthesize nanographene. Two types of same material electrodes, a Cu or graphite wire with a diameter of 3 mm, were used in this study. The duration of discharge, which corresponded to the synthesis time, was typically one hour.

Optical emissions from the plasma were measured in the gas-phase region close to 3 mm above the liquid surface. The emissions were collected with a focusing lens (Nikon Rayfact PF 10545 MF - UV) and guided with an optical fiber to the spectrometer (ANDOR Shamrock 500i), which was equipped with an image intensifier charge-coupled device iCCD camera (ANDOR iStar). The optical emission spectra (OES) were taken using a grating of 2400 lines/mm.

The weights of both the Cu and graphite electrodes decreased upon synthesis, which indicated that both electrodes were eroded by the plasma. The synthesis yields of carbon-containing materials were estimated by subtracting the weight of the eroded electrodes.

After purification, the synthesized nanographene surfaces were loaded with Pt nanoparticles (NPs) using a liquid-phase reduction method using hexachloroplatinic acid (H_2PtCl_6 ; Sigma-Aldrich) [4-5]. The reduction for Pt NP deposition was carried out differently for each electrode. For samples differently prepared in following the two cases, the Pt-loading procedures were slight differences; however no essential difference

was obtained in the Pt-NP coating performance.

In the case of the Cu electrode, first, 30 mg of nanographene was dispersed in 50 ml of pure water using an ultrasonicator for 30 min. Next, 200 μ l of 8 wt% chloroplatinic acid in H₂O was added to the solution and held for 30 min to obtain a dispersion. Then, 10 ml of 1 M NaBH₄ as a reducing agent was added to the dispersion and stirred to mix completely at 90°C for 120 min. The Pt-NP-coated nanographenes were collected by suction filtration. The collected compounds were rinsed with pure water.

In the case using the graphite electrode, 20 mg of the nanographene was dispersed in 50 ml of pure water using an ultrasonicator for 30 min. Next, 500 μ l of 8 wt% chloroplatinic acid in H₂O, 200 μ l of 1 M NaOH as a pH-neutralizer, and 50 ml of ethylene glycol for dilution were sequentially added to the solution. The solution was mixed at 120°C for 6 h. After suction filtration, the Pt-NP-coated nanographenes were rinsed with pure water.

The contents of the metallic compounds were characterized using a thermogravimetric analyzer (Yanaco MT-6) at a combustion temperature at 1000°C under O₂ atmosphere, that the condition was different from pyrolytic graphite growth, i.e., all carbons were burned out in the highly oxidative ambience at the high temperature. After burning off the carbons, the Pt residue was weighed. In the case of the graphite electrode, the weighed Pt contents were 51.8, 51.9, and 51.7 wt% for the use of ethanol, 1-propanol, and 1-butanol, respectively. In the case using the Cu electrode, the weighed Pt content was 29.7, 18.4, and 17.6 wt% for ethanol, 1-propanol, and 1-butanol, respectively. As discussed below, the large weight of 29.7% for the ethanol case was caused by contamination of the eroded Cu electrode.

A three-electrode electrochemical cell with a rotating disk electrode (RDE) and a

potentiostat (SI1287, Solartron Analytical.) were used for cyclic voltammetry (CV) and high potential cycle testing at room temperature. To prepare the samples, 1.9 ml of 2-propanol and 0.6 ml of ultrapure water were mixed. Next, 2 mg of Pt-nanoparticle-coated nanographene was dispersed in this solution. Then, 10 μl of 10% Nafion DE1021 (Wako) diluted in water was added to this solution. The solution was stirred and homogenized for 30 min using a homogenizer. Subsequently, 22 $\mu\text{g-Pt}/\text{cm}^2$ of the homogenized solution was deposited onto a working electrode with an area of 0.07065 cm^2 . The coated working electrode was heated for 15 min at 65°C, and then immersed in 0.1 M HClO_4 solution. A reversible hydrogen electrode and Pt wire was used as the reference and counter electrodes, respectively. The solution was purged with the N_2 gas for 20 min. CV was conducted by varying the potential from 0.05 to 1.2 V at a scan rate of 50 mV/s. For the evaluation of durability, a high potential cycle test was performed up to 10,000 cycles in accordance with the standard protocol of the fuel cell commercialization conference of Japan (FCCJ). The potential was varied from 1.0 V to 1.5 V at a scan rate of 500 mV/s.

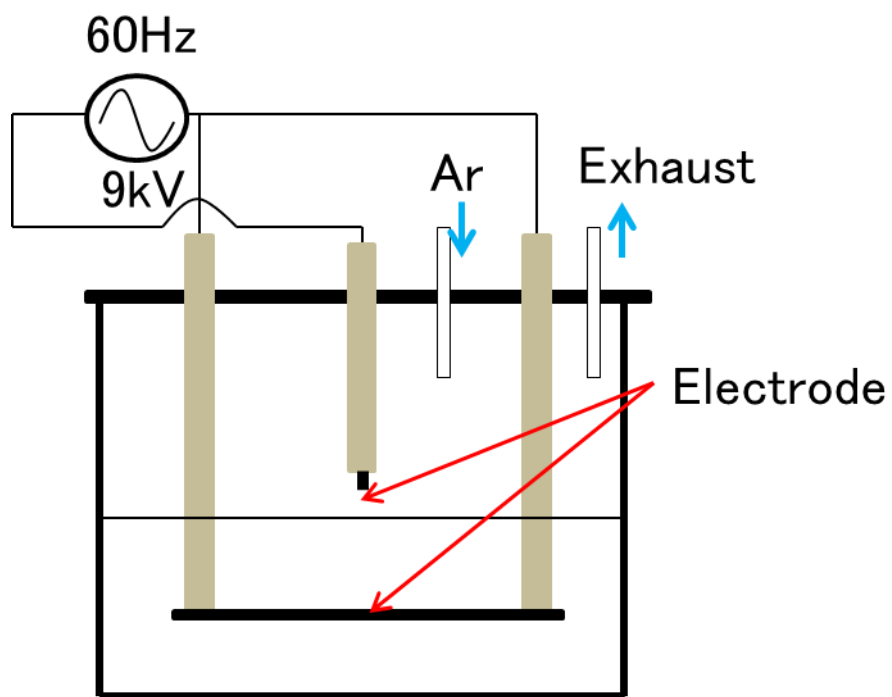


Fig. 3-1 Schematic of in-liquid plasma system.

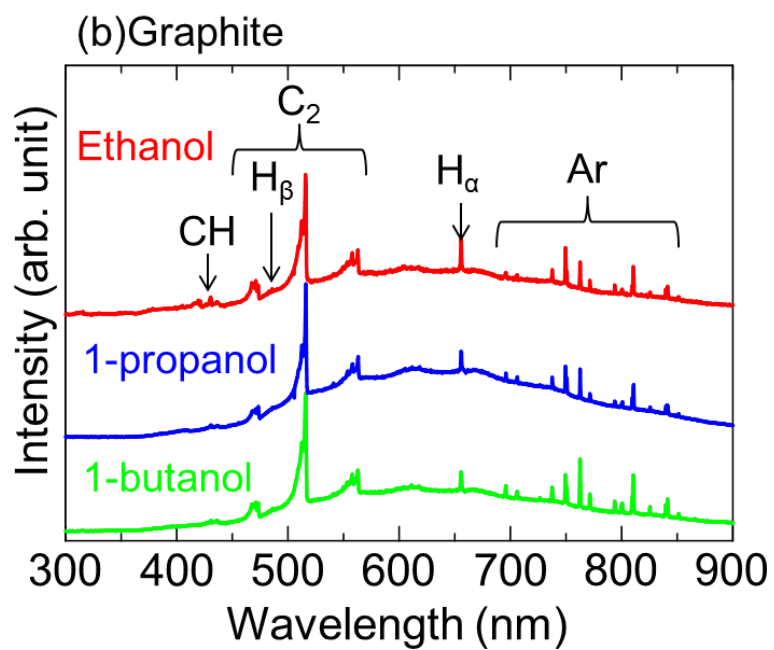
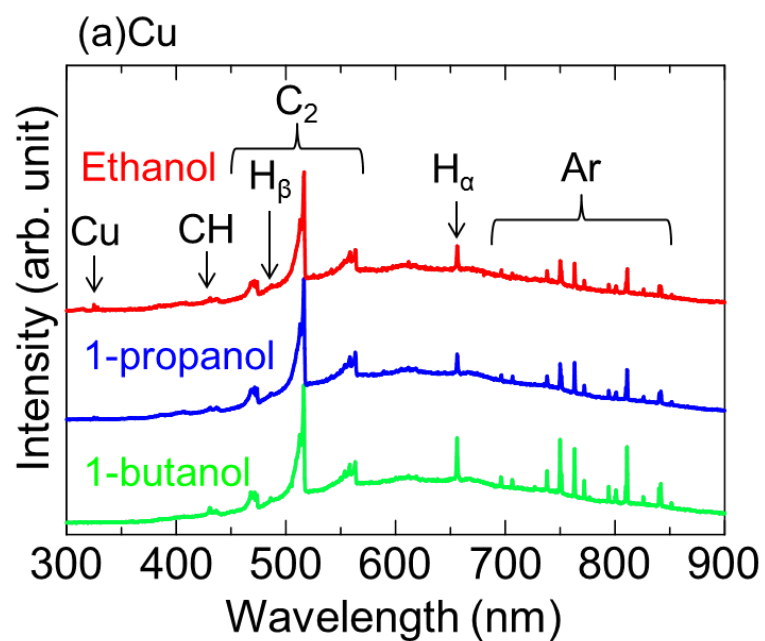
3.3 Synthesized and Characteristics

3.3.1 Plasma diagnostics

The in-liquid plasma was analyzed by optical emission spectroscopy. Figure 3-2 shows typical emission spectra of the plasma generated by a combination of the graphite electrode and ethanol. Figure 3-2(a-b) shows spectra in the 300-900 nm range. Around 500 nm, spectral peaks were clearly observed. These were attributed to the Swan band of the C_2 molecule ($d^3\Pi_g - a^3\Pi_u, v=0, 0$) with a band head around 516 nm. Spectral fitting was conducted [6]. The rotation temperature (T_{rot}) and vibrational temperature (T_{vib}) were estimated to be 2100 K and 2000 K, respectively. Presumably, the C_2 molecules were generated by the recombination of atomic C, which was preliminarily formed by the decomposition of alcohol. Thus, the T_{vib} and T_{rot} of the C_2 molecules might be thermalized by collisions of the background gases. This means that the ro-vibrational temperatures can be regarded as the gas temperatures. Table 3-1 shows rotation temperature and vibration temperature of all conditions. As the alcohol and electrode were varied, no significant change was observed in the ro-vibrational temperatures of the C_2 molecules, because the generated plasmas had similar characteristics. It was found that, in the gaseous Ar plasma, O and H atoms were generated by electron-collision-induced reactions. The fact that spectral peaks Cu were identified at wavelengths around 324.7 and 327.4 nm indicated that the Cu electrode was eroded by the plasma. H_β around 486.13 nm [7]. Using Voigtian fitting, Stark broadening widths were obtained and the electron densities were estimated [8]. Figure 3-3(a) shows the estimated electron densities for different types of alcohol and electrodes. The estimated electron densities in the Cu electrode were $3.0 \times 10^{14} \text{ cm}^{-3}$ for

Chapter 3

ethanol, $3.4 \times 10^{14} \text{ cm}^{-3}$ for 1-propanol, and $3.9 \times 10^{14} \text{ cm}^{-3}$ for 1-butanol. The estimated electron densities in the graphite electrode were $2.9 \times 10^{14} \text{ cm}^{-3}$ for ethanol, $3.9 \times 10^{14} \text{ cm}^{-3}$ for 1-propanol, and $5.0 \times 10^{14} \text{ cm}^{-3}$ for 1-butanol. The electron density increased with increasing molecular weight of alcohol. The electrical conductivity of the alcohol might be presumably a dominant factor: the higher the molecular weight of the alcohol, having vapor pressures: 8 kPa for Ethanol, 3 kPa for 1-propanol, and 1 kPa for 1-butanol at temperature of 300 K. The higher the electrical current flowing through it, and thus, the higher the electron density.



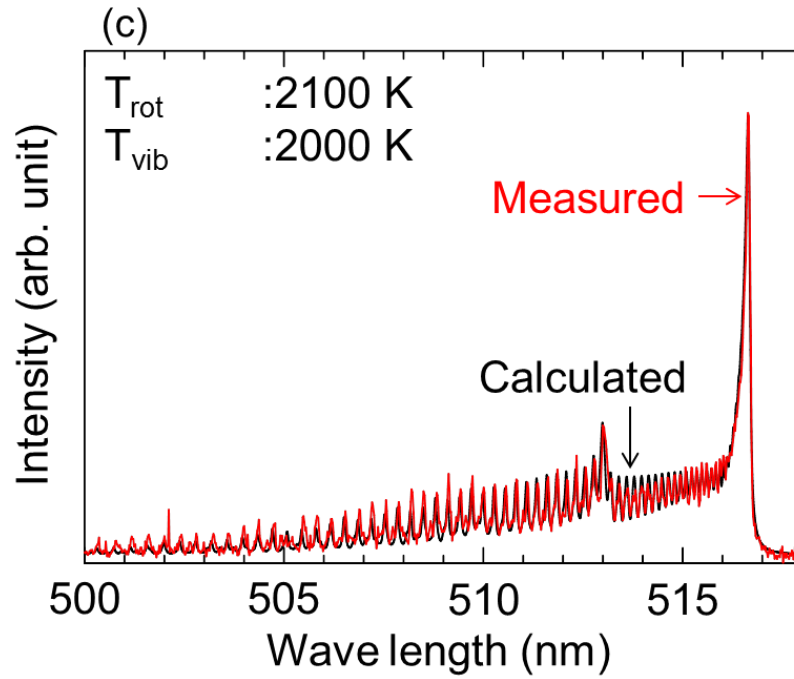


Fig. 3-2 Optical emission spectrum of in-liquid plasma. (a-b) Spectral range from 300 to 900 nm; (c) C_2 Swan band around 516 nm with graphite electrode by ethanol; The measured and calculated spectra are shown.

Table 3-1. Rotational temperature and vibration temperature by plasma condition.

Electrode	Alcohol	T_{rot} (K)	T_{vib} (K)
Cu	Ethanol	2300	2150
	1-propanol	2500	2200
	1-butanol	2550	2300
Graphite	Ethanol	2100	2000
	1-propanol	2300	2300
	1-butanol	2700	2450

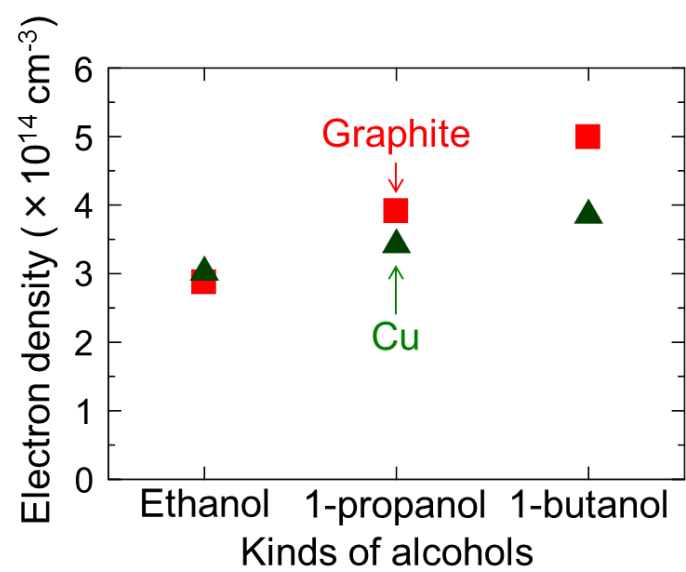


Fig. 3-3 Trends in the electron density of the in-liquid plasma, as measured by the H_{β} spectrum.

3.3.2 Synthesis rates

Figure 3-4 shows the amounts of nanographenes synthesized by the in-liquid plasma using the Cu or graphite electrode. The nanographene yields, obtained using the Cu electrode and a synthesizing duration of 1 h, were 13.5 mg for ethanol, 37.6 mg for 1-propanol, and 55.3 mg for 1-butanol. The nanographene yields, obtained using the graphite electrode for 1 h, were 18.2 mg for ethanol, 38.1 mg for 1-propanol, and 66.3 mg for 1-butanol. Larger amounts of nanographene were synthesized with higher-molecular-weight alcohols, as reported previously [1]. Larger synthesis yields corresponded to higher electron densities, as seen in the OES results. According to the gas chromatography results of the previous study, the residual liquid in the case of nanographene synthesis using ethanol contained reaction intermediaries, such as 2,3-butanediol ($\text{CH}_3\text{CH}(\text{OH})\text{CH}(\text{OH})\text{CH}_3$), phenylethyne ($\text{C}_6\text{H}_5\text{C}\equiv\text{CH}$), indene (C_9H_8), naphthalene (C_{10}H_8), and biphenylene (C_{12}H_8) [1]. These molecules suggested that the six-membered ring structures were formed through Diels-Alder-type reactions involving elimination and dehydration. The in-liquid plasma provided a huge variety of molecules containing oxygen atoms, C=C double bonds, C≡C triple bonds, and so forth. In addition, the crystallinity of nanographene might be governed by the ring formation reactions, eliminating the modified branch reactions. Thus, it is believed that different types of alcohol imparted different conversion efficiencies to the six-membered ring structures. Larger amounts of nanographene were formed from higher-molecular-weight alcohols in the case of both graphite and Cu electrodes. The nanographene yield was slightly larger for the graphite electrode.

The powder X-ray diffraction (XRD) profiles indicated that Cu was incorporated

into the synthesized materials when the Cu electrode was used with ethanol and 1-propanol. This indicated that the Cu electrodes were eroded during plasma discharge, as will be discussed later.

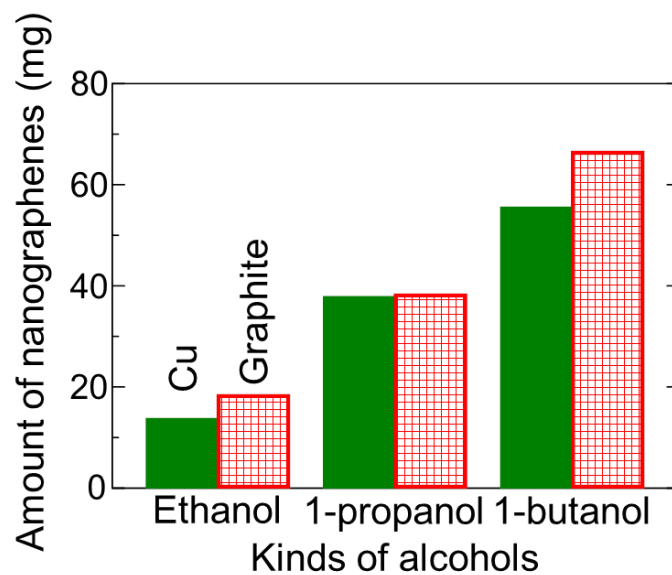


Fig. 3-4 Amounts of nanographene synthesized by in-liquid plasma using a Cu or graphite electrodes with ethanol, 1-propanol, or 1-butanol.

3.3.3 Degree of perfection of six-membered ring structure

Figure 3-5 shows the Raman spectra of nanographenes synthesized using (a) Cu and (b) graphite electrodes. Four peaks were clearly visible in all spectra, as is always the case in nanographene samples. G- and 2D-band peaks were observed at 1580 and 2700 cm^{-1} , respectively. These peaks are induced by six-membered ring structures [9-10]. The other two peaks at 1340 and 1620 cm^{-1} were attributed to the D- and D'-bands, respectively. These arise from the defects and edges of six-membered rings [9].

The FWHM value of the G-band peak indicates the degree of perfection of the six-membered ring structures: the smaller the G-band peak, the higher the degree of perfection. Figure 3-5(a) shows the FWHM values of the G-band peaks of the Raman spectra. In the case of the Cu electrode, the FWHM values of the G-band peaks are 36, 47, and 59 cm^{-1} for nanographenes synthesized from ethanol, 1-propanol, and 1-butanol, respectively, while the corresponding values for the graphite electrode are 32, 39, and 48 cm^{-1} . These results suggest that nanographenes that have highly perfect six-membered rings were synthesized using lower-molecular-weight alcohols. The FWHM values of the G-band peaks for samples synthesized by the graphite electrode were smaller. This means that six-membered ring structures with lower distortion were produced by the graphite electrode. The high crystallinity of the nanographene synthesized using ethanol was evident in the small FWHM values of the G-band peak, comparable to those of CVD-grown graphene and HOPG.

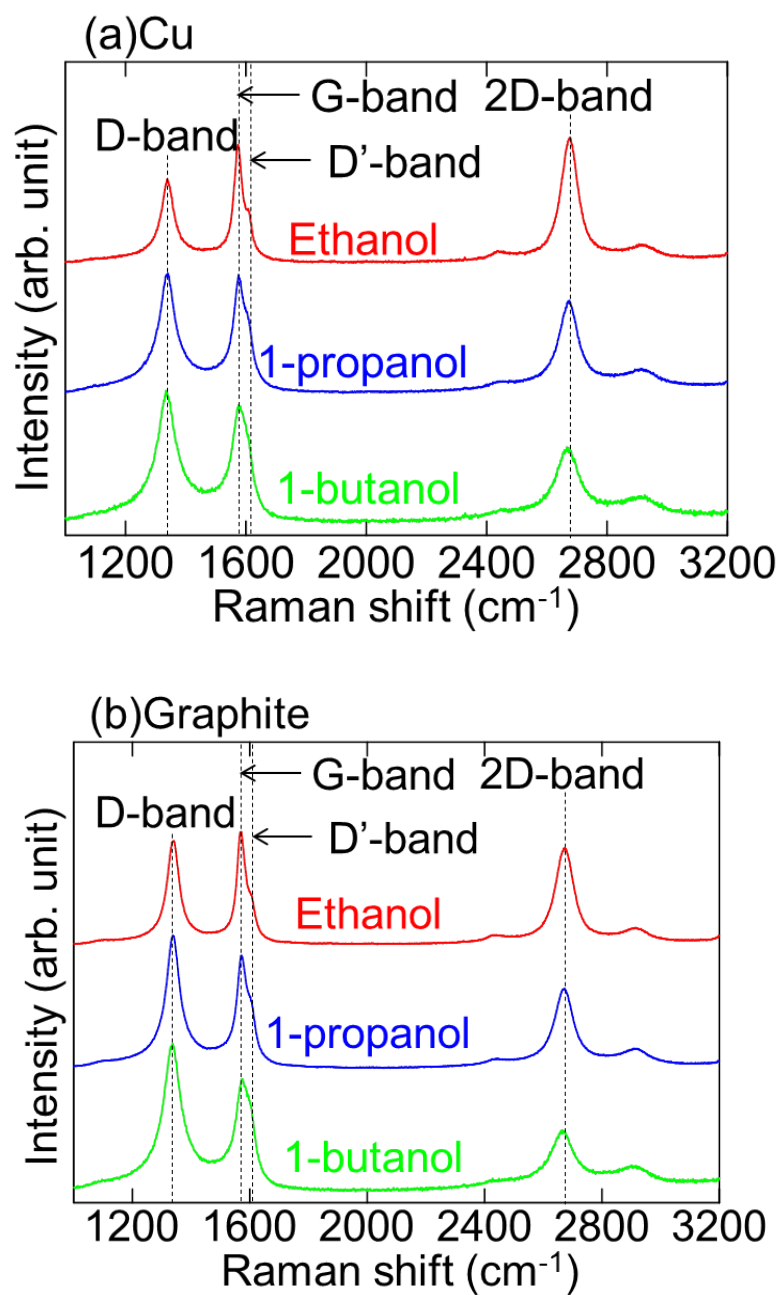


Fig. 3-5 Raman spectra of nanographenes synthesized by in-liquid plasma using a Cu or graphite electrode with ethanol, 1-propanol, or 1-butanol.

Figure 3-6(b) shows the crystallite sizes of the nanographenes estimated from the I_D/I_G ratios of the Raman spectra [11]. I_G and I_D denote the integral intensities of the G and D bands, respectively.

The I_D/I_G ratio of the Cu electrode was 1.2 for ethanol, 1.9 for 1-propanol, and 2.6 for 1-butanol. The electron density in the graphite electrode was 1.6 for ethanol, 2.1 for 1-propanol, and 2.5 for 1-butanol. For the Cu electrode, the crystallite sizes of nanographenes synthesized by ethanol, 1-propanol, and 1-butanol were 15.9, 10.1, and 7.5 nm, respectively, while the corresponding values for the graphite electrode were 11.9, 9.3, and 7.7 nm. The crystallite sizes were large when lower-molecular-weight alcohols and the Cu electrode were used. Smaller I_D/I_G ratios were obtained with the Cu electrode, which indicated that the crystallite size obtained by the Cu electrode was larger.

These above results revealed the tradeoff between the synthesis rate and the crystallinity, as indicated by the FWHM value of the G-band peak and the crystallite size.

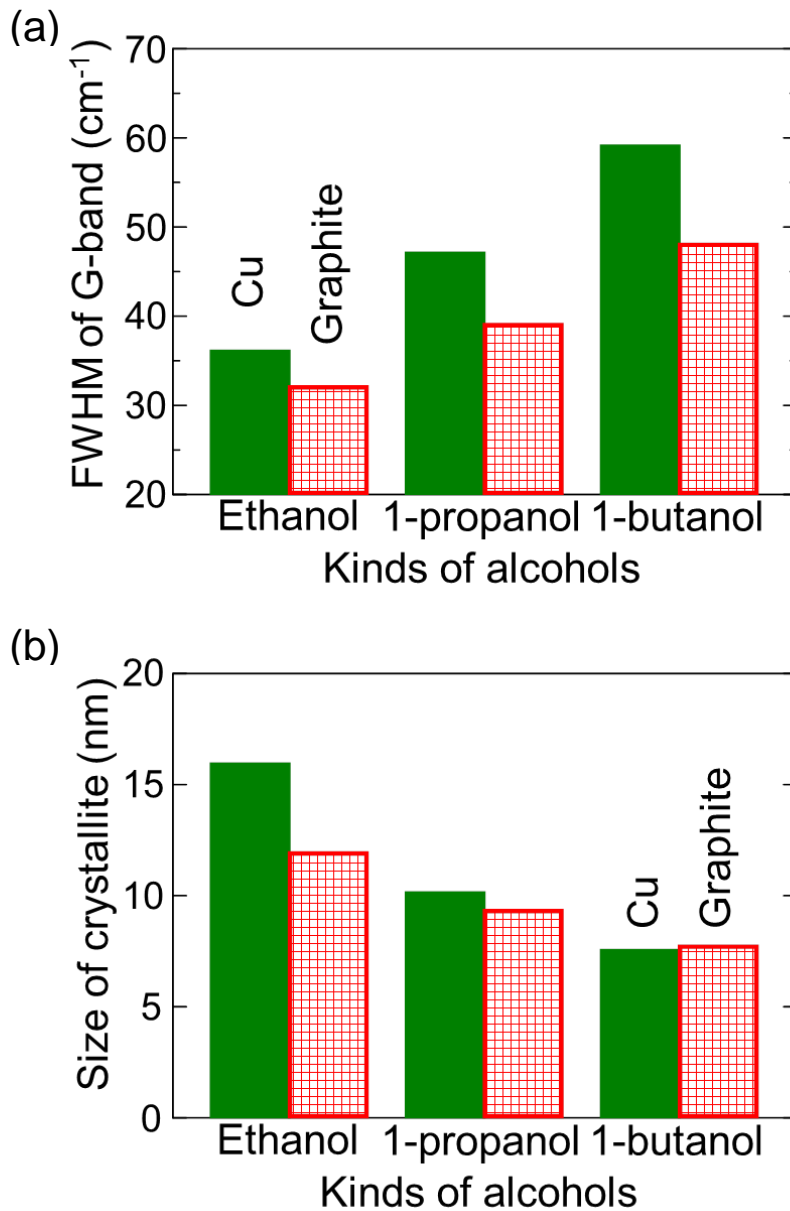


Fig. 3-6 (a) Full width at half maximum (FWHM) values of G-band peaks in the Raman spectra of nanographenes synthesized by an in-liquid plasma using a Cu or graphite electrode with ethanol, 1-propanol, or 1-butanol. (b) Crystallite size in nanographenes synthesized by the in-liquid plasma using a Cu or graphite electrode with ethanol, 1-propanol, or 1-butanol, as determined from the I_D/I_G ratios of the Raman spectra.

3.4 Crystalline structures of Pt nanoparticles supported on nanographenes

The Cu electrode was eroded. Cu emissions were observed in the OES in the gas phase, as described above. The crystalline growth of nanographene has been enhanced by the incorporation of Cu into the reaction sites of the nanographene [12]. Unfortunately, there was no clear evidence for the catalytic effect on the graphene growth reaction. However, the structural differences between the nanographenes synthesized in Cu and graphite may depend on the catalyzing effects of copper. On the other hand, in order to prepare a catalyst electrode for a fuel cell, fine Pt particles were loaded onto nanographene. During loading of the catalysts, the Pt nanoparticle formation was also influenced by the presence of Cu on the nanographenes.

Figure 3-7 shows the powder XRD profiles of the Pt-nanoparticle supported on nanographenes. In Fig. 3-6(a), the broad diffraction peaks were clearly found at 25.5°, 25.1°, and 25.0° for the cases using ethanol, 1-propanol and 1-butanol with the Cu electrode, respectively. These values were smaller than the reported value of graphite's 002 plane (26.5°). This means that the lattice spacing values of 002 planes formed in this experiment were larger than that of the graphite bulk (0.34 nm). The lattice spacing values of graphite's 002 planes were estimated to be 0.35, 0.35 and 0.36 nm for the cases using ethanol, 1-propanol and 1-butanol, respectively. From the widths of those peaks and by using the Scherrer equation, the crystalline sizes were estimated to be 2.0, 1.7, and 1.6 nm for ethanol, 1-propanol, and 1-butanol, respectively, with the Cu electrode. These results mean that the higher crystallinity nanographenes with larger

crystallite size was formed using the lower molecular-weight alcohol.

The domain sizes obtained the XRD and the Raman methods are different. The author thinks that the differences may cause due to the direction of nanographene domains, i.e., along sheet direction or across sheet-lamination direction. It can be seen that the value of domain size derived from the result of Raman spectroscopy is different. This is because the value obtained by Raman spectroscopy is the plane direction and the value derived from XRD is the thickness direction. From this result, it is considered that the nanographenes synthesized has about 5 to 6 layers of about 10 nm size. In contrast, the very weak and broad peaks were also found at 26.5° in the cases using the graphite electrodes as shown in Figure 3-6(b). Even in the Raman G-band peaks were observed without significant differences among the samples synthesized with the Cu or graphite electrodes, the diffraction peaks of graphite's 002 plane in the XRD results were possibly dependent on the Cu incorporation. Thus, the graphitic components may depend on the catalyzing effects of copper.

In all profiles, Pt111 and Pt200 diffraction peaks were also clearly observed at 39.7° and 46.3° , respectively. For the Cu electrode and ethanol or 1-propanol, small diffraction peaks related to Cu111 also appeared at 43.20° . In addition, for the Cu electrode with ethanol and 1-propanol, diffraction peaks appeared at 40.67° and 40.30° . From the widths of the Pt111 diffraction peaks and by using the Scherrer equation, the average diameters of the Pt nanoparticles were estimated to be 4.0, 3.9, and 4.5 nm for ethanol, 1-propanol, and 1-butanol, respectively, in the case of the Cu electrode [13]. The corresponding values for the graphite electrode were 3.2, 4.0, and 4.0 nm. Thus, the nanoparticle sizes synthesized using the Cu electrode were larger than those synthesized by the graphite electrode.

As revealed by the thermogravimetric analysis results presented above, the compound synthesized using the Cu electrode and ethanol contained metallic contaminants. The amount of metallic contaminants decreased in the order ethanol > 1-propanol > butanol. It is well known that diffraction peaks shift to higher angles in the case of PtCu compounds [14]. The peak could be identified as PtCu alloy, and using Vegard's law, the Cu content was estimated to be 26% with ethanol. Or, the Cu content was estimated to be 15% with 1-propanol. Both Pt and Pt₇₄Cu₂₆ or Pt₈₅Cu₁₅ nanoparticles were present on the nanographenes when Cu electrodes were used, especially with ethanol and 1-propanol. These results indicated that PtCu was formed. Cu atoms were deposited from the Cu electrode onto the nanographene. During Pt nanoparticle formation, the residual Cu might have reacted with Pt to form PtCu.

Figure 3-8 shows transmission electron microscopy (TEM) images and transmission electron diffraction (TED) patterns of Pt nanoparticles supported on the nanographenes synthesized using the (a-c) Cu and (d-f) Graphite electrodes with ethanol. The nanoparticles were with average diameters of 4.4 nm for Cu electrode and 3.4 nm for graphite electrode with ethanol. In the TED patterns, rings can be assigned to diffraction spots for Pt111, Pt002, Pt220, and so forth. For PtCu particles, as shown from the XRD analyses, no discriminable peak was observed in all TED patterns. PtCu111 diffraction is positioned at very close to Pt111, since the lattice spacing of 0.220 nm and the Cu content of 24 %. In accordance with all TEM images and TED patterns, regardless of the types of alcohols, Pt and PtCu nanoparticles with averaged sizes of 4.5 nm for Cu and 3.4 nm for graphite electrodes were supported on the nanographenes.

Figure 3-9 shows the mechanism by which PtCu particles are formed. When

synthesized using ethanol and 1-propanol, Cu as an electrode material is mixed during synthesis. Then, the Pt nanoparticles are supported by the liquid phase reduction method. At that time, Pt nanoparticles are formed when Pt nanoparticles are formed on the nanographene. It is considered that PtCu alloy particles were formed in the vicinity where Cu exists. The size of Cu particles estimated from the XRD pattern is present at 8.4 nm in the case of ethanol. In the case of 1-propanol, it is 12.8 nm. PtCu alloy particles were 5.3 nm in the case of ethanol. In addition, it was 5.3 nm in the case of 1-propanol. From this, it is thought that Cu present as small particles forms PtCu alloy particles and it is difficult to form an alloy with larger particles. It is thought that the amount containing Cu is related to the synthesis amount of nanographene. Since the state of the plasma has not changed significantly, the influence of the plasma on the Cu electrode is almost the same. However, the synthesis amount varies nearly doubling in both cases. From this fact, it was considered that the mixing ratio of the metal mixed from the electrode material became small in the sample with large amount of nanographene synthesis. As a result, it seems that the ratio of PtCu alloy nanoparticles produced by alcohol species has changed. On the other hand, in the case of 1-butanol, mixing of Cu could not be confirmed. This is probably due to the large amount of synthesis of nanographene. Even if Cu was mixed, it was an extremely small amount, so it seems that there was no influence in the process of producing Pt nanoparticles.

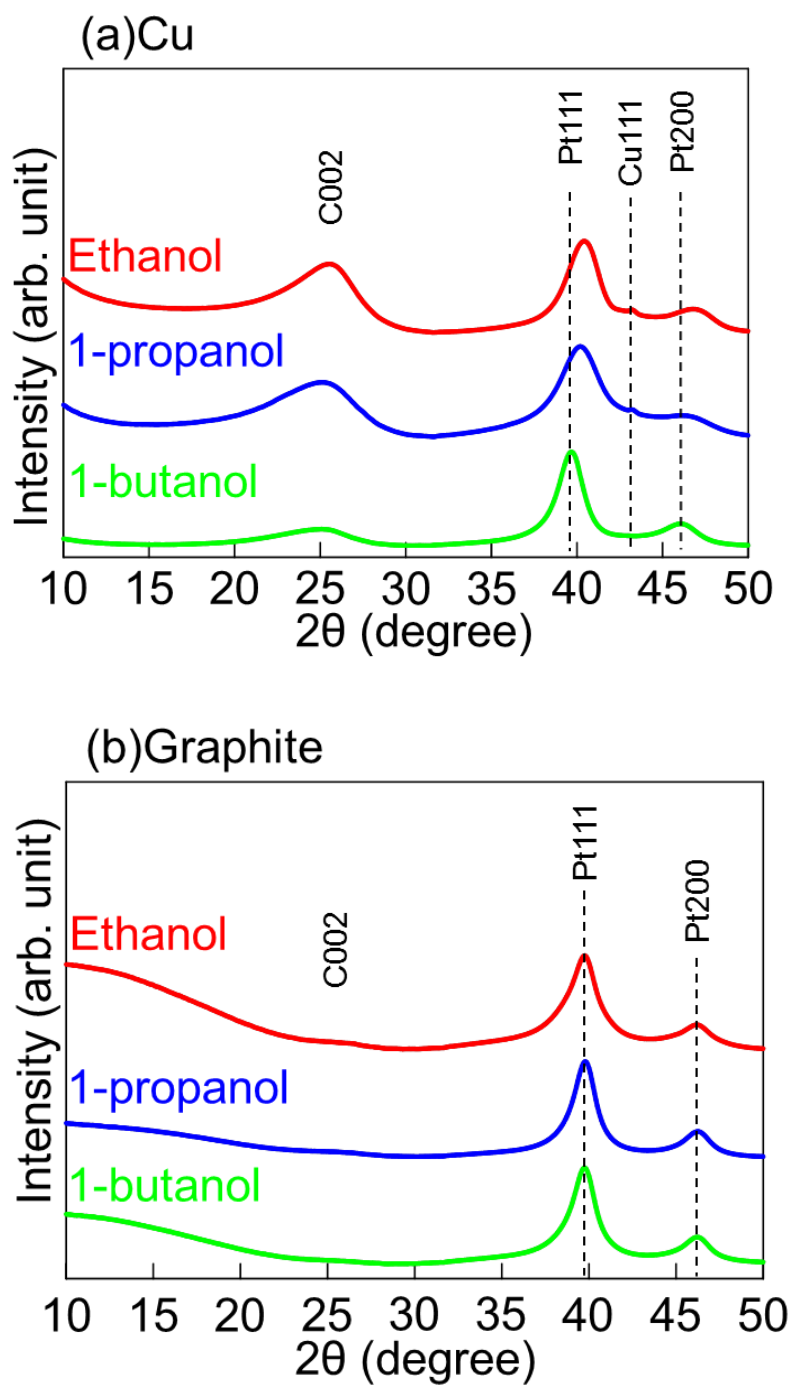
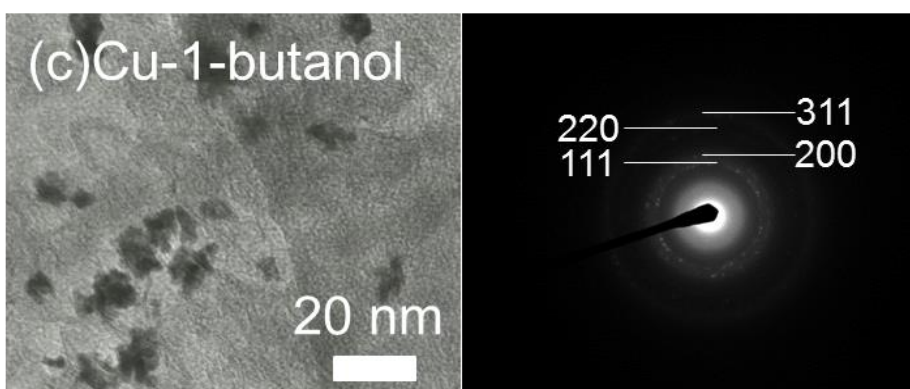
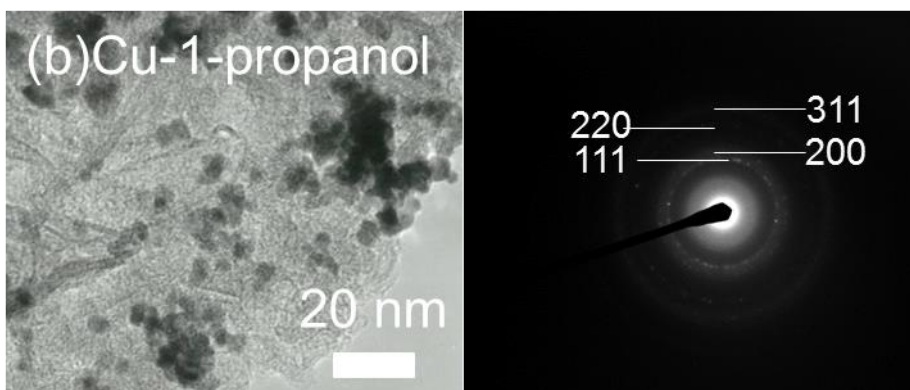
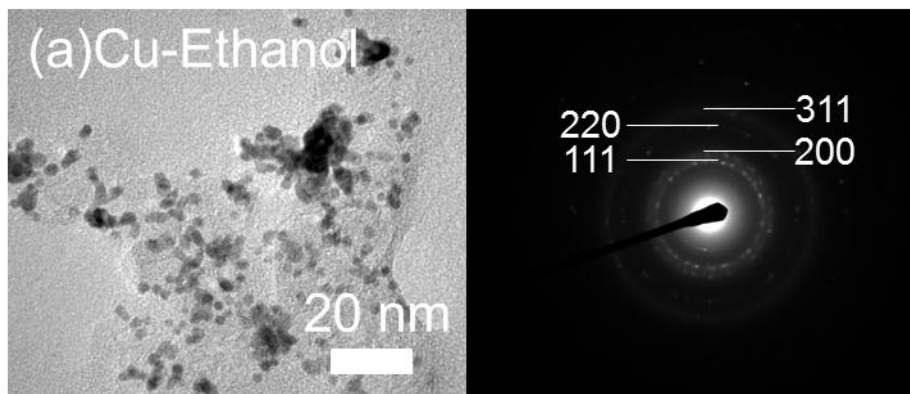


Fig. 3-7 X-ray diffraction (XRD) profiles of Pt-nanoparticle-coated nanographenes synthesized by a in-liquid plasma using a Cu or graphite electrode with ethanol, 1-propanol, or 1-butanol.



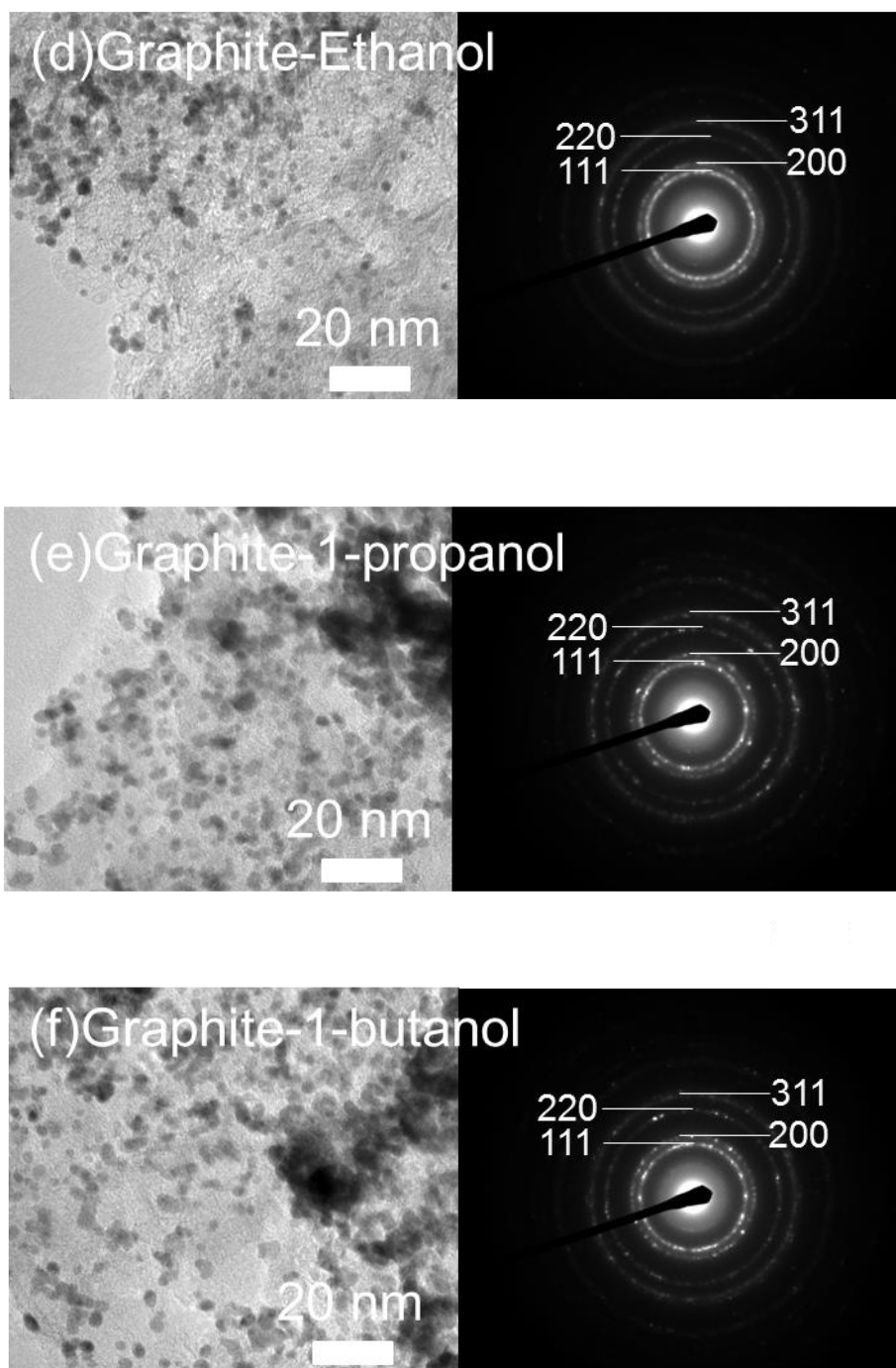


Fig. 3-8 Transmission electron microscopy (TEM) images and transmission electron diffraction (TED) patterns of Pt nanoparticles supported on nanographenes synthesized using (a~c) Cu or (d~f) graphite electrode with alcohol.

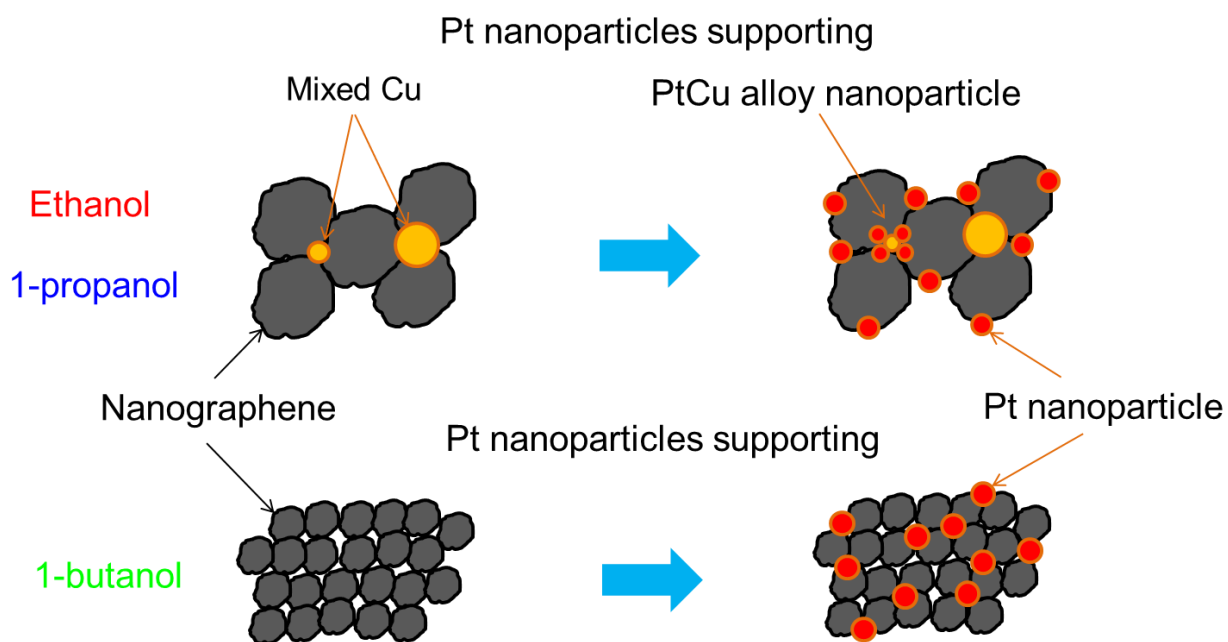


Fig. 3-9 Formation model of PtCu alloy nanoparticle.

3.5 Durability of catalyst of the Pt nanoparticles supported nanographenes

Figure 3-10 shows cyclic voltammograms obtained using Pt-nanoparticle-loaded nanographenes as a working electrode, before and after high potential cycle testing for 10,000 cycles. All curves exhibit typical peaks around 0.05 to 0.4 V vs. RHE (reversible hydrogen electrode), corresponding to hydrogen adsorption (Q_{H^a}) in positive current and desorption (Q_{H^d}) in negative current around 0.05 V; Pt oxidation (Q_{Pt^o}) in positive current and reduction (Q_{Pt^r}) in negative current around 0.8 V vs. RHE. The effective electrochemical surface areas (ECSAs) of Pt nanoparticles were derived from area intensities of Q_{H^a} using the hydrogen adsorption charge amount per unit area of Pt. The ECSAs of Pt on nanographene can be estimated by using the amounts of Pt nanoparticles measured by the thermogravimetric analyzer. Before the durability tests, the ECSAs were 42.9, 36.9, and 36.3 m²/g for the cases using the Cu electrode with ethanol, 1-propanol, and 1-butanol, respectively. The corresponding ESCAs for the graphite electrode were 59.0, 47.1, and 45.8 m²/g. The surface-area-to-volume ratios of the particles are inversely proportional to the diameters of Pt nanoparticles [15]. The nanographene synthesized using the Cu electrode was estimated to be 1.3 times larger than that synthesized using the graphite electrode. The ECSAs obtained by the graphite electrode were 1.1 to 1.2 times larger than those obtained by the Cu electrode. This may be due to the difference in surface-to-volume ratio between different diameters. For both the Cu and graphite electrodes, larger ECSAs were obtained by using lower-molecular-weight alcohols, even though the Pt nanoparticle sizes were

comparable. The ECSA values were determined by another factor, such as the electrical conductivity of the nanographenes. Since nanographenes synthesized using lower-molecular-weight alcohols had a higher crystallinity and larger crystallite size, their conductivities were higher and the carriers generated could be transported to the external circuit more smoothly.

Figure 3-11 shows the normalized ECSA values obtained during high potential cycle testing as a function of number of potential cycles. The ECSA values are normalized by the maximum values around 1,000 cycles. Even after 10,000 high potential cycles, the ECSAs decreased by only 10% from their maxima at 1000 cycles in the case of the Cu electrode and ethanol. In the case of the Cu electrode, the ECSAs decreased 16% and 33% for 1-propanol and 1-butanol, respectively. Lower-molecular-weight alcohols resulted in higher durability, because of the higher crystallinity of the synthesized nanographenes. By contrast, with the graphite electrode, the ECSA characteristics hardly deteriorated; the levels of deterioration with respect to the ECSA maxima were 12%, 10%, and 12% for ethanol, 1-propanol, and 1-butanol, respectively. Thus, high-crystallinity nanographenes were highly durable.

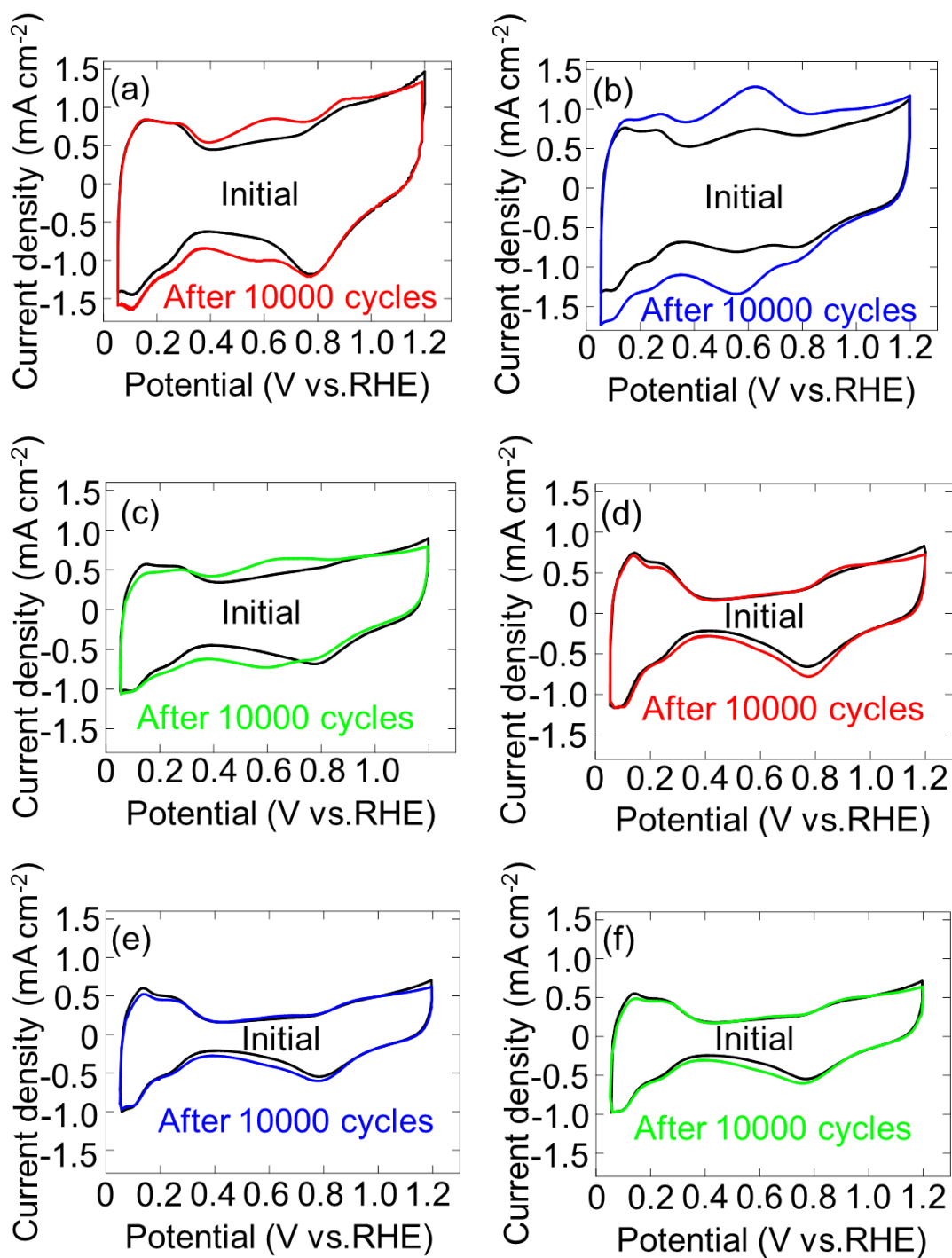


Fig. 3-10 Cyclic voltammograms using Pt-nanoparticle-supported nanographenes as working electrodes before and after high potential cycle testing for 10,000 cycles. The Cu (a-c) and graphite (d-f) electrodes were used with ethanol (a,d), 1-propanol (b,e), and 1-butanol (c,f).

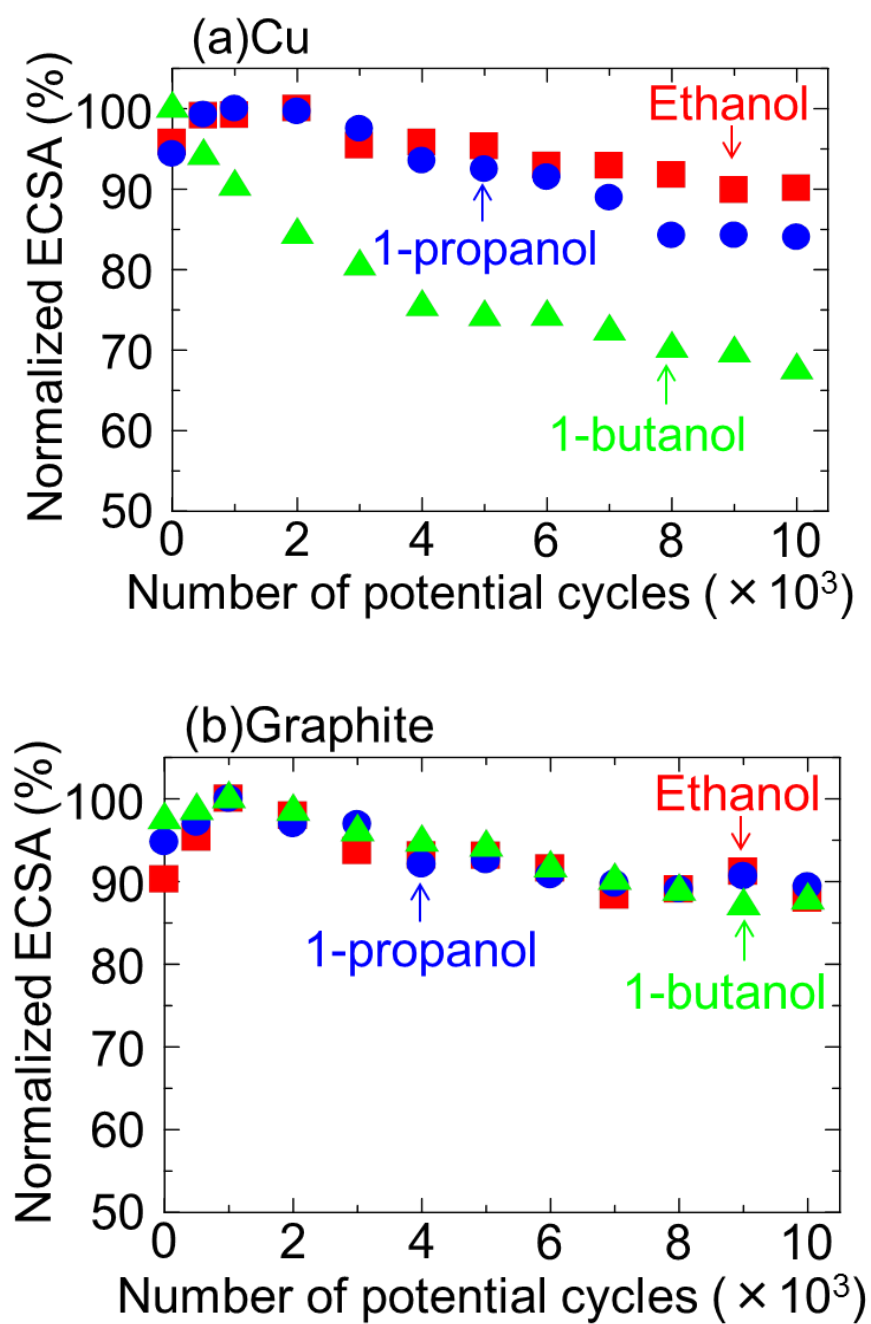


Fig. 3-11 Normalized ECSA values as a function of the number of potential cycles during high potential cycle testing.

Figure 3-12 shows the relationship between the deterioration rates and the FWHM values of the G-band peaks in the Raman spectra. As mentioned above, the FWHM values of G-band peaks correlates with the crystallite size of graphite. The deterioration rate increased when the FWHM values exceeded 48 cm^{-1} . The deterioration rate hardly changed, regardless of the change in crystallite size, in nanographenes synthesized using the graphite electrode. From this result, the model is shown in Figure 3-13. The deterioration rate increased with decreasing the Raman-detected crystallite size in the case of the Cu electrode. Therefore, the degree of structural disorders of the six-membered ring structure, rather than the crystallite size, affects the durability of Pt catalytic activity during high potential cycle testing. Since this kind of deterioration can presumably be promoted more easily at surface defects on nanographenes, low disordered nanographenes show a higher durability. Thus, the durability of nanographene as a catalyst support is improved significantly by the formation with low structural disorders of six-membered ring structures in the nanographene.

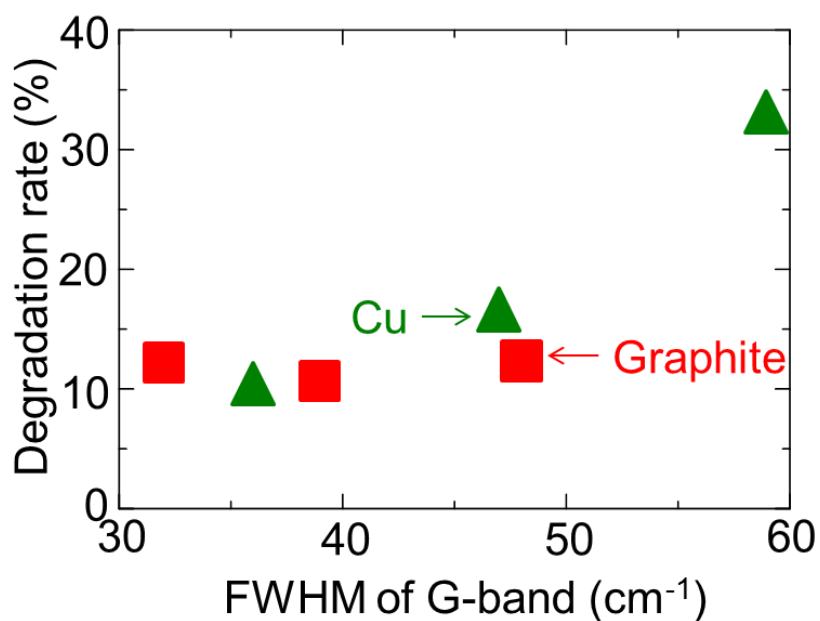


Fig. 3-12 Relationship between degradation rate of ECSAs and FWHM values of G-band peaks in Raman spectra using a Cu (●) or graphite (Δ) electrode.

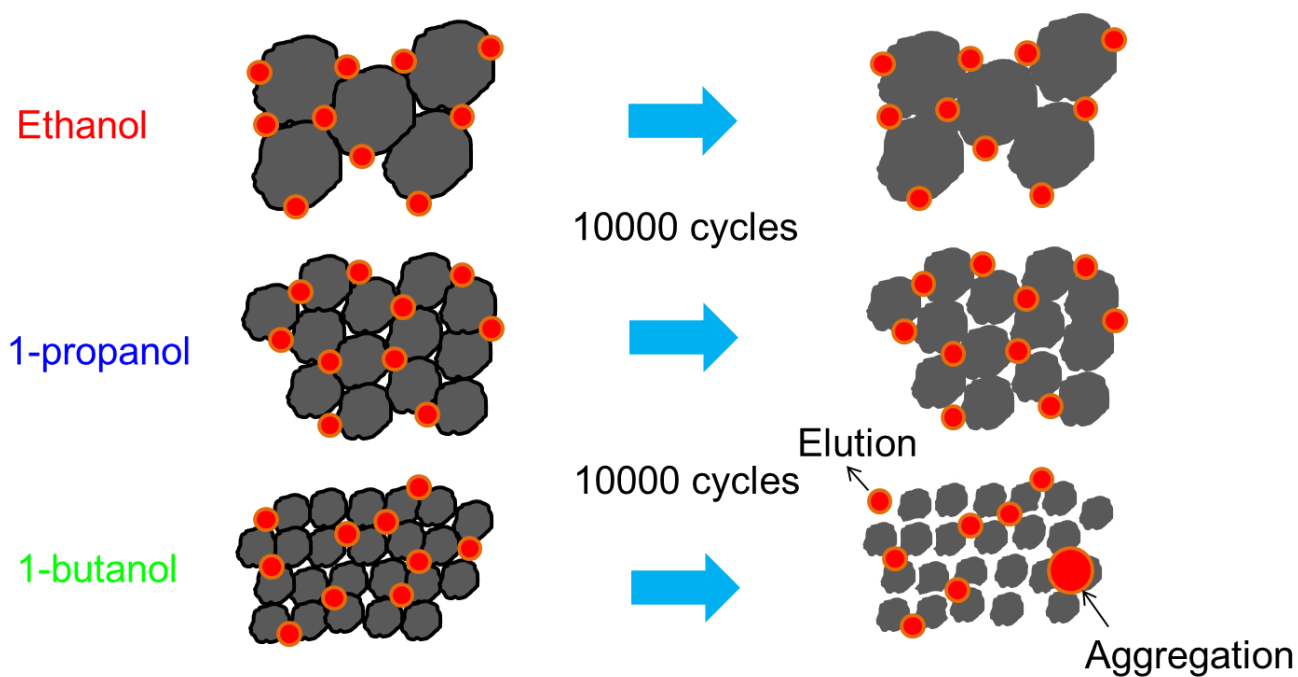


Fig. 3-13 Degradation model of nanographenes in high potential cycle testing.

3.6 Summary

Nanographenes with different crystallinities were synthesized by the in-liquid plasma, using one of three types of alcohol and a Cu or graphite electrode. The OES data indicate that the electron density ranged between 3.0×10^{14} and 5.0×10^{14} cm^{-3} . The electron density increased with increasing molecular weight of the alcohol, and was larger for the graphite electrode than for the Cu electrode. Regardless of the electrode type, a larger amount of nanographene was synthesized by using higher-molecular-weight alcohols. In the case of 1-butanol, 55.3 mg of nanographenes were synthesized using the Cu electrode for 1 h, while the 13.5 mg of nanographenes were synthesized by ethanol. Upon the use of lower-molecular-weight alcohols, the G-band peak in the Raman spectra became narrower and the relative intensity of the D-band peak decreased, indicating that the crystallinity of the nanographenes increased. The tradeoff between the synthesis rate and crystallinity depended on the type of alcohol. As seen in the cyclic voltammograms, the Pt electrochemical surface areas obtained using the nanographenes were attributed to not only the smaller size of the Pt nanoparticles but also the higher electrical conductivity due to higher crystallinity. Author found that higher nanographene crystallinity correlated with lower degradation rate during high potential cycle testing. For nanographene synthesized by ethanol, the ECSA degradation rate was only 10%, even after 10,000 cycles. The degree of perfection of the six-membered ring structure, rather than the crystallite size, was critical to improving the durability of nanographene during high potential cycle testing. The knowledge gained in this study will pave the way to the fabrication of highly durable catalyst supports through the use of nanographene synthesized by the in-liquid

plasmas.

References

- [1] T. Hagino, H. Kondo, K. Ishikawa, H. Kano, M. Sekine, and M. Hori, *Appl. Phys. Express* **5** (2012) 035101.
- [2] A. Ohma, K. Shinohara, A. Iiyama, T. Yoshida, and A. Daimaru, *ECS Trans.* **41** (2011) 775.
- [3] Y. Feng, G. Zhou, G. Wang, M. Qu, and Z. Yu, *Chem. Phys. Lett.* **375** (2003) 645.
- [4] T. C. Deivaraj, and J. Y. Lee, *J. Power Sources* **142** (2005) 43.
- [5] W. Z. Li, C. H. Liang, W. J. Zhou, J. S. Qiu, Z. H. Zhou, G. Q. Sun, and Q. Xin, *J. Phys. Chem. B* **107** (2003) 6292.
- [6] X. Chen, J. Mazumder, and A. Purohit, *Appl. Phys. A* **52** (1991) 328.
- [7] H. R. Griem, *Plasma Spectroscopy* (McGraw-Hill, New York, 1964).
- [8] S. Takashima, M. Hori, T. Goto, A. Kono, M. Ito, and K. Yoneda, *Appl. Phys. Lett.* **75** (1999) 3929.
- [9] F. Tuinstra, and J. L. Koenig, *J. Phys. Chem.* **53** (1970) 1126.
- [10] R. P. Vidano, D. B. Fishbach, L. J. Willis, and T. M. Loehr, *Solid State Commun.* **39** (1981) 341.
- [11] M. A. Pimenta, G. Dresselhaus, M. S. Dresselhaus, L. G. Cancado, A. Jorio, and R. Saito, *Phys. Chem. Chem. Phys.* **9** (2007) 1276.
- [12] S. Bhaviripudi, X. Jia, M. S. Dresselhaus, and J. Kong, *Nano Lett.* **10** (2010) 4128.
- [13] M. Oezaslan, F. Hasche, and P. Strasser, *J. Electrochem. Soc.* **159** (2012) 444.
- [14] V. Radmilovic, H. A. Gasteiger, and P. N. Ross, *J. Catal.* **154** (1995) 98.
- [15] M. Shao, A. Peles, and K. Shoemaker, *Nano Lett.* **11** (2011) 3714.

Chapter 4

Synthesis of graphene flakes by in-liquid plasma using iron phthalocyanine added alcohols

4.1 Introduction

Graphene fabrication methods are known; (i) The ultrasonication strips mechanically graphene-sheets by peeling off lumps of graphite-flakes,[1-3] however, the poor productivity is inferior in use for mass production;[4] (ii) The Hummer's method separates chemically by oxidation and reduction of graphite-flakes.[5-6] This method can synthesize a powder of graphene-flakes rapidly, showing poor crystallinity.[7] (iii) The atmospheric pressure plasma processes.[8,9]

There were reports of the graphene-flake synthesis in atmospheric pressure processes such as the submerged discharges in liquids.[8] Carbon nanomaterials were synthesized in the submerged plasma in the water added small amount of organics such as alcohols, hydrocarbons.[9] Nanometer-scaled flakes of graphene sheets were synthesized and called as carbon-onion, carbon nanoflower and carbon nanoflakes.[10-11] To the best our knowledge, micron-size graphene flakes have not

been successfully synthesized by a bottom-up method employing a liquid source in liquid processes. Noticeably, there was no report about synthesis of graphene-flakes with a micron size in the liquid processing of electrically discharged plasma-generations. Therefore, this study aimed to search feasibility of a bottom-up approach of large-size graphene synthesis in the liquid plasma processing.

The realization of the synthesis of graphene-flakes with micrometer-scale in the in-liquid plasma of ethanol added with 15 mg of iron phthalocyanine (FePc; $C_{32}H_{16}FeN_8$) as an additive by dissolution in solvents such as dimethylformamide (DMF; $(CH_3)_2NCHO$) was reported. To know a mechanism of the synthesis, comparison among kinds of alcohols and solvents, the FePc addition into ethanol other than other alcohols was made. As the result, the effects related with FePc and ethanol are essential for the nanographene-flakes synthesis. Therefore, iron of FePc acts possibly as a catalyst of synthesis of graphene sheets, as similarly in syntheses of the carbon nanomaterials.[12-13]

4.2 Experimental details

A schematic illustration of the experimental procedure is shown in Figure 4-1(a). A glass reactor was an inner diameter of 108 mm. Iron phthalocyanine ($\text{FePc}(\text{C}_{32}\text{H}_{16}\text{FeN}_8)$; Tokyo Chemicals Industry Co., Ltd.) dispersed in (N,N-dimethylformamide($\text{C}_3\text{H}_7\text{NO}$); DMF, Wako Pure Chemical Industries, Ltd) for 30 min using a homogenizer (TOMY SEIKO UR-21P). Then 40 ml of the FePc-DMF solution mixed with 160 ml of pure ethanol ($\text{C}_2\text{H}_5\text{OH}$; Wako Pure Chemical Industries, Ltd.) and dispersed for 10 min. A total 200 ml of liquid filled in the reactor. Ar gas with a flow rate of 6 slm flowed in the reactor and kept at atmospheric pressure. Two electrodes were positioned at the upper half of gas-phase and the lower half of liquid-phase, sandwiched the gas-liquid boundary. Thus, the upper electrode was placed in the gas phase and the lower electrode was submerged in the liquid phase. The tip of the upper electrode made of graphite wire with a diameter of 3 mm was placed at 1 mm above the liquid level. The 100-mm-long wire that was used as the lower electrode was immersed at 9 mm below the liquid level in the alcohol. An alternative current (AC; 60 Hz) voltage of 9 kVpk power was applied between the two electrodes. Figure 4-1(b) shows a photograph of the in-liquid plasma discharge. After ignition of the discharge, the solution color turned immediately to dark. The synthesis duration was typically for 5 min. The dark-colored solutions were filtrated for collection of solid materials as the synthesized compounds by the suction filtration with a filter membrane of pore size approximately 1 μm (Millipore JAWP04700). The filtrates were weighed by the electronic balance. Also the collected carbon residues were microscopically observed by the scanning electron microscope (SEM; Hitachi-high technologies S-4800) and

analyzed by the Raman scattering spectroscopy (Renishaw inVia Reflex) using the 532 nm excitation of a Nd:YAG laser.

Optical emission spectra (OES) from the plasma were measured in the gas-phase region close to 3 mm above the liquid surface. The emissions were collected with a focusing lens (Nikon Rayfact PF 10545 MF-UV) and guided with an optical fiber to the spectrometer (ANDOR Shamrock 500i), which was equipped with an image intensifier charge-coupled device iCCD camera (ANDOR iStar) using a grating of 2400 lines/mm.

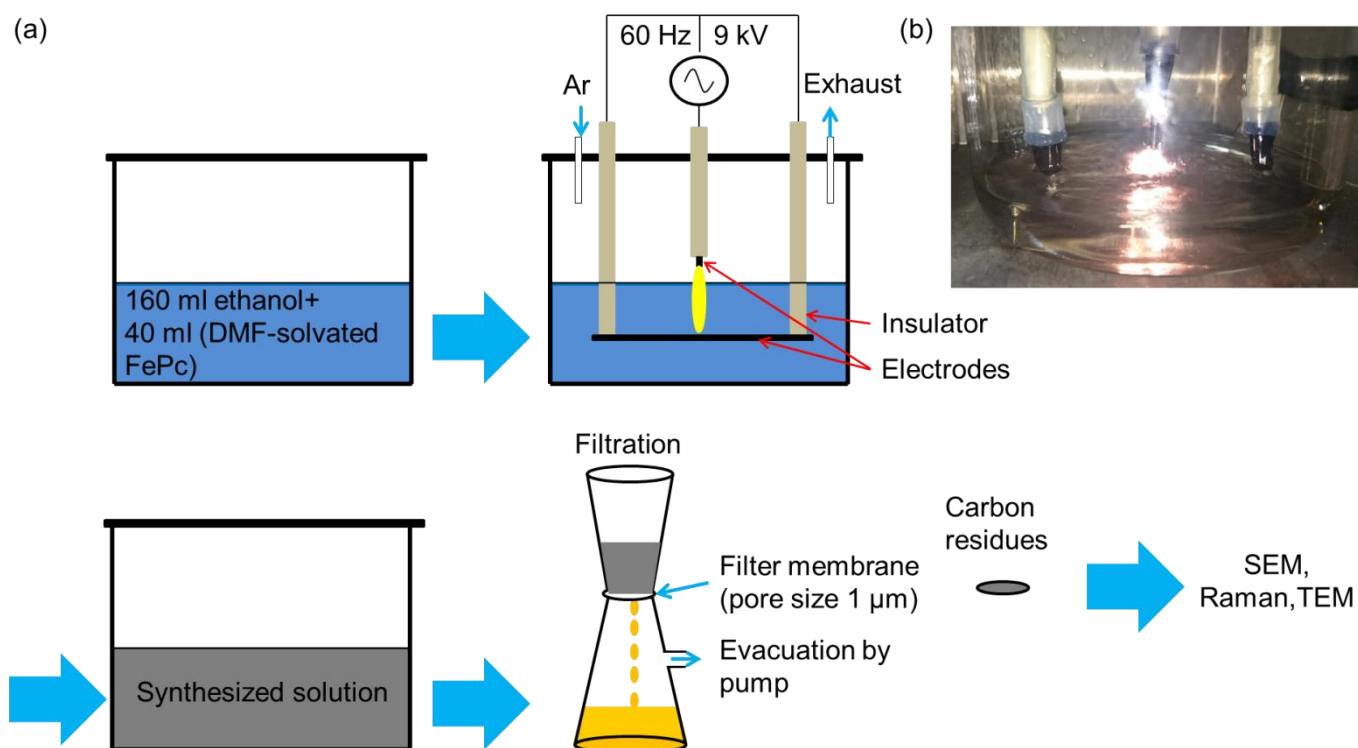


Fig. 4-1 (a) Schematic of experimental procedure of the in-liquid plasma technique. (b) Image of the in-liquid plasma.

4.3 Nanographene synthesized by in-liquid plasma

4.3.1 Surface analysis of graphene flakes

Carbon residues synthesized by employing the in-liquid plasma of ethanol added with FePc solvated in DMF were collected by the filter membrane. A photograph of the filtrates is shown in Figure 4-2(a). The black lumps are visible on the filter membrane. The SEM images are also shown in Figure 4-2(b-d). The flaky micron-size sheets are visible. In details, averaged size of the flakes was measured approximately 1 μm in length and less than 10 nm in thickness. It is noteworthy that the giant-sized flakes were the first report of the in-liquid process.

Next, the synthesized carbon residues were evaluated by the Raman spectroscopic measurements for clarification of nanographene features, as shown in Figure 4-3. The full width at half maximum (FWHM) of the G-band peaks were 30 cm^{-1} for the ethanol added with FePc solvated in DMF. Smaller FWHM value of the G-band peak indicates a degree of perfection of six-membered ring structures, since the 2D band around 2700 cm^{-1} was also visible. The D band originated from edges of nanographene was weak. The high-degree of perfection of six-membered ring nanographenes was obtained in the case of ethanol added with DMF-solvated FePc.

Figure 4-4(a) is a transmission electron microscopy (TEM) image of the nanographene materials synthesized by the in-liquid plasma of ethanol with DMF-solvated FePc. More than 100 nm sized sheet of graphene flake was observed at the upper half of the image, while aggregates of smaller structures were also found at the lower half. Figure 4-4(b) shows a TED pattern from the same image filed with the Fig. 4(a). Three rings were clearly observed and their lattice spacing values were

calculated to be 0.34 nm, 0.21 nm and 0.11 nm, respectively. These values are almost similar with the reported values of 0.34 nm, 0.20 nm and 0.12 nm for graphite (002), (101) and (112) planes, respectively.

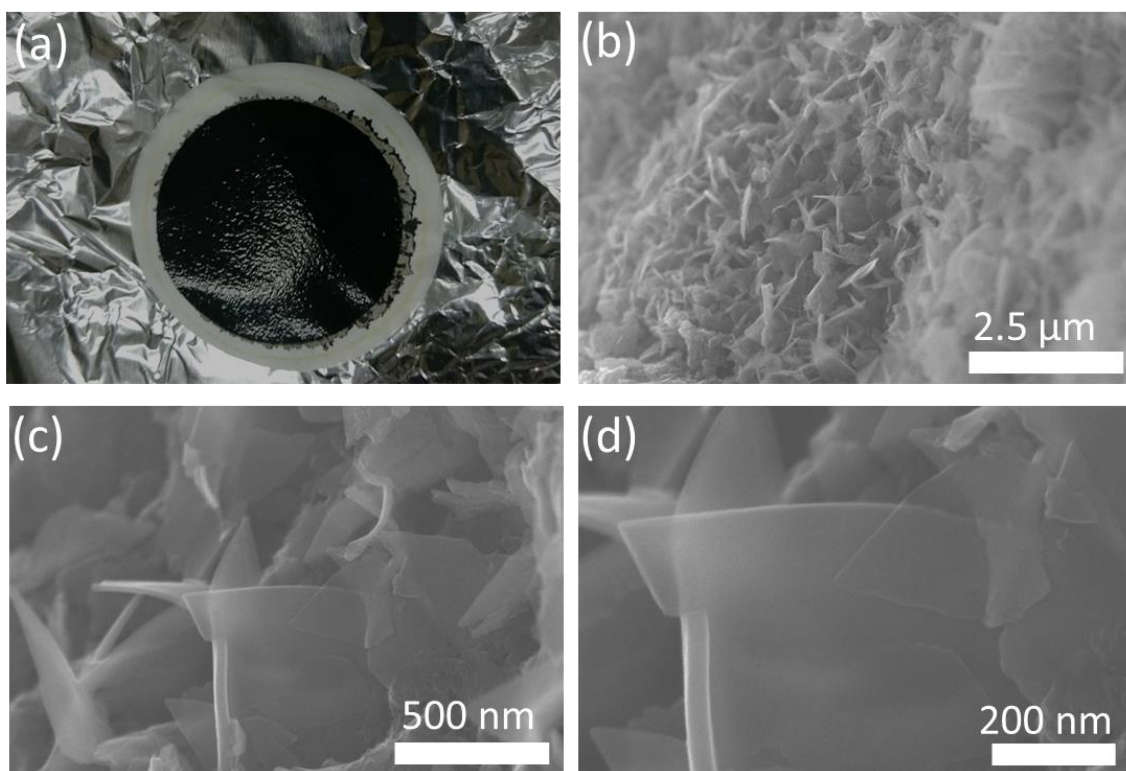


Fig. 4-2 (a) Image of carbon residue filtrates synthesized in ethanol with DMF-solvated FePc. (b-d) SEM images: (b) 2.5 μm scale, (c) 500 nm scale, and (d) 200 nm scale.

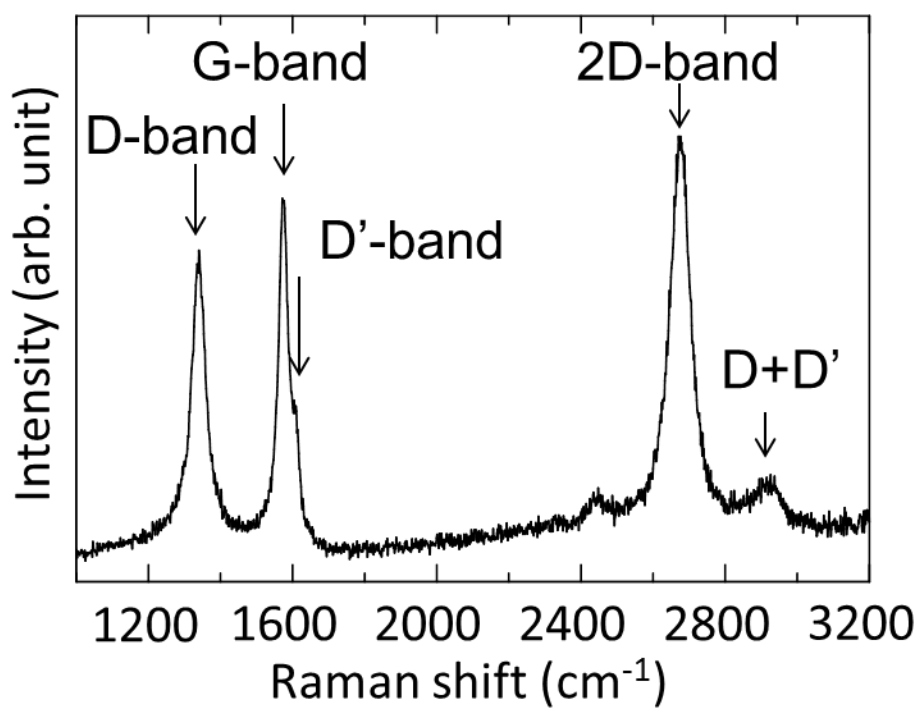


Fig. 4-3 Raman spectra of nanographenes synthesized by the in-liquid plasma in ethanol with DMF-solvated FePc.

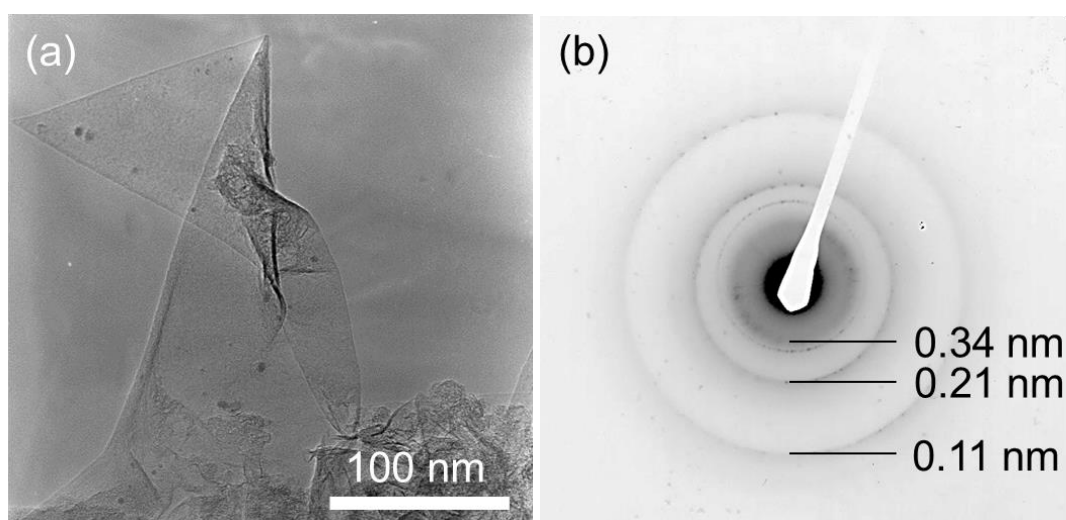


Fig. 4-4 (a)TEM image and (b)TED pattern of the in-liquid plasma approach in ethanol with DMF-solvated FePc.

4.3.2 Plasma diagnostics

The optical emissions were taken with a range between 200 and 900 nm, as shown in Figure 4-5. For the plasmas of the mixture of DMF-solvated FePc and ethanol, emissions of Fe or C (ca. 250 nm), OH (ca. 310 nm), CN (ca. 390 nm), CH (ca. 430 nm), H (488 and 656 nm), and C₂ (474, 516, and 564 nm) were observed. The Fe and CN emissions were arisen from FePc and DMF, respectively. Table 4-1 lists the electron density derived from the Stark broadening of H_β and the rotational temperature of C₂ estimated from fitting of measured spectra to simulated spectra in the Swan bands.[14-16] Since all spectroscopic parameters were no significant change, the plasma discharges briefly were not essential for the observed nanographene synthesis.

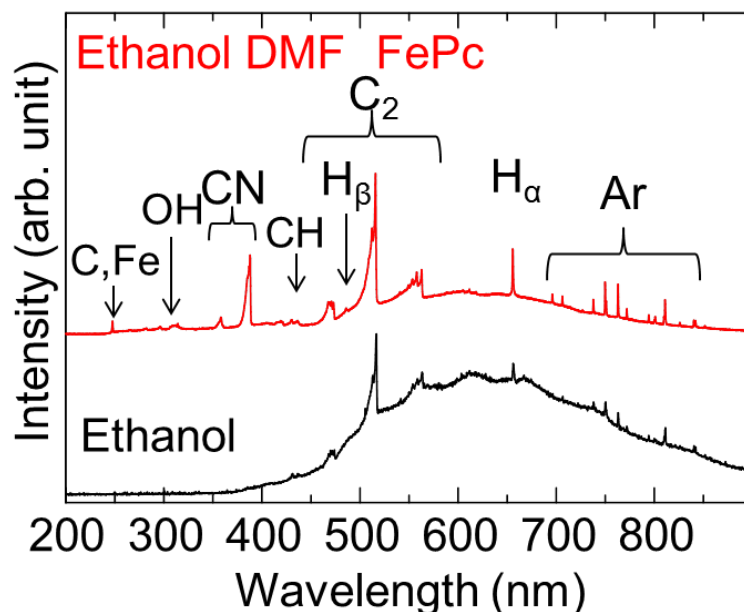


Fig. 4-5 Optical emission spectra with a range from 200 to 900 nm of the in-liquid plasma approach in ethanol with and without DMF-solvated FePc.

4.4 Effect of iron-phthalocyanine on flaky structure

A reason why the flake-like sheets were synthesized in the FePc in DMF-mixed ethanol solution is discussed. Effects for alcohols, solvents, and FePc were compared among them. Figure 4-6 shows a summary of the synthesis of the giant flakes of nanographene for the various conditions. The giant-size nanographene-flake syntheses were succeeded only in a mixture of FePc and ethanol, regardless of a kind of solvent. However, no flake appeared in both the DMF mixed ethanol without FePc and the hydrogen phthalocyanine (H₂Pc) added ethanol. Apparently, the molecular structure of H₂Pc and the solvents are not caused of the synthesis. Therefore, the giant graphene-flakes yielded only in the case of DMF-solvated FePc added ethanol.

A growth mechanism on the flake-like nanographene sheet with micrometer scales would be caused by iron-additives. Iron is in general used as a catalytic metal for the synthesis of carbon nanotubes (CNT).[17] For the CNT growth, the iron-catalytic effects are however with respect that its solubility of carbons enhances for the growth of multilayer of graphene.[18] In our case, iron of the FePc is just as a centered atom of the planer molecule of phthalocyanine. Thus the solubility of iron would not be effective in this study. In the high-crystalline nanographenes in the in-liquid plasma of pure ethanol, the nanographene sheets are reliable to be synthesized in ethanol as a graphene precursor. Possibly, the nanographene synthesis might occur to collect nanographene sheets for the growth of the characteristic flaky graphite with micrometer scales. Namely, one supposes that the giant graphene flakes formed by collection of nanographene sheets with the FePc effects.

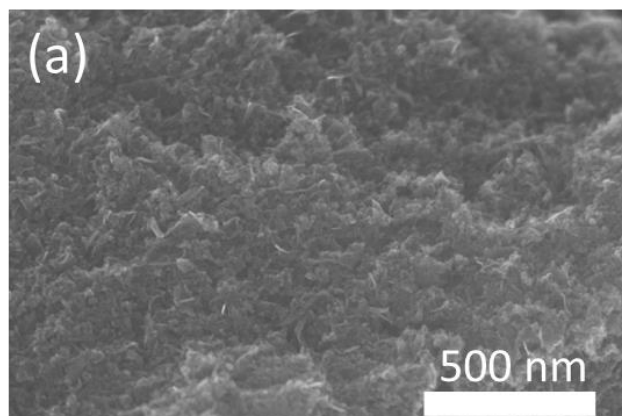
The other possibility is thought that intermediates for the flake-like growth were

catalyzed by iron during the in-liquid plasma of ethanol. It seems that iron inhibits to grow defective or amorphous carbons under oxidizing conditions brought by alcohols, involving an oxygen atom or a hydroxyl group, owing to the other alcohols yielded no similar intermediates for the sheet-like graphene synthesis. During the synthesis process of nanographene, the oxidizing effect removes effectively the amorphous carbons,[19] which inhibit to grow with the ordering growth of nanographene-flakes.

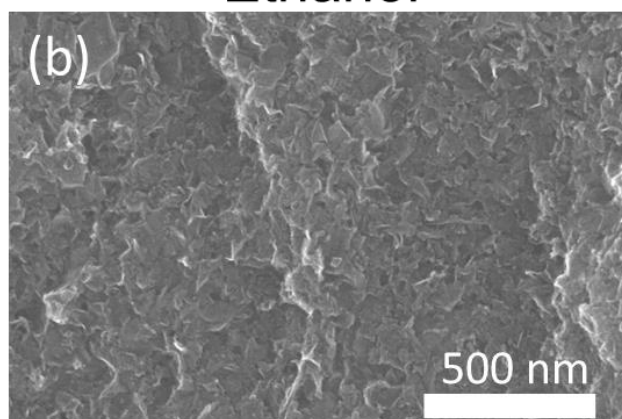
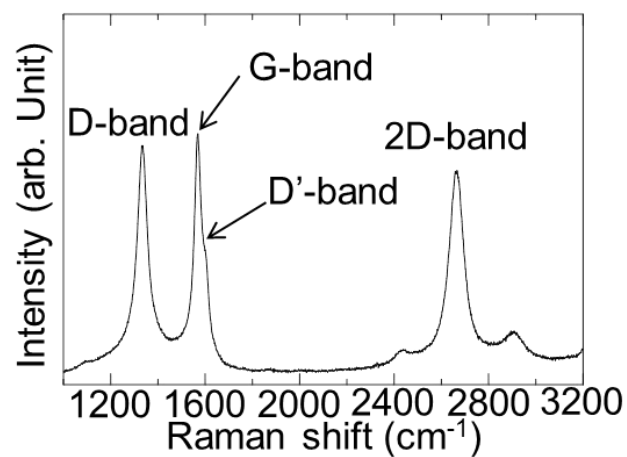
Overall of our interpretations, a proof of the FePc catalytic effect has not been completely obtained yet. For the case of FePc-added ethanol, iron predominantly caused that the FWHM of G-band revealed the high crystallinity graphene synthesis and less the amorphous carbons. As a consequence, it is remarked that the in-liquid plasma of ethanol with the additive of FePc was essential for true bottom-up growth of the giant nanographene-flakes in the facile liquid processing.

Table 4-1 Diagnostic parameters for plasma, synthesis rate and FWHM of G band in various synthesis conditions.

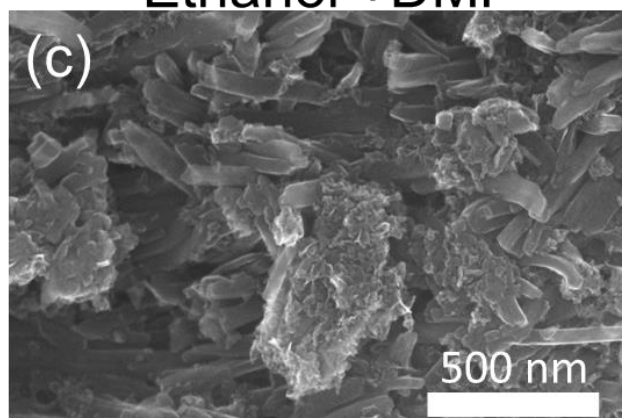
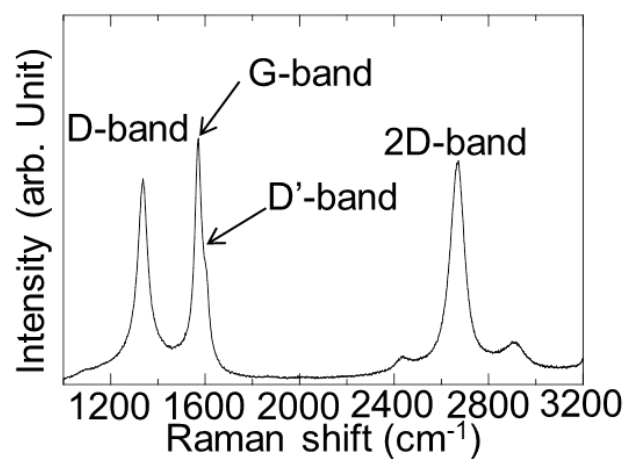
Alcohol	Solvent	Additive	Electron density ($\times 10^{14}$ cm^{-3})	Rotational temperature (K)	Vibrational temperature (K)	Synthesis amount after 30 min (mg)	FWHM of G band (cm^{-1})
Ethanol	-	-	4.7	2100	2000	9.2	40
Ethanol	DMF	-	5.0	2300	2100	5.5	35
Ethanol	DMF	H ₂ Pc	6.9	2650	2100	20.2	43
Ethanol	DMF	FePc	3.9	2600	2100	13.8	30
1-Propanol	DMF	FePc	4.5	2600	2000	21.7	39
1-Butanol	DMF	FePc	6.0	2600	1900	22.9	42



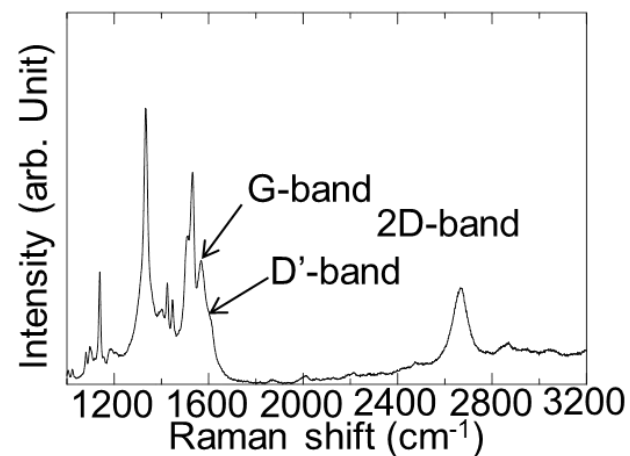
Ethanol



Ethanol +DMF



Ethanol+DMF+H₂Pc



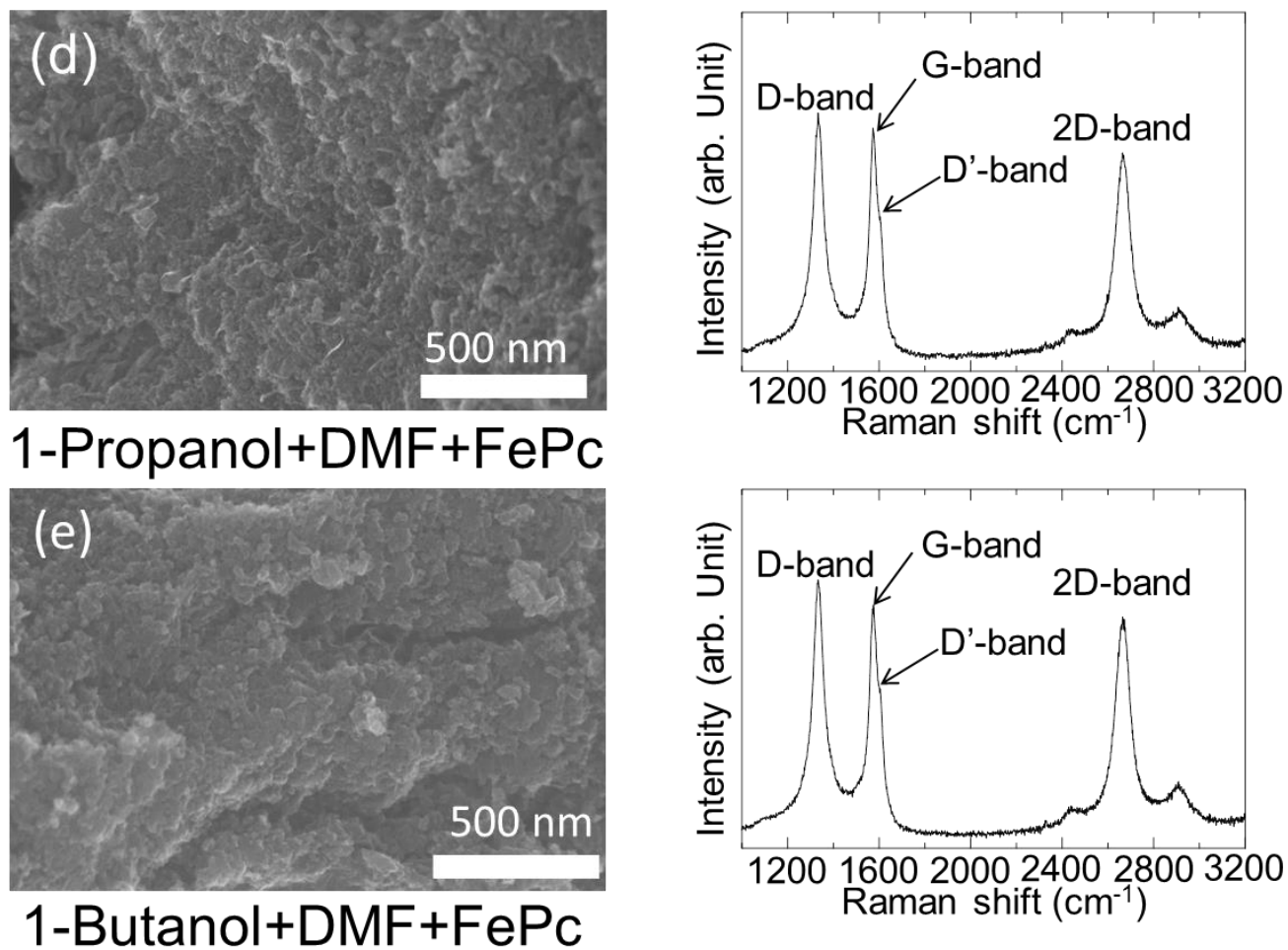


Fig. 4-6 SEM images (Left column) and Raman spectra (Right column) of carbon residues synthesized using the in-liquid plasma approach with (a) pure ethanol, (b) DMF-mixed ethanol, (c) DMF-solvated H_2Pc with added ethanol, (d) DMF-solvated FePc with added 1-propanol, and (e) DMF-solvated FePc with mixed 1-butanol.

4.5 Conclusion

The author and our group successfully synthesized the giant graphene-flakes employing the in-liquid plasma of ethanol with dispersion of iron phthalocyanine (FePc) in solvents. Regardless of the mixture of FePc, the plasma characteristics analyzed from the emissions were no significant changes therefore no effect on the synthesis of nanographene. The synthesized carbon residues were collected by a filter membrane. The residues were observed by SEM and analyzed by Raman scattering spectroscopy. As the results, the large flaky graphene with a size of approximately 1 μm was grown with a majority component of nanographenes, showing G band, D band, D' band, and 2D bands on the Raman spectra. The TEM images and TED patterns also indicated the several hundred nanometer sized sheet and graphene structures with a (002) interlayer spacing of 0.34 nm which is the same as for bulk graphite, respectively. Interestingly, the giant graphene-flakes could be synthesized only in solvated-FePc added ethanol, however not in the other than H₂Pc and alternative alcohols such as 1-propanol and 1-butanol. Iron may act effectively for an ordering collector of nanographenes, with iron catalytic reactions of aggregation or removal of amorphous carbons. From this study, it was found that the flake-shaped graphene could be synthesized by the bottom-up approach using the in-liquid plasma processing.

Reference

- [1] U. Khan, A. O'Neill, H. Porwal, P. May, K. Nawaz, and Jonathan N. Coleman. *Carbon* **50** (2012) 470.
- [2] D. Nuvoli, L. Valentini, V. Alzari, S. Scognamillo, S. B. Bon, M. Piccinini, J. Illescas, and A. Mariani. *J. Mater. Chem.*, **21** (2011) 3428.
- [3] S. Park, and R. S. Ruoff. *Nat. Nanotechnol.*, **4** (2009) 217.
- [4] M. Yi, and Z. Shen. *J. Mater. Chem. A*, **3** (2015) 11700.
- [5] W. S. Hummers, Jr and R. E. Offeman. *J. Am. Chem. Soc.* **80** (1958) 1339.
- [6] S. Jalili-Firoozinezhad, M. H. M. Moghadam, M. H. Ghanian, M. K. Ashtiani, H. Alimadadi, H. Baharvand, I. Martin, and A. Scherberich. *RSC Adv.*, **7** (2017) 39628.
- [7] H. C. Schniepp, J. L. Li, M. J. McAllister, H. Sai, M. Herrera-Alonso, D. H. Adamson, R. K. Prud'homme, R. Car, D. A. Saville, and I. A. Aksay. *J. Phys. Chem. B*, **110** (2006) 8535.
- [8] H. Lee, M. A. Bratescu, T. Ueno, and N. Saito. *RSC Adv.*, **4** (2014) 51758.
- [9] Y. Li, Q. Chen, K. Xu, T. Kaneko, and R. Hatakeyama. *Chem. Eng. J.*, **215** (2013) 45.
- [10] W. Choi, I. Lahiri, R. Seelaboyina, and Y. S. Kang. *Crit. Rev. Solid State Mater. Sci.* **35** (2010) 52.
- [11] H. F. Arani, A. R. Mirhabibi, S. Collins, R. Daroughegi, A. Khalife Soltani, R. Naghizadeh, N. Riahi-Noori, R. Aghababazadeh, and A. Westwood. *RSC Adv.*, **7** (2017) 5533.
- [12] I. Alstrup. *J. Catal.*, **109** (1988) 241.
- [13] M. José-Yacamán, M. Miki-Yoshida, L. Rendón, and J. G. Santiesteban. *Appl. Phys. Lett.* **62** (1993) 657.

- [14] X. Chen, J. Mazumder, and A. Purohit. *Appl. Phys. A* **52** (1991) 328.
- [15] H. R. Griem, *Plasma Spectroscopy* (McGraw-Hill, New York, 1964).
- [16] S. Takashima, M. Hori, T. Goto, A. Kono, M. Ito, and K. Yoneda. *Appl. Phys. Lett.* **75** (1999) 3929.
- [17] Y. Homma, Y. Kobayashi, T. Ogino, D. Takagi, R. Ito, Y. J. Jung, and P. M. Ajayan. *J. Phys. Chem. B*, **107** (2003) 12161
- [18] Y. Xue, B. Wu, Y. Guo, L. Huang, L. Jiang, J. Chen, D. Geng, Y. Liu, W. Hu, and G. Yu. *Nano Res.*, **4** (2011) 1208.
- [19] C. Bower, O. Zhou, W. Zhu, D. J. Werder, and S. Jim. *Appl. Phys. Lett.* **77** (2000) 2767.

Chapter 5

Structures and catalytic activity of carbon nanomaterial synthesized using iron phthalocyanine

5.1 Introduction

The synthesized nanographene with high crystallinity is supposed to be potentially useful as a support material in PEFCs. In the oxygen reduction reactions, the four-electron process of $O_2+4H^++4e^-\rightarrow H_2O$, not the two-electron process of $O_2+2H^++2e^-\rightarrow H_2O_2$, are necessary. However, the four-electron reactions were limited in the cases of the carbon material with iron phthalocyanine. Saito et al. reported the non-precious metal carbon nanomaterial catalysts synthesized in the plasma submerged in liquid.[1] In the alkaline conditions, the synthesized catalysts worked with almost four-electron process.[2-3] However, high activity with four electron reactions has not been shown under acidic media.

In this study, the author has studied catalytic activities of the in-liquid plasma synthesized carbon flakes with micrometer scale involving large amounts of high crystalline carbon nanomaterials as a catalyst containing Fe-N active sites. The oxygen

reduction reactions under realistic alkaline media were analyzed by electrochemical techniques. Dispersed solvents for the synthesized carbon-flakes depended slightly on the electrochemical properties. The carbon nanomaterial structure was characterized by physicochemical techniques such as transmission electron microscopy, Raman scattering spectroscopy. Different types of alcohol and electrode materials were studied.

5.2 Experimental details

The glass reactor, with an inner diameter of 108 mm, was filled with 160 ml of pure alcohol and 40 ml of dispersion solvent. Three types of pure alcohols, *viz.*, ethanol (C_2H_5OH), 1-propanol (C_3H_7OH), and 1-butanol (C_4H_9OH), were used to synthesize carbon nanomaterial. Tetrahydrofuran (THF) and N, N-dimethylformamide (DMF) were used as dispersion solvents. Iron phthalocyanine was used as a catalyst raw material. First, iron phthalocyanine is added to a dispersion solvent and dispersed for 30 min using a homogenizer. Next, the alcohol and the dispersion solvent are mixed and further dispersed for 10 min. The resulting solution is used as a catalyst synthesis solvent. Ar gas with a flow rate of 6 slm was introduced and filled the gas region at the upper half of the reactor. The pressure was maintained at the atmospheric pressure. These electrodes were positioned so as to sandwich the gas-liquid boundary. One electrode, the upper one, was placed in the gas phase. The other, lower electrode was immersed in the liquid phase. More specifically, the tip of the upper electrode was placed 1 mm above the liquid level. The 100-mm-long wire that was used as the lower electrode was immersed 9 mm below the liquid level in the alcohol. A graphite wire with a diameter of 3 mm, were used in this study. An AC (60 Hz) voltage of 9 kV was applied between the two electrodes. Plasmas were generated in the in-liquid between the gas phase, the gas-liquid boundary phase, and the liquid phase. Notably, since a large number of bubbles of alcohol vapor were generated in the liquid phase, the plasma in liquid appeared to reach the lower electrode position. The duration of discharge, which corresponded to the synthesis time, was typically 30 min.

Optical emission spectra (OES) of the plasma were measured in the gas-phase

region close to 3 mm above the liquid surface. Plasma emission emissions were measured using a multi channel spectrometer (Ocean Optics HR-4000).

After the syntheses, suction filtration with a filter (Millipore JAWP04700) collected solid materials as the synthesized compounds. The weights of the products were measured by an electronic balance. The weights of graphite electrodes decreased upon synthesis, which indicated that both electrodes were eroded by the plasma. The synthesis yields of carbon-containing materials were estimated by subtracting the weight of the eroded electrodes. The collected material was a composite of iron nitrogen-containing carbon nanomaterial.

Next, 5 mg of the FePc-alcohol-mixture-synthesized carbon nanomaterial was dispersed in the solution of a mixture of 490 μl of 2-propanol and 490 μl of ultrapure water. Then, 20 μl of 5% Nafion DE521 (Wako) diluted in water was added to the solution. The solution was homogenized for 30 min using a homogenizer. The homogenized solution 3 μl was coated onto a working electrode with an area of 0.07065 cm^2 , and then heated for 15 min at 65°C by evaporation of solvents. A three-electrode electrochemical cell with a rotating disk electrode (RDE) and a potentiostat (SI1287, Solartron Analytical.) was used for linear sweep voltammetry (LSV) at room temperature. The LSV was conducted by varying the potential from 0 to 1.0 V at a scan rate of 10 mV/s and the electrode rotation speed is 400, 900, 1600, 2500 rpm, in 0.1 M HClO_4 solution, purged with O_2 gas for 20 min before measurements. Cyclic voltammogram (CV) was measured by varying the potential from 0.05 to 1.2 V with a scan rate of 50 mV/s. A reference potential was measured by a reversible hydrogen electrode. A Pt wire was used for the counter electrode.

5.3 Synthesis characteristics by in-liquid plasma with FePc

The in-liquid plasma was analyzed by using optical emission spectroscopic technique. Figure 5-1 shows the typical emission spectra of the plasma generated by the combination of the graphite electrode and ethanol. It shows the spectra ranged between 200 and 900 nm. Emission of Fe, OH, CN, CH, H, C₂ derived from the solution and Ar derived from the plasma was observed. In particular, CN appeared in the case of using DMF. From this, the emission of CN is derived from DMF, not iron phthalocyanine. Next, the electron density in the plasma was determined from the peak of H_β (486.13 nm)[4]. By the Voigtian fitting, stark broadening widths were obtained and then electron densities were estimated [5]. The electron density at the THF solvent is $7.4 \times 10^{14} \text{ cm}^{-3}$ for ethanol, $8.8 \times 10^{14} \text{ cm}^{-3}$ for 1-propanol and $9.6 \times 10^{14} \text{ cm}^{-3}$ for 1-butanol. The electron density in the DMF solvent is $3.9 \times 10^{14} \text{ cm}^{-3}$ in ethanol, $4.5 \times 10^{14} \text{ cm}^{-3}$ in 1-propanol and $6.0 \times 10^{14} \text{ cm}^{-3}$ in 1-butanol. The electron density increased with increasing the molecular-weight of alcohol. Probably, electrical conductivity of alcohol may be a main factor, because of high electrical current flows in alcohols with high molecular weight. The electron density increased with increasing the flowing current.

In addition, the synthesis amount for 30 minutes was ethanol, 1-propanol and 1-butanol. 26.3, 47.1 and 61.5 mg of carbon nanomaterials were synthesized using the THF for synthesis duration of thirty minutes. 13.8, 21.7 and 22.9 mg of carbon nanomaterials were synthesized using the DMF for synthesis duration of thirty minutes.

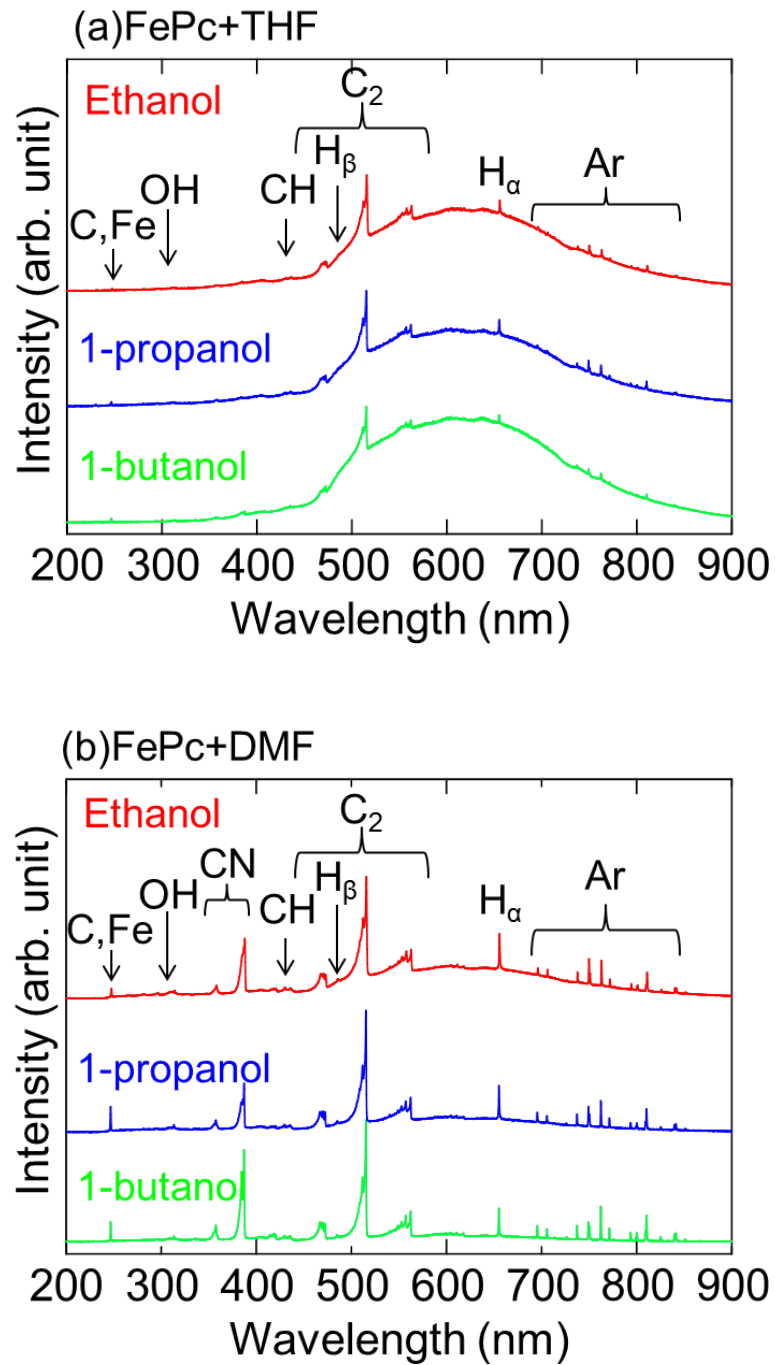


Fig. 5-1 Optical emission spectrum of the in-liquid plasma spectral range from 200 to 900 nm.

5.4 Structural and morphologic properties

Figure 5-2 (a) and (b) show Raman spectra of carbon nanomaterials synthesized using the THF and the DMF solvent, respectively. Four significant peaks, which typically appear in the carbon nanomaterials, were clearly found in all spectra. G-band and 2D-band peaks at 1580 and 2700 cm^{-1} , respectively, are caused by six-membered ring structures. D-band and D'-band peaks at 1340 and 1620 cm^{-1} , respectively, are caused by defects and edges of six-membered rings. Smaller FWHM value of the G-band peak indicates a degree of perfection of six-membered ring structures. In the case using the THF solvents, the FWHM values of G-band peaks are 34, 49 and 58 cm^{-1} for the carbon nanomaterials synthesized by ethanol, 1-propanol and 1-butanol, respectively. Those by the graphite electrodes are 30, 39 and 42 cm^{-1} for the cases using ethanol, 1-propanol and 1-butanol, respectively. This means that high-degree of perfection of six-membered ring carbon nanomaterials were synthesized using lower-molecular-weight alcohols, regardless of electrodes. The carbon nanomaterials using ethanol were synthesized with high crystallinity because small FWHM values of the G-band peak were comparable to those of CVD-grown graphene and HOPG.

The I_D / I_G ratio in the THF solvent was 1.66 for ethanol, 1.87 for 1-propanol and 1.94 for 1-butanol. The I_D / I_G ratio in the DMF solvent was 1.25 for ethanol, 1.47 for 1-propanol and 1.84 for 1-butanol. In the case using the THF solvent, the sizes of crystallites in carbon nanomaterials synthesized by ethanol, 1-propanol, and 1-butanol, were 11.6, 10.3 and 9.9 nm, respectively. Those using the DMF solvent were 15.3, 13.1 and 10.5 nm for ethanol, 1-propanol, and 1-butanol, respectively.[6] The sizes of crystallites were large when the lower-molecular-weight alcohols and the DMF solvent

were used. These results clarified the trade-off relationship between the synthesis rate and the crystallinity, as indicated in the FWHM value of G-band peak and the size of crystallite. The FWHM values of G-band peaks for the samples used by the graphite electrode were smaller. This means that the lower distortion of six-membered ring structures was realized by the DMF solvent. Further, crystallinity is higher when using DMF than THF. It is conceivable that the plasma density was suppressed by DMF, the C having a non-6-membered ring bond was suppressed, and the proportion of C having a 6-membered ring bond relatively increased.

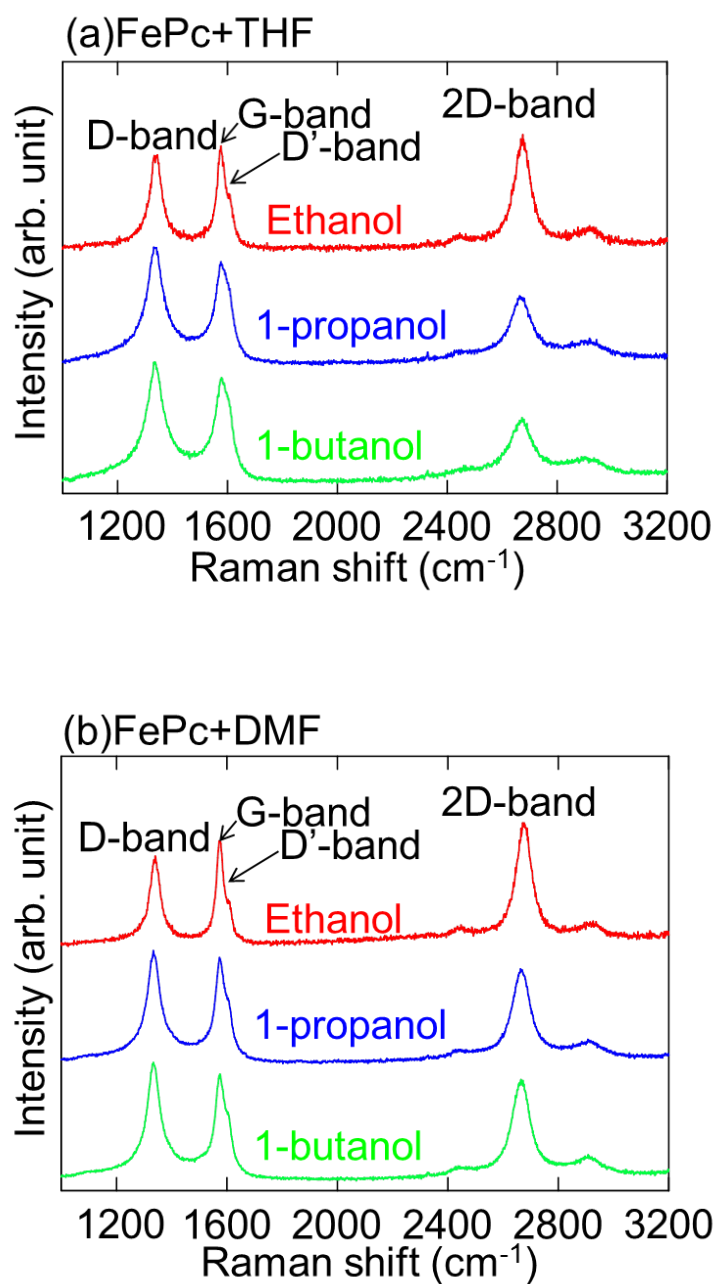


Fig. 5-2 Raman spectra of carbon nanomaterials synthesized by the in-liquid plasma using the THF and the DMF solvent with ethanol, 1-propanol, and 1-butanol, respectively.

Figure 5-3 shows the SEM image of the synthesized carbon nanomaterial. It was found to be flaky shape in samples synthesized with ethanol from here. However, no flaky compound was found under other conditions. This is a growth mechanism on the flake-like carbon nanomaterial sheet with micrometer scales would be caused by iron-additives [7]. In our case, the iron of the FePc is just as a centered atom of the planer molecule of phthalocyanine. Thus the solubility of iron would not be effective in this study. In the high-crystalline carbon nanomaterials in the in-liquid plasma of pure ethanol, the carbon nanomaterial sheets are reliable to be synthesized in ethanol as a graphene precursor. However, it is thought that the synthesis of amorphous carbon is large in the case other than ethanol and catalytic effect did not occur.

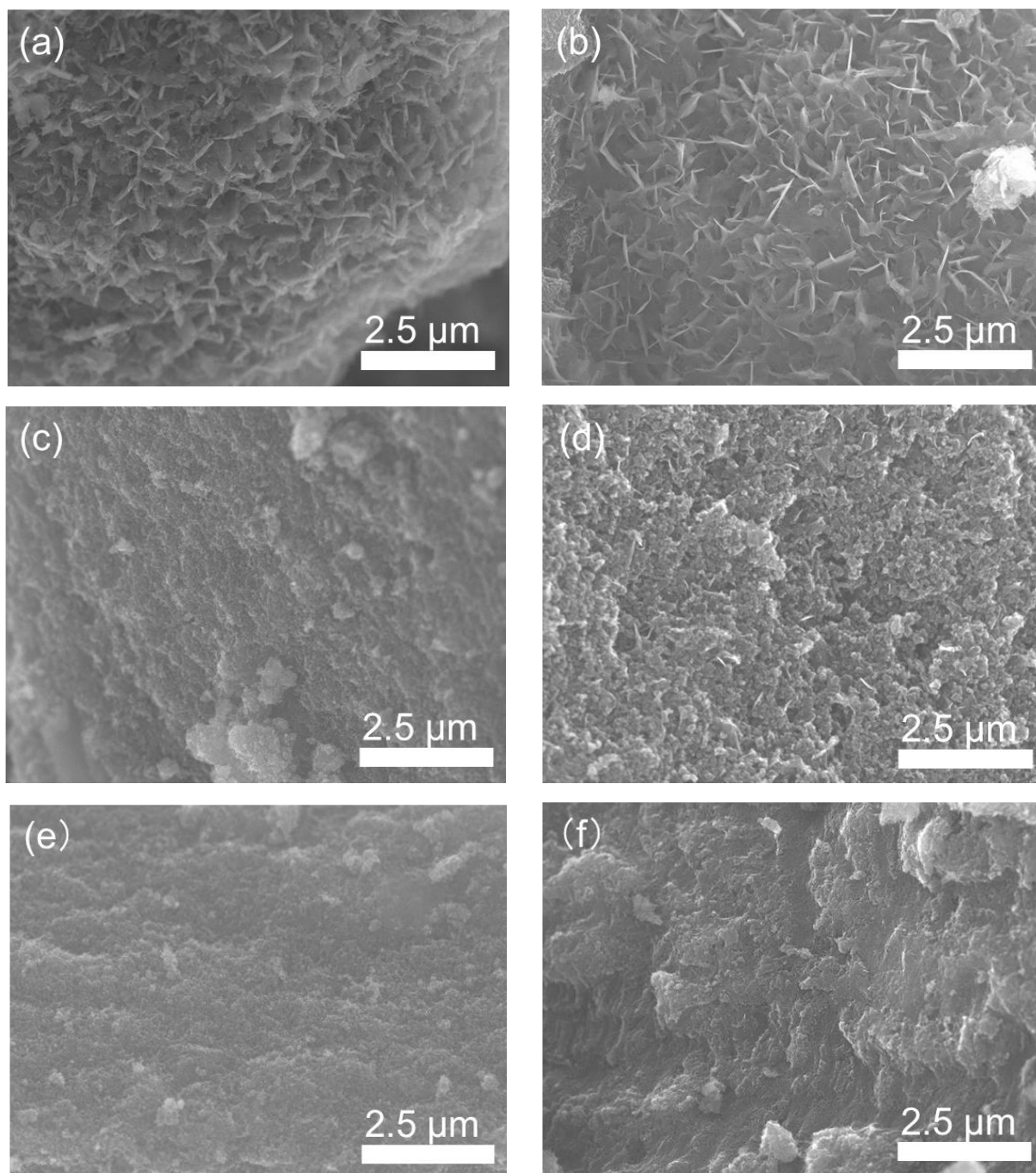


Fig. 5-3 SEM image of the synthesized carbon nanomaterial.(a) ethanol added with THF-solvated FePc, (b) ethanol added with DMF-solvated FePc, (c) 1-propanol added with THF-solvated FePc, (d) 1-propanol added with DMF-solvated FePc, (e) 1-butanol added with THF-solvated FePc, (f) 1-butanol added with DMF-solvated FePc.

5.5 Catalytic activity of iron-nitrogen doped carbon nano material

5.5.1 Composition and chemical bonding states

The surface of synthesized carbon nanomaterial was examined using by XPS. Figure 5-4 shows the N1s peak using the XPS. The peak of N1s was standardized by the integrated value of C1s. The N 1s peaks were decomposed into four components of pyridinic N (398.6 eV), Fe-N (399.3 eV), pyrrolic N (400.1 eV), and graphitic N (401.1 eV) bonding states. The total contents of N in the sample are estimated to 6 at% and 11 at% for THF and DMF, respectively. The DMF sample obtained contents of 2 at% for pyridinic N, 5.2 at% for Fe-N, 1.6 at% for pyrrolic N, and 2.2 at% for graphitic N; these values are almost twice as high as the 1 at%, 2.5 at%, 1.4 at%, and 0.9 at% for the THF sample, respectively. Fe contents were 2.1 at% for THF and 1.7 at% for DMF. These values are listed in Table 5-1. In the sample dispersed with DMF, the bond peak of graphitic is increased. It is observed a peak of CN only if DMF was used from OES results, considered that it would be contributed to increased binding of graphitic by the can CN.

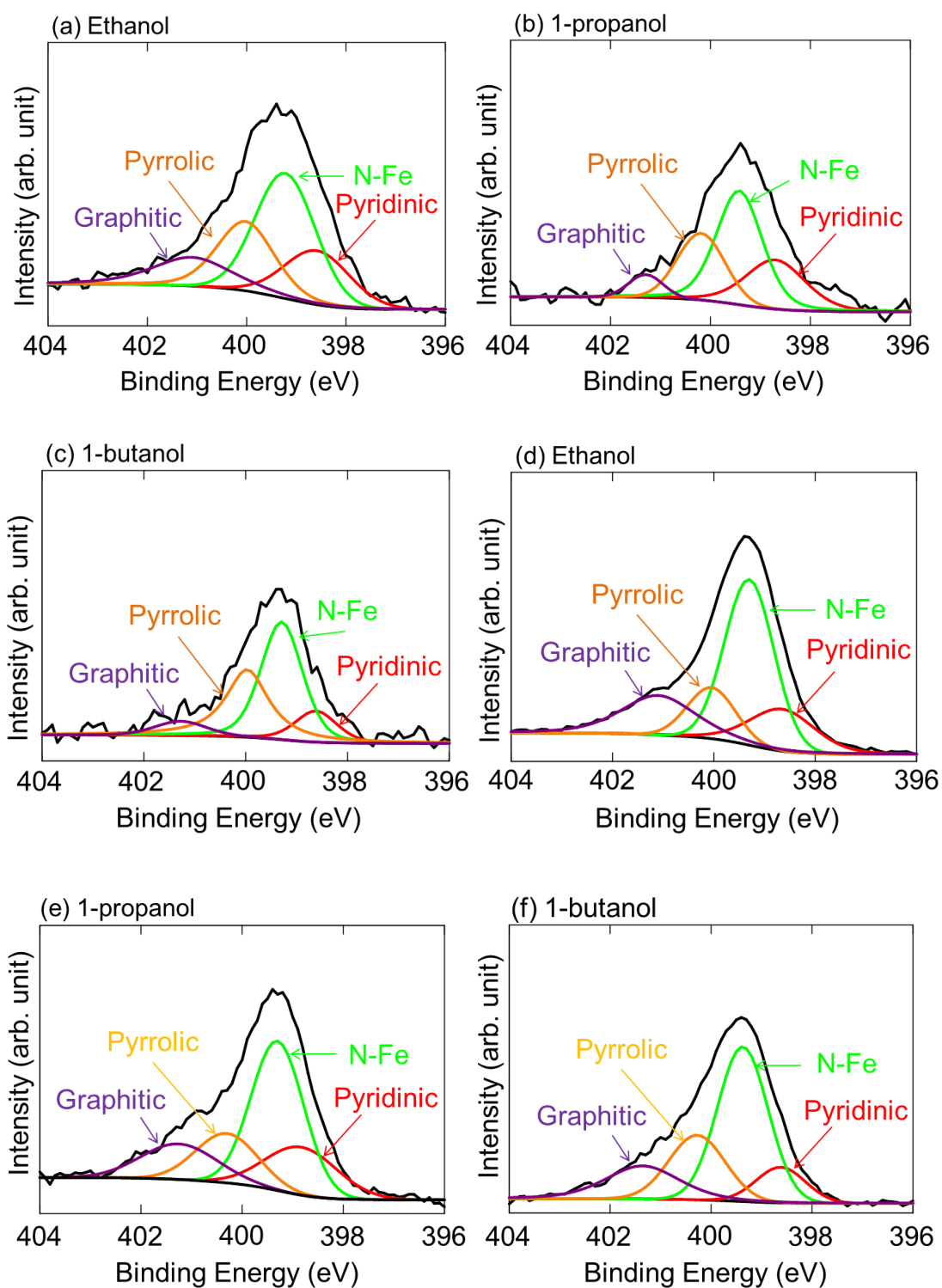


Fig. 5-4 High-resolution XPS N1s spectra of (a-c)THF and (d-f)DMF.

Table 5-1 Surface elemental composition of FePc with DMF- and THF- mixed alcohol obtained from the XPS measurements.

		C (at%)	N (at%)	Pyridinic N (at%)	Fe-N (at%)	Pyrrolic N (at%)	Graphitic N (at%)	O (at%)	Fe (at%)
	Ethanol	84.56	5.99	1.17	2.46	1.44	0.92	7.34	2.12
THF	1-propanol	88.16	3.39	0.85	1.51	1.68	0.41	7.50	0.98
	1-butanol	90.47	2.04	0.25	0.94	0.71	0.14	6.67	0.82
	Ethanol	66.79	10.83	1.89	5.16	1.55	2.23	20.65	1.73
DMF	1-propanol	77.55	6.63	1.34	3.05	1.19	1.19	14.66	1.16
	1-butanol	85.65	5.24	0.58	2.56	1.19	0.91	8.23	0.89

5.5.2 Catalytic activity

Cyclic voltammogram (CV) measured in a 0.1 M HClO₄ solutions saturated with O₂ at a scan rate of 50 mV/s are shown in Figure 5-5. Reduction peaks in the CV curve are clearly visible at 0.55, 0.42 and 0.35 V for THF and 0.64, 0.59 and 0.47 V for the DMF samples. These potentials were referenced to the RHE. Oxygen reduction reaction measurements were made in O₂-saturated 0.1M HClO₄ at a scan rate of 10 mV/s. Linear sweep voltammetry (LSV) curves are shown in Figure 5-6. Also, Figure 5-6 when synthesized using ethanol, 1-propanol, 1-butanol, oxygen reduction onset potentials are 0.86, 0.72 and 0.70 V vs.RHE in the case of THF. Also, when synthesized using ethanol, 1-propanol, 1-butanol, the oxygen reduction onset potential are 0.89, 0.87 and 0.74 V vs.RHE, respectively in the case of DMF. It can be seen that a catalyst using a low molecular weight alcohol exhibits the higher catalytic activity. The current density at the time of 0.2 V vs.RHE at the time of dispersion using THF are 3.64, 2.98 and 2.94 mA/cm² for ethanol, 1-propanol and 1-butanol, respectively. The current density at 0.2 V vs.RHE during dispersion using DMF are 4.29, 4.46, 2.59 mA/cm² for ethanol, 1-propanol and 1-butanol, respectively. Furthermore, the transferred electron number per oxygen molecule involved in the oxygen reduction at each of the electrodes is determined by the Koutecky–Levich (KL) equation

$$\frac{1}{j} = \frac{1}{j_k} + \frac{1}{B\omega^{1/2}} \quad , \quad (1)$$

$$B = 0.2nFD_0^{2/3}\nu^{-1/6}C_0 \quad , \quad (2)$$

where j is the measured current density, j_k is the kinetic current density, ω is the electrode rotating rate, n represents the number of electrons transferred per oxygen molecule, F is the Faraday constant ($F = 96485 \text{ C mol}^{-1}$), D_0 is the diffusion coefficient

of O_2 in 0.1 M $HClO_4$ ($1.9 \times 10^{-5} \text{ cm}^2/\text{s}$), ν is the kinetic viscosity ($0.01 \text{ cm}^2/\text{s}$), and C_0 is the bulk concentration of O_2 ($1.2 \times 10^{-6} \text{ mol}/\text{cm}^3$) [8]. The constant 0.2 is used when the rotation speed is expressed in rpm. According to equations, the number of transferred electrons can be obtained from the slope of the Koutecky–Levich (KL) plots.

Figure 5-6 shows a series of polarization curves for the ORR recorded with the rotation speeds from 400 to 2500 rpm. In these polarization curves, currents increased with the higher rotation speeds. The KL plots at different potentials are shown in Fig. 5-7. Linear relationships in the KL plots were fitted by lines. The first-order reaction kinetics toward the concentration of dissolved oxygen and a similar electron transfer number for LSV at 0.1 V vs. RHE in the acidic solution were estimated the electron transfer numbers of 2.28 for the THF sample and 3.14 for the DMF sample. Even though the acidic solutions, the synthesized samples shows the relatively large electron number of almost ideal four were obtained.

Fe-N bonds are considered to contribute to the catalytic activity.[9] From the results of XPS, the samples contained relatively large amounts of Fe-N bonding states, possibly owing to the use of the precursor FePc. To obtain the ideal transfer electron number of 4, the carbon nanomaterial properties surrounding the Fe-N active sites are also important. In addition, this result is less than the ideal number of transfer electrons. It is thought that the binding of Fe-N bonding in the composite was weakly coupled with carbon nanomaterial and the conductivity became low.[10] Therefore, if we can fix Fe-N bonds on carbon nanomaterials by annealing etc., it seems that activity may be further improved. The synthesized carbon nanomaterials using DMF achieved higher crystallization, thinner flake width, and smaller carbon nanomaterial-domain sizes than using THF; this was observed from the results of the Raman measurements. Further, the

sample using DMF had higher catalytic activity than that using THF. This could be attributed to the large Fe-N content. Consequently, the in-liquid plasma syntheses provided non-precious-metal catalysts with high catalytic activity owing to the highly crystalline carbon nanomaterials with large surface areas

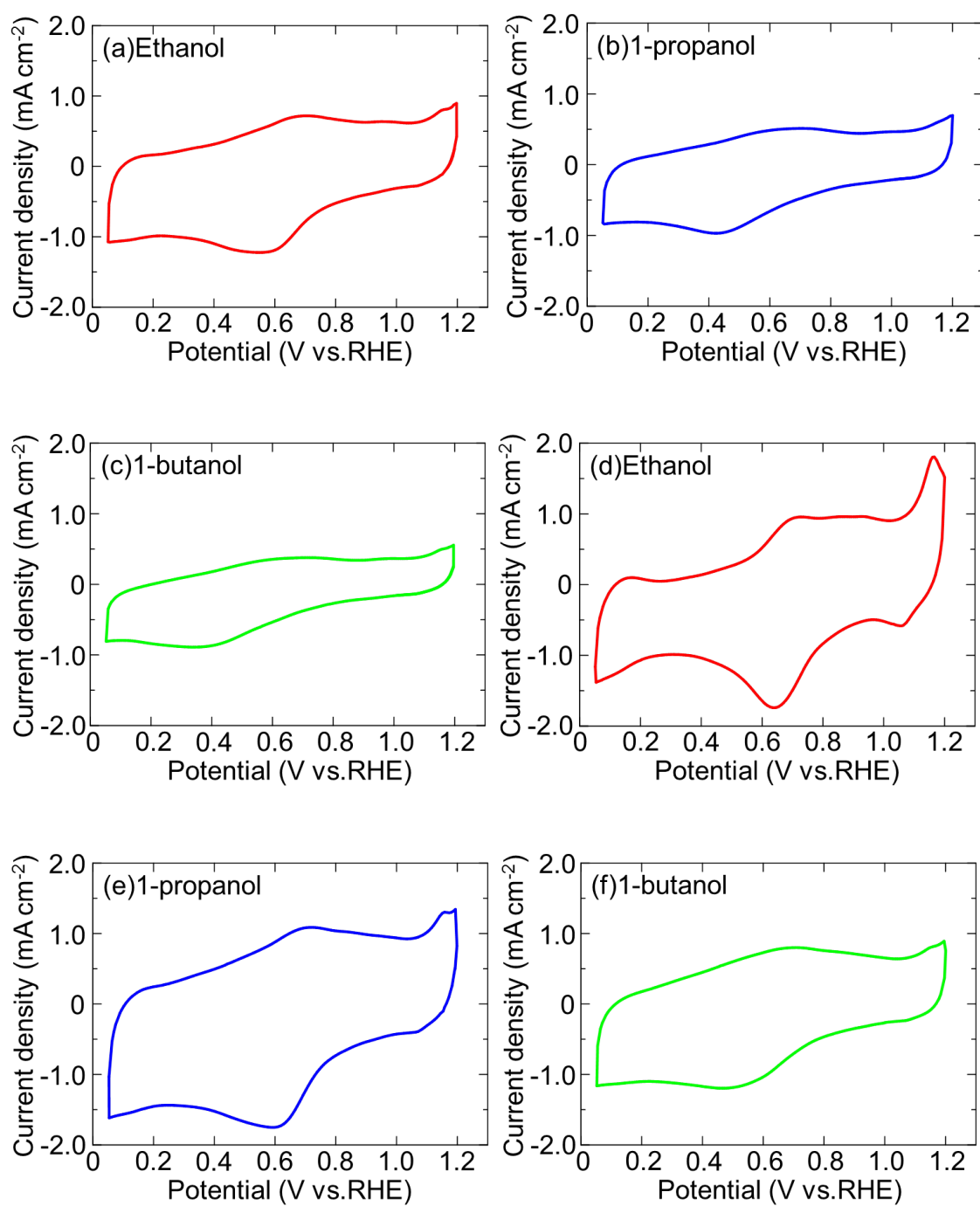


Fig. 5-5 Cyclic voltammograms using carbon nanomaterials curves of the (a-c) THF, and (d-f) DMF, samples in O₂-saturated 0.1M HClO₄ at a scan rate of 50 mV/s.

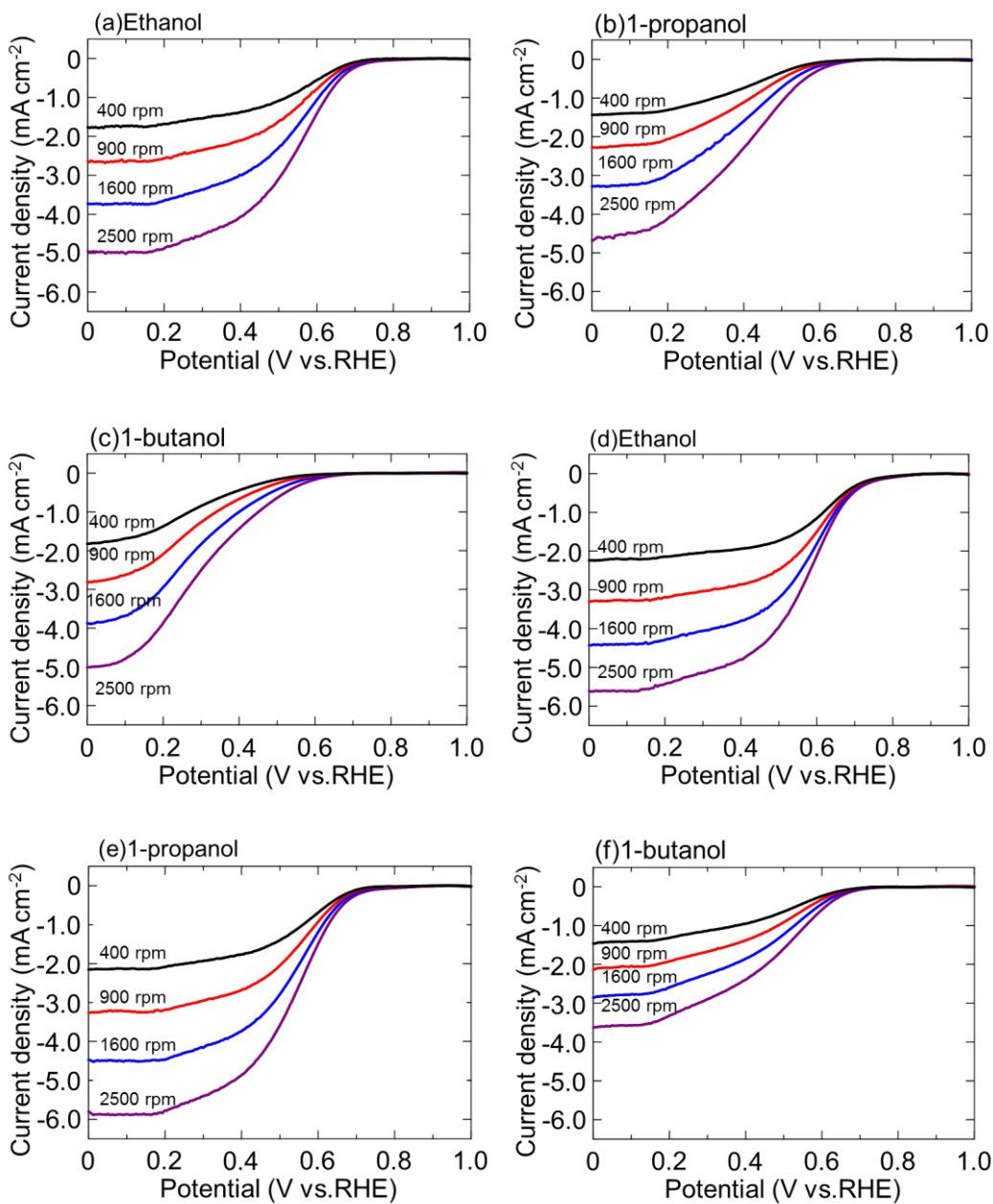


Fig. 5-6 LSV curves of the (a-c)THF, and (d-f)DMF samples in O₂-saturated 0.1M HClO₄ at a scan rate of 10 mV/s.

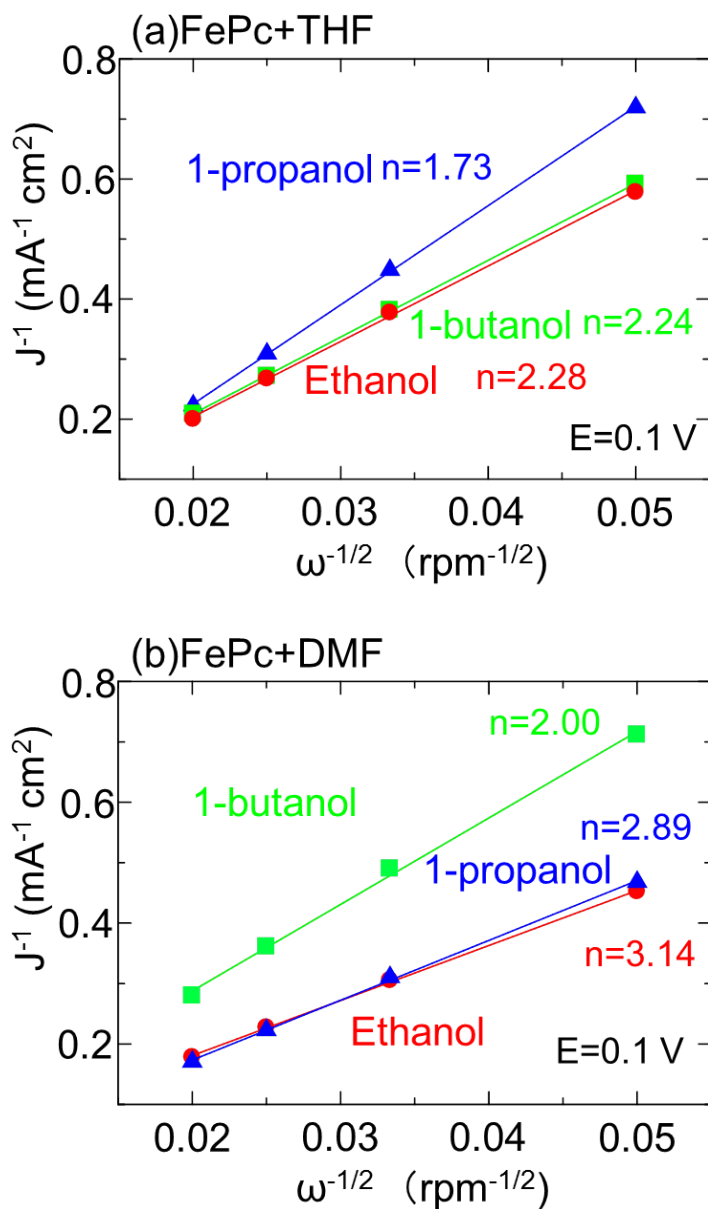


Fig. 5-7 LSV curves of the (a)THF, and (c)DMF samples in O₂-saturated 0.1M HClO₄ at a scan rate of 10 mV/s. Koutecky-Levich plots.

5.6 Conclusion

Carbon nanomaterials were synthesized by using in-liquid plasma of ethanol adding iron phthalocyanine that dissolved into solvents such as THF or DMF. From the data of OES, the electron density at the THF solvent is $7.4 \times 10^{14} \text{ cm}^{-3}$ for ethanol, $8.8 \times 10^{14} \text{ cm}^{-3}$ for 1-propanol and $9.6 \times 10^{14} \text{ cm}^{-3}$ for 1-butanol. The electron density in the DMF solvent is $3.9 \times 10^{14} \text{ cm}^{-3}$ in ethanol, $4.5 \times 10^{14} \text{ cm}^{-3}$ in 1-propanol and $6.0 \times 10^{14} \text{ cm}^{-3}$ in 1-butanol. The electron density increases as the molecular weight of alcohol increases. Furthermore, dependence of synthesis amount and electron density was observed. Regardless of types of solvent, the larger amount of carbon nanomaterials was synthesized by the higher-molecular-weight alcohols. 26.3, 47.1 and 61.5 mg of carbon nanomaterials were synthesized using the THF solvent for thirty minutes. Additionally, 13.8, 21.7 and 22.9 mg of carbon nanomaterials were synthesized using the DMF solvent for thirty minutes. On the other hand, according to the Raman spectra, using the lower-molecular-weight alcohols, the crystallinity of carbon nanomaterials became higher, in which the width of G-band peak became narrower and the relative intensity of D-band peak smaller. There is the trade-off relationship between the synthesis rate and crystallinity depending on the types of alcohols. In addition, by using the DMF solvent, the width of G-band peak became narrower, while the domain size was larger. The surface condition of the graphene synthesized from the SEM image was confirmed. It was found that the sample was synthesized using ethanol to form a sheet. Other things were not sheets but the same as conventional carbon nanomaterials were made.

Reference

- [1] K. Hyun, T. Ueno, G. Panomsuwan, O. L. Li, and N. Saito. *Phys.Chem.Chem.Phys.* **18** (2016) 10856.
- [2] D. Kim, O. L. Li, and N. Saito. *Phys.Chem.Chem.Phys.* **16** (2014) 14905.
- [3] L. Li, S. Chiba, Y. Wada, G. Panomsuwan, and T. Ishizaki. *J. Mater. Chem. A* **5** (2017) 2073.
- [4] H. R. Griem, *Plasma Spectroscopy* (McGraw-Hill, New York, 1964).
- [5] S.Takashima, M. Hori, T. Goto. A. Kono, M. Ito, and K. Yoneda, *Appl. Phys. Lett.* **75** (1999) 3929.
- [6] M. A. Pimenta, G. Dresselhaus, M. S. Dresselhaus, L. G. Cancado, A. Jorio, and R. Saito, *Phys. Chem. Chem. Phys.* **9** (2007) 1276.
- [7] T. Amano, H. Kondo, K. Ishikawa, T. Tsutsumi, K. Takeda, M. Hiramatsu, M. Sekine, and M. Hori. *Appl. Phys. Express* **11**, (2018) 015102.
- [8] L. Lin, Q. Zhu, and A. W. Xu. *J. Am. Chem. Soc.* **136** (2014) 11027.
- [9] K. Liu, S. Kattel, V. R. Mao, and G. Wang. *J. Phys. Chem. C* **120** (2016) 1586.
- [10] Y. Zhang, A. Thomas, M. Antonietti, and X. Wang, *J. Am. Chem. Soc.* **131** (2009) 50.

Chapter 6

Conclusions and future works

6.1 Summary of this thesis

In this paper, from the viewpoint that synthesis method using in-liquid plasma is advantageous as compared with the conventional carbon nanomaterial synthesis method, the application destination of synthesized nanographene was clarified and the synthesis process and characterization were clarified. Nanographene synthesized by in-liquid plasma can be synthesized at high speed and has high crystallinity. In addition, as a result of applying nanographene to a catalyst electrode for a fuel cell, it was suggested that the lifetime of the fuel cell could be prolonged. It was also suggested that it is possible to realize platinum substitution catalyst by using nanographene. The outline of each chapter is briefly explained below.

In chapter 1, the structures and properties of carbon nanomaterials are described. Graphene composed of a two-dimensional sheet had characteristic structural features and exhibited unique electronic properties. Furthermore, the definition and problems of nanographene and conventional graphene synthesis method are summarized. The authors emphasized the superiority of nanographene synthesis using underwater plasma.

Next, the current state and problems of fuel cells are described. Author described the superiority of polymer electrolyte fuel cell and its problems. Finally, as a problem of the fuel cell, there are degradation of the catalyst carrier and exploration of the non-precious metal catalyst, but introduction that the prior research is being conducted.

In Chapter 2, the in-liquid plasma device for synthesizing nanographene was described. The amorphous carbon removal treatment of the synthesized graphene and the platinum supporting process were shown. Various evaluation methods of the nanographene were also described. The principles of the evaluation methods and analyses techniques such as optical Emission spectroscopy (OES), Raman spectroscopy, X-ray diffraction (XRD), scanning electron microscopy (SEM), transfer electron microscopy (TEM), X-ray photoelectron spectroscopy (XPS), and electrochemical measurement were explained.

In Chapter 3, the nanographene synthesized in in-liquid plasma had highly durable catalyst-support-property in applications of polymer electrolyte fuel-cells (PEFC). A in-liquid plasma was generated using copper or graphite electrodes positioned outside and within ethanol, 1-propanol, or 1-buthanol. The higher the electron density derived from the spectrum of H_{β} , the higher the synthesis amount. There was a trade-off relationship between the synthesis rate and the crystallinity of nanographenes depending on kinds of alcohols employed as a liquid. When copper electrode was used, copper was found to be mixed in nanographene. It was found that when platinum fine particles were supported on these graphenes, PtCu alloy nanoparticles were produced. The nanographene synthesized using the ethanol was hardly degraded in a high-potential cycle test of the half-cell, e.g., only loss of 10% in effective surface area of Pt even after 10,000 cycles. The better catalyst-support property in the PEFC was obtained by the

nanographene with the narrower width of the G-band peak in the Raman spectra, owing to perfect formation of six-membered ring carbons, rather than that with wider domain sizes of the crystallites.

In Chapter 4, giant graphene-flakes with a size of micrometer scale were grown in liquid phase of submerged plasmas of iron-phthalocyanine (FePc)-added ethanol. The atmospheric pressure plasmas were generated in Ar gas phase and in liquid phase comprising of bubbles and liquid-solution. The mixture of FePC in ethanol was essential for the formation of giant graphene-flakes of aggregates of nanographenes, confirming by D, G and 2D bands in the Raman spectra. From the results of TEM and TED, it was confirmed several hundred nanometer order of the sheet is graphite confirmed. Also, it could not have been changing the type of alcohol and the complex. This suggested the possibility of metal catalytic effect.

In Chapter 5, iron phthalocyanine mixed nanographenes were synthesized by in-liquid plasma using the ethanol, the 1-propanol and the 1-buthanol. Then, their catalytic activity was evaluated. The amount of synthesis also increased in proportion to the number of C atoms in alcohol. As a result, the high catalytic activity was obtained in iron phthalocyanine mixed nanographene synthesized with ethanol. The author discussed the relationship between the results and catalytic activity. The onset potential increased with the proportion of Fe-N bond contributing to catalytic activity.

6.2 Scopes for future works

The author found that the crystallinity and synthesis rate of nanographene can be controlled by changing alcohol species from this study. It was found that the nanographene having high crystallinity exhibits high durability as a catalyst carrier of a catalyst electrode for a fuel cell. In addition, author think that measurement of plasma reaction in liquid is necessary to develop this research. Analysis was carried out based on information obtained from light emission in the gas phase portion in this measurement system. However, in the liquid phase it is not easy to measure in the current system. This is because the synthetic solvent changes to black as the plasma reaction progresses, so that the light emission in the solution is attenuated. Although it is possible to evaluate the product after synthesis by analysis using GC-MS, it is difficult to explain the mechanism by which alcohol converts to graphene during synthesis. Although the electron density in the gas phase was derived this time, the liquid density has a higher molecular density than the gas phase, so the reaction amount is large, so the electron density is considered to be different. From these facts, it is necessary to investigate not only the gas phase but also the liquid phase. As a result of carrying out the catalyst durability test, the catalyst exhibited high catalyst durability in nanographenes having high crystallinity. Based on this result, we think that there is a need to control the structure of nanographene while maintaining crystallinity and aim for improvement of catalytic activity.

It was found that sheet-like carbon was synthesized by mixing plasma with dispersing solvent and FePc in ethanol to generate plasma. We found the result that the

sheet can be formed in this experiment, but the reason why it grew into a sheet shape is not known in detail. It is necessary to investigate whether this is due to metal or synthesized in gas phase or liquid phase. In this plasma measurement, gas phase plasma was measured. However, it has hardly been investigated in the liquid phase. Therefore, it is necessary to develop a method that can measure in real time in liquid. Also, a sheet-shaped carbon material was synthesized, but it turned into a ring as a result of the TED pattern. This indicates that the directions of crystal planes are uneven and can not be regarded as a sheet of graphene. Therefore, the sheet there is a need to investigate further what it is. The Author believe that the reaction process in the liquid phase is identified and contributes to the future development of plasma science.

Then, we discovered the possibility of nanographene synthesized by mixing FePc as a platinum substitution catalyst. However, it is still far from practical use when compared with platinum. In addition, it was found that the synthesized nanographene contains a large amount of oxygen. We think that it is necessary to reduce them because they can be one of the factors increasing the resistance in nanographene. Therefore, it is necessary to elucidate the influence of other transition metals and other elements such as N₂ plasma on nanographenes caused by containing different elements. In order to realize this, it is necessary to develop calculation method of synthesis process and new measuring method of in-liquid plasma. The current problem is that electron transfer is not smooth. On the other hand, it is necessary to strongly immobilize Fe-N bond showing catalytic ability on graphene. For this, it is necessary to study annealing and acid treatment of synthesized nanographene in the future. By advancing these things, it will become clear that what can and can not be done in liquid synthesis. And I think that it may be able to generate reactions that we could not do by devising processes.

Acknowledgements

The present research was performed in Professor Hori and Professor Ishikawa Laboratory, Department of Electrical Engineering and Computer Science, Nagoya University. Author would like to appreciate his research advisor, Professor Masaru Hori, Institute of Innovation for Future Society, Nagoya University, for his guidance, advices, and encouragements through the course of this research. The author also would like to thank his vice-advisors, Professor Kenji Ishikawa, Plasma Nanotechnology Research Center, Nagoya University, and associate Professor Hiroki Kondo, Plasma Nanotechnology Research Center, Nagoya University, for lots of valuable comments. The author also would like to thank his vice-advisers, Professor Nagahiro Saito, Department of Chemical Systems Engineering, Nagoya University, Professor Yutaka Ohno, Department of Electrical Engineering, Nagoya University, and Professor Satoshi Iwata, Institute of Materials and Systems for Sustainability, Nagoya University, for their guidance and valuable suggestions in preparing this thesis.

The author is enormous grateful to Professor Mineo Hiramatsu, Professor Masafumi Ito, and Professor Takayuki Ohta, Associate Professor Keigo Takeda, Department of Electrical and Electronic Engineering, Meijo University, Professor Makoto Sekine, Professor Osamu Oda, Professor Toshio Hayashi, Professor Hitoshi Ito, Professor Naohiro Shimizu, Assistant Professor Takayoshi Tsutsumi, Plasma Nanotechnology Research Center, Nagoya University, Lecturer Hiromasa Tanaka, and Assistant professor Hiroshi Hashizume, Institute of Innovation for Future Society, Nagoya University, for their valuable comments and suggestions.

He also thanks Dr. Yudai Miyawaki, Dr. Hironao Shimoeda, Dr. Toshiya Suzuki, Dr.

Acknowledgements

Hyung Jun Cho, Dr. Lu Yi, Dr. Yusuke Kondo, Dr. Lingyun Jia, Dr. Zecheng Liu, Dr. Naoyuki Kurake, Mr. Atsushi Ando, Mr. Harry Zhang, Mr. Takashi Kako, Mr. Kuangda Sun, Mr. Timothy Ryan Brubaker, Mr. Shun Imai, Mr. Hirotugu Sugiura, Mr. Masakazu Tomatsu, Mr. Yusuke Fukunaga, Mr. Borude Ranjit Rohidas, Mr. Jiadong Cao, Mr. Haoran Wang, Mr. Masayuki Nakamura, Mr. Keita Miwa, Mr. Xu Da, Ms. Sijie Liang, Mr. Takumi Ito, Mr. Kazuki Iwamoto, Mr. Takumi Kumakura, Mr. Kazuaki Kojima, Mr. Jialin Pan, Mr. Atsuki Asano, Mr. Shunichi Sato, Mr. Shinnosuke Takai, Mr. Suiki Tanaka, Mr. Takuya Tonami, Mr. Kenichi Naitoh, Mr. Takayuki Ryo Furuta, Mr. Naoki Yoshitake, Mr. Masato Imamura, Mr. Toshinari Ueyama, Mr. Daiki Kanno, Mr. Ren Kuramashi, Mr. Yukihiro Kurokawa, Mr. Mika Takahashi, Mr. Tomonori Ichikawa, Ms. Moe Okabe, Mr. Xitong Xie, Ms. Yan Hao, Ms. Kaede Katsuno, Mr. Naoki Takeda, Mr. Yugo Hosoi, Mr. Kaito Murakami, Mr. Soutarou Yamaoka, Mr. Yasuyuki Ohashi, Mr. Takahiro Omichi, Mr. Takumi Kato, Mr. Kazuya Nakane, Mr. Masaki Hasegawa, Mr. Ryo Hamaji, Mr. Shogo Maeda, and all other students who have studied in Professor Hori and Professor Ishikawa Laboratory for giving the big pleasure in life and creating a most enjoyable work atmosphere.

The author appreciates Ms. Yoko Kuwabara, Ms. Kazuyo Hirota, and Ms. Kazuyo Hirota for lots of encouragements and helpful advices in day-to-day life.

Finally, the author would like to appreciate his family including Mr. Naoki Amano, Ms. Hiroe Amano, Ms. Kana Amano, his grandparents, uncles, aunts, and cousins, for their help, support, and encouragement.

Tomoki Amano

February 2018

List of papers

1. Original Papers

Title	Journal	Authors Related Chapter
1. Nanographene synthesized in triple-phase plasmas as a highly durable support of catalysts for polymer electrolyte fuel cells	Japanese Journal of Applied Physics (accepted)	T. Amano, H. Kondo, K. Takeda, K. Ishikawa, M. Hiramatsu, M. Sekine, and M. Hori
2. Rapid growth of micron-sized graphene flakes by in-liquid plasma employing iron phthalocyanine-added ethanol	Applied Physics Express, 11 , (2018) 015102.	T. Amano, H. Kondo, K. Ishikawa, T. Tsutsumi, K. Takeda, M. Hiramatsu, M. Sekine, and M. Hori
3. Oxygen reduction reaction properties of nitrogen-incorporated nanographenes synthesized using in-liquid-plasma of ethanol and iron phthalocyanine mixture	Japanese Journal of Applied Physics (accepted)	T. Amano, H. Kondo, K. Takeda, K. Ishikawa, M. Hiramatsu, M. Sekine, and M. Hori

2. International Conferences

Title	Conference	Authors
1. Electro catalytic properties of Pt-supported nanographene synthesis using in-liquid plasma	6th International Symposium on Advanced Plasma Science and Its Applications for Nitride and Nanomaterials / 7th International Conference on Plasma-Nano Technology & Science, 05aB06O Meijo University, Aichi, Japan, March 2-6, 2014	T. Amano, K. Takeda, H. Kondo, K. Ishikawa, T. Ohta, M. Ito, H. Kano, M. Hiramatsu, M. Sekine, and M. Hori
2. Synthesis and electrocatalytic properties of Pt nanoparticles-supported nanographene synthesized employing in-liquid plasma	International Conference on Microelectronics and Plasma Technology 2014 (ICMAP 2014),MP-ECS-TuA-5, Gunsan, Korea, July 8-11, 2014	H. Kondo, T. Amano, K. Ishikawa, M. Sekine, M. Hori, M. Ito, and M. Hiramatsu
3. Controlled synthesis and electrocatalytic characteristics of Pt nanoparticles-supported nanographene synthesized by in-liquid plasma	67th Annual Gaseous Electronics Conference, FT3.00003, Raleigh, North Carolina, USA, November 2-7, 2014	H. Kondo, T. Amano, K. Ishikawa, M. Sekine, M. Hori, and M. Hiramatsu

List of papers

<p>4. Stability of the fuel cell electrode using the nanographene synthesized by in-liquid plasma</p>	<p>7th International Symposium on Advanced Plasma Science and Its Applications for Nitride and Nanomaterials / 8th International Conference on Plasma-Nano Technology & Science A5-O-03, Nagoya University, Aichi, Japan, March 26-31, 2015</p>	<p>T. Amano, K. Takeda, H. Kondo, K. Ishikawa, T. Ohta, M. Ito, H. Kano, M. Hiramatsu, M. Sekine, and M. Hori</p>
<p>5. Electrocatalytic Property and Durability of Pt Nanoparticles-Supported Nanographene Synthesized by In-Liquid Plasma</p>	<p>2015 MRS Spring Meeting & Exhibit, QQ7.03, San Francisco, California, USA, April 6-10, 2015</p>	<p>M. Hori, H. Kondo, T. Amano, K. Ishikawa, M. Sekine, M. Ito, and M. Hiramatsu</p>
<p>6. Stable structure analysis of the fuel cell electrode using the nanographene synthesized by in-liquid plasma</p>	<p>The 10th Anniversary Asian-European International Conference on Plasma Surface Engineering, 22a-D-4, Ramada Plaza Jeju Hotel, Jeju, Korea, September 20-24, 2015</p>	<p>T. Amano, K. Takeda, H. Kondo, K. Ishikawa, T. Ohta, M. Ito, H. Kano, M. Hiramatsu, M. Sekine, and M. Hori</p>
<p>7. Oxygen reduction reaction of fuel cell catalytic electrodes using nanographene materials synthesized by in-liquid plasma</p>	<p>8th International Symposium on Advanced Plasma Science and Its Applications for Nitride and Nanomaterials / 9th International Conference on Plasma-Nano Technology & Science 07pB110, Nagoya University, Aichi, Japan March 6-10, 2016</p>	<p>T. Amano, K. Takeda, H. Kondo, K. Ishikawa, T. Ohta, M. Ito, H. Kano, M. Hiramatsu, M. Sekine, and M. Hori</p>

List of papers

<p>8. Oxygen reduction reaction on highly-durable Pt/nanographene fuel cell catalyst synthesized employing in-liquid plasma</p>	<p>69th Annual Gaseous Electronics Conference, RR3.00006, Ruhr-Universität Bochum, Bochum, Germany, October 10-14, 2016</p>	<p>T. Amano, H. Kondo, K. Takeda, K. Ishikawa, H. Kano, M. Hiramatsu, M. Sekine, and M. Hori</p>
---	---	--